THE UNIVERSITY OF HULL

Pulsed Laser Annealing of CdTe/$Cd_{1-x}Mn_xTe$ Epilayers and Pulsed Laser Emission of ZnS/$Zn_{1-x}Cd_xS$ Quantum Well Structures

being a Thesis submitted for the Degree of

Doctor of Philosophy

in the University of Hull

by

Haidar Howari B.Sc, Tishreen University (Syria)

October 1999

Acknowledgements

I would like firstly to express my sincere gratitude to my supervisors Dr. J. E. Nicholls and Dr. J. H. C. Hogg for their support and encouragement throughout this work. I would like to extend my thanks to Dr. D. Sands for the expert guidance particularly in chapters 3 and 4. Many thanks are also due to Dr. T. Stirner and Prof. W. E. Hagston for allowing me to use their theoretical modelling by which the energy of excitons in quantum wells were calculated, and Dr. M. O'Neill for her guidance regarding chapter 5. I am grateful to Dr. D. E. Ashenford and B. Lunn for supplying valuable samples. I must thank also Prof. P. E. Dyer for the use of departmental facilities in the Physics department at Hull University. I must thank also Prof. A. G. Cullis and Mr. M. Fay for TEM measurements at the University of Sheffield. I would like to thank also Gordon Sowersby for keeping the laboratory equipment in good running order, Bill Buchan for his assistance with the cryogenic liquids in this work. Many thanks to Dr. L. May and Dr. P. Chen for the help and assistance during this work. My thanks to Ronnie, Peter, Saher, Faiz and Chris for their help and encouragement. Finally, I thank Al-Baath University (Syria) for the award of a Research Scholarship to study at the University of Hull.

To My Parents

Contents

Chapter 1

$CdTe/Cd_{1-x}Mn_xTe$ and $ZnS/Zn_{1-x}Cd_xS$ Heterostructures

In this chapter most of the basic physical properties of II-VI compound semiconductors are introduced. The crystal structure, band structure, quantum well and superlattice structures will be briefly reviewed. Strain effects in II-VI structures are discussed also in order to have a better idea about the processes taking place inside the crystal structure of the semiconductor. The shooting technique, for calculation of single particle energies, and calculation of the exciton binding energies are reviewed for superlattices and multiquantum wells.

1.1 The Interest in $CdTe/Cd_{1-x}Mn_xTe$ and $ZnS/Zn_{1-x}Cd_xS$ Heterostructures

II-VI semiconductor quantum well and superlattice structures have recently attracted increasing interest due to the considerable progress in the epitaxy growth techniques. As compared to the relatively smaller band-gap III-V quantum well structures (QWs), the wider band-gap II-VI compound multilayer structures are more suitable for various optoelectronic devices covering the near-infrared to visible and ultraviolet spectral range. Furthermore, II-VI compounds exhibit significantly larger exciton binding energies, for example, the exciton binding energy is 10 meV in CdTe compared to with 4.2 meV in GaAs. The larger exciton binding energy in II-VI materials, together with the significant enhancement of exciton binding energy in quasi-two-dimensional structures, make it possible for the exciton binding energy in QWS to exceed the LO phonon energy, resulting in efficient room-temperature QW device operation. Diluted magnetic semiconductors (DMS) are basically semiconducting alloys in which a fraction of group II atoms are replaced by magnetic atoms. CdMnTe, itself a diluted magnetic semiconductor, has optical and magneto optical properties due to the large Zeeman splitting of the exciton and the giant Faraday rotation which made CdMnTe an excellent candidate for opto-electronic applications like Optical Modulators, Polarizers and Magnetic Field Sensors [1]. Multiple Quantum Well (MQW) and Superlattice (SL) structures based on CdMnTe have enhanced magneto optical properties compared to those of bulk CdMnTe materials. A considerable amount

of work has been carried out on II-Mn-VI materials since its discovery and a huge number of papers have been published. The presence of Mn ions in these alloys has opened a new area of study into the quantum well context such as the magnetic properties, the sp-d exchange interaction, and the optical emissions specific to the Mn ions. Owing to the possibility of tuning the lattice parameters and their energy gaps, which can be performed by altering the composition of the materials, II-Mn-VI alloys are highly suitable candidates for the preparation of quantum wells, superlattices, and other heterostructures that involve band-gap engineering. As well, II-Mn-VI alloys are very important in the field of optical panel display applications due to the high electroluminescence efficiency of these materials. Furthermore, the existence of Mn ions in these materials leads to an exchange interaction between the sp band electrons and the d electrons of the Mn ions, which results in very large Zeeman splittings of the electronic levels. However new effects such as the giant Faraday rotation, the magnetic-field-induced metal-insulator transition, and the formation of the magnetic polarons have also been reported in these type of alloys. Finally we should realize that DMS alloys have the advantage of combining two important fields, semiconductivity and magnetism.

On the other hand, ZnS has always been a promising material for blue and UV light emitting diodes and laser diodes. When ZnS combines with other materials such as CdS, it produces a stimulating and potentially effective heterostructures such as ZnS/ZnCdS systems. The effective bandgap energy of a ZnS/ZnCdS quantum well structure can therefore be tuned within the green, blue, and ultraviolet spectral region by varying either Cd composition x or the well width L_z. In order to produce blue and UV light emitting devices from ZnS/ZnCdS structures it is advantageous to use as low a Cd concentration as possible to achieve the shortest possible lasing wavelength from the structure.

1.2 Crystal Structure of II-VI Compounds

II-VI compounds are known to crystallize into two basic structure forms; Cubic zinc-blende and hexagonal wurtzite. However, only zincblende structure will be reviewed here since all the samples used in the present thesis have the zincblende structure. Figure 1.1 shows the atomic arrangement for the zincblende structure. The cubic zincblende structure can be thought as two interpenetrating face centred cubic

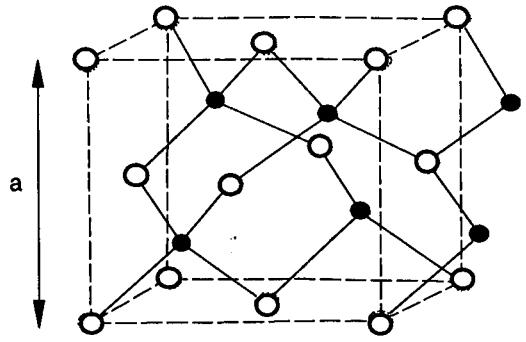

Figure 1.1: Schematic diagram of the zincblende crystal structure.

(fcc) sublattices (metal and non-metal), one being composed of group II atoms and the other of group VI atoms. One of the two sublattices is displaced along the body diagonal of the conventional unit cell by one quarter of length of the body diagonal [2,3]. Each group II(VI) atom is tetrahedrally bonded to four nearest neighbour group VI(II) atoms, each at a distance of $(1/4)\sqrt{3}a$, where a is the lattice constant. This type of bonding involves the two valence s electrons of the group II atom and the six valence p electrons of the group VI atom, this is referred as the $s\text{-}p^3$ bonding. Furthermore, each atom has twelve next nearest neighbour atoms of the same kind, located at a distance $(1/2)\sqrt{2}a$. Moreover, the zincblende structure does not have a centre of inversion symmetry which means that the [111] axis of the structure is a polar axis. Some examples of the zincblende II-VI compounds along with their room temperature lattice parameters are illustrated in table 1.1.

II-VI compound	Lattice parameter (Å)
CdTe	6.481
CdSe	6.052
CdS	5.832
ZnTe	6.104
ZnSe	5.669
ZnS	5.049

Table 1.1: Some zincblende II-VI compounds along with their lattice parameters at room temperature. Values are taken from ref [4].

CdMnTe materials have the same zincblende structure as CdTe for Mn concentration up to about 0.77%. Mn is a transition metal which contains two valence electrons in the *4s* orbital. Its *3d* shell is only half-filled (five spins are parallel). This makes it possible (because of the Hund's rule) to contribute its $4s^2$ electrons to the $s\text{-}p^3$ bonding, as a result of which Mn can replace the group II elements in the tetrahedral sites of the II-VI compounds. Table 1.2 shows the crystal structure and the corresponding ranges of composition for some II-Mn-VI diluted magnetic semiconductor alloys [5].

The lattice constant for II-Mn-VI materials are found to obey the Vegard's law. Vegard's law states that the average lattice parameter of a substitutional solid solution varies linearly with composition as given below [6]:

$$a = (1-x)a_A + xa_B \tag{1.1}$$

where a_A and a_B are the lattice parameters of the II-VI and Mn-VI materials.

For $Cd_{1-x}Mn_xTe$ materials which can be considered as a true alloy of CdTe and MnTe, its lattice constant is found to decrease linearly with x as expressed below [7]:

$$a(Cd_{1-x}Mn_xTe) = 6.481 \times (1 - 0.0225x)\ \text{Å} \tag{1.2}$$

ZnS and CdS exist in both crystal forms, i.e. cubic zincblende and hexagonal wurtzite crystal structures. The lattice parameters of the ZnS and CdS are shown in table 1.1. ZnCdS materials exists since Cd behaves similarly to Zn, i.e. the *3d* shell of

the Cd is completely filled and the valence *5s* orbital contains two electrons, therefore it can replace the Zn element in the tetrahedral sites of the ZnS material. The lattice parameter of a ZnCdS alloy with intermediate composition can be calculated using Vegard's law [6]:

$$a_{ZnCdS} = (1-x)a_{ZnS} + xa_{CdS} \tag{1.3}$$

where a_{ZnS} and a_{CdS} are the lattice parameters of ZnS and CdS respectively, x is the Cd composition, and a_{ZnCdS} is the lattice parameter of the ZnCdS alloy.

Materials	Crystal Structure	Range of composition
$Zn_{1-x}Mn_xS$	zincblende	$0 < x \leq 0.10$
	wurtzite	$0.10 < x \leq 0.45$
$Zn_{1-x}Mn_xSe$	zincblende	$0 < x \leq 0.30$
	wurtzite	$0.30 < x \leq 0.57$
$Zn_{1-x}Mn_xTe$	zincblende	$0 < x \leq 0.86$
$Cd_{1-x}Mn_xS$	wurtzite	$0 < x \leq 0.45$
$Cd_{1-x}Mn_xSe$	wurtzite	$0 < x \leq 0.50$
$Cd_{1-x}Mn_xTe$	zincblende	$0 < x \leq 0.77$
$Hg_{1-x}Mn_xS$	zincblende	$0 < x \leq 0.37$
$Hg_{1-x}Mn_xSe$	zincblende	$0 < x \leq 0.38$
$Hg_{1-x}Mn_xTe$	zincblende	$0 < x \leq 0.75$

Table 1.2: The crystal structure and the corresponding ranges of composition for some II-Mn-VI diluted magnetic semiconductor alloys [5].

1.3 Band Structure of II-VI Compounds

1.3.1 General Band Structure Features

Zincblende compounds such as CdTe and ZnS are direct bandgap semiconductors with the principal band edges occurring at the Γ point (*k=0*). Figure 1.2 illustrates a schematic diagram of the band structure of the cubic zincblende. At the zone centre the doubly degenerated conduction band $(\Gamma_1)\Gamma_6$ is generally thought to be associated with the *s*-like wavefunctions derived from the cation *s*-orbitals, whilst the six-fold degenerate valence band (Γ_{15}) is considered to be composed of *p*-like wavefunctions associated with the anion *p*-orbitals.

Due to the spin-orbit interaction, the six-fold degeneracy of the valence band (Γ_{15}) is lifted into a four-fold degenerate state Γ_8 (J=3/2; m_j=±3/2, ±1/2) and a lower two-fold degenerate state Γ_7 (J=1/2; ±1/2). These states are separated by the energy Δ. For CdTe Δ=0.80 eV [8] and for ZnS Δ=0.27 eV [9] at 293 K. The holes associated with the Γ_8 state are known as heavy holes (hh; with m_j=±3/2) and light holes (lh; with m_j=±1/2) according to their effective masses m^*_{hh} and m^*_{lh} respectively.

The dispersion of the bands close to the zone centre can be described by:

$$E(k) = \frac{\hbar^2 k^2}{2m^*}; \quad k^2 = k_x^2 + k_y^2 + k_z^2 \tag{1.4}$$

where m^* is the effective mass, taking account of the periodic crystal potential.

For CdTe, $m_e^* = 0.096m_0$ [10], $m_{hh}^* = 0.60m_0$ and $m_{lh}^* = 0.13m_0$ determined by Dang et al [11]. These values were used in the theoretical modelling of the quantum states of the MQWs.

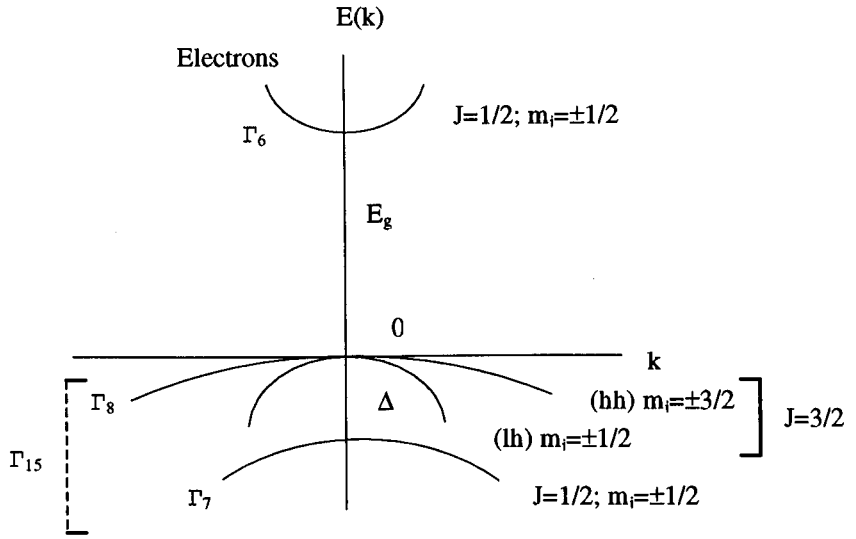

Figure 1.2: Schematic diagram of the zone centre band structure of zincblende.

1.3.2 The Energy Bandgap and its Dependence on Composition

The bandgap energies at 4.2 K and 300 K and the lattice parameters at 300 K for CdTe, MnTe, CdS and ZnS zincblende are illustrated in table 1.3.

Adding increasing amounts of Mn to CdTe widens the bandgap as the alloy lattice parameter decreases. The bandgap energy E_g for $Cd_{1-x}Mn_xTe$ varies linearly with Mn concentration x and it is given by Furdyna [5]:

$$E_g(4.2K) = 1.606 + 1.592x \quad (eV), \tag{1.5}$$

for the composition range $x < 0.77$.

	CdTe	MnTe	CdS	ZnS
Lattice parameter (Å)	6.481	6.334	5.818	5.4093
Bandgap energy (eV)	1.606 (4.2 K) 1.528 (300 K)	3.2 (2.4 K) 2.9 (300 K)	2.56 (4.2 K) 2.36 (300 K)	3.84 (4.2 K) 3.67 (300 K)

Table 1.3: Lattice parameters at 300 K and bandgap energies at 4.2 K and 300 K of CdTe, MnTe, CdS and ZnS cubic zincblende taken from references [4],[5] and [12].

The bandgap of CdS is 2.56 eV at 4.2 K, compared with 3.84 eV for ZnS [12]. In the case of ZnCdS the substitution of Cd at the Zn sites causes the bandgap to decrease as the alloy lattice parameter increases. The variation of E_g with x for $Zn_{1-x}Cd_xS$ is given by [13]:

$$E_g(Zn_{1-x}Cd_xS) = 3.84 - 2.0781x + 0.82662x^2 \quad (eV) \tag{1.6}$$

In the range of $0 \leq x \leq 0.2$ E_g can be given by [7]:

$$E_g(Zn_{1-x}Cd_xS) = 3.839 - 2.139x \quad (eV) \tag{1.7}$$

The effective masses for the electron, heavy hole and light hole in CdTe and ZnS are given in table 1.4.

	Effective masses in CdTe	Effective masses in ZnS
m_e^*	$0.096m_0$	$0.34m_0$
m_{hh}^*	$0.60m_0$	$1.76m_0$
m_{lh}^*	$0.13m_0$	$0.26m_0$

Table 1.4: The electron and hole effective masses in CdTe and ZnS taken from references [10], [11] and [14].

1.4 Low Dimensional Structures, Quantum Well and Superlattices

The fabrication of semiconductor heterostructures with layer thicknesses and chemical composition that can be controlled extremely precisely was an outcome of the recent developments of crystal growth techniques such as molecular beam epitaxy (MBE) and metal-organic chemical vapour deposition (MOCVD). Layers with thicknesses that can be controlled almost at the atomic scale became a possibility to grow by MBE. The optical properties of semiconductors can be altered by varying the layer thickness and composition of the material in order to meet the specific requirements of the device of interest. This kind of structure design is known as bandgap engineering.

When a thin semiconductor layer is deposited, sandwiched between two layers of another semiconductor with larger bandgap, a potential well is formed. In this way the freedom of the carrier motion is restrained to a lower dimension and the carrier energy is quantized. This defines a quantum well.

When two thin semiconductor layers of different bandgap are deposited in sequence on a substrate as shown in figure 1.3, periodic potential steps in the growth (z) direction are formed. If the thickness of the semiconductor layers is less than the de Broglie wavelength of the charge carrier involved, given by:

$$\lambda = \frac{h}{\sqrt{2m^*E}}, \tag{1.8}$$

then the electron band structure will be altered by the quantum confinement or quantum size effects and the description of the carrier motion in the z direction follows a quantum mechanical regime. This is known as a superlattice, figure 1.3.

1.4.1 Band Alignment

According to the size and arrangement of the band offsets of the two semiconductors, the band alignment at the heterointerfaces of a quantum well or superlattice structure are classified into three different types. In a type I band line-up, both types of carriers (electrons and holes) are confined in the same layer i.e. electrons in the conduction band and holes in the valence band as shown in figure 1.4. Optical

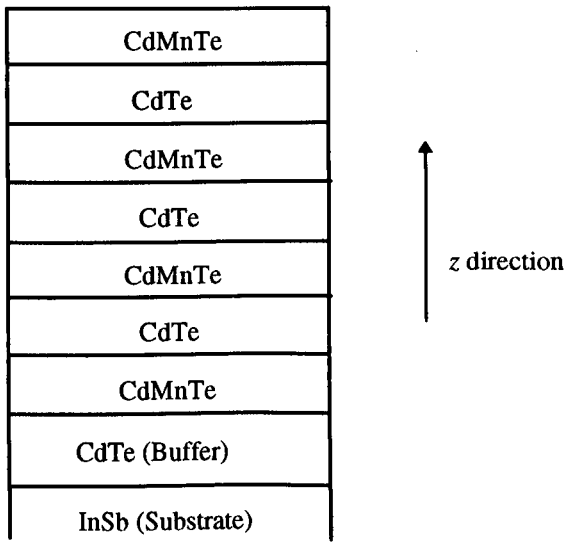

Figure 1.3: Schematic diagram of CdTe/CdMnTe superlattice structure.

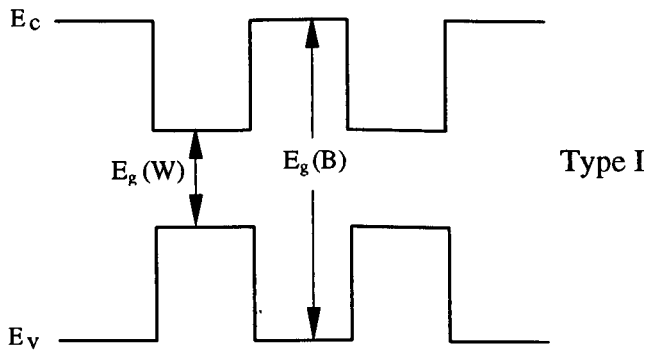

Figure 1.4: Schematic illustration of the band line-up in type I structure.

transitions thus occur directly without the need of emitting phonons in the process. Therefore, bright and efficient luminescence is produced in this type of structure. For the type II band alignment,electrons and holes are localised in different layers, figure 1.5. Consequently, optical transitions are indirect in space and phonons must be emitted in the process. Moreover, optical emissions from type II systems are in general weak and inefficient owing to the particle wavefunctions not overlapping. In type III systems, which are known also as misaligned type II systems, the material posses semi-metallic properties. Also the energy of the conduction band minimum in the well lies below the valence band maximum energy in the barrier as shown in figure 1.6.

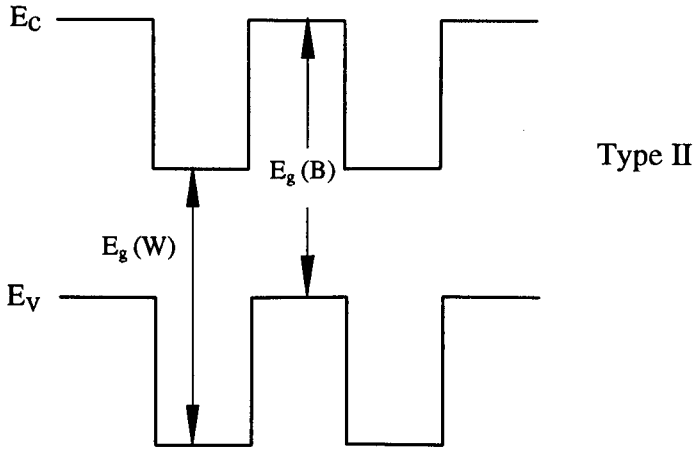

Figure 1.5: Schematic illustration of the band line-up in type II structure.

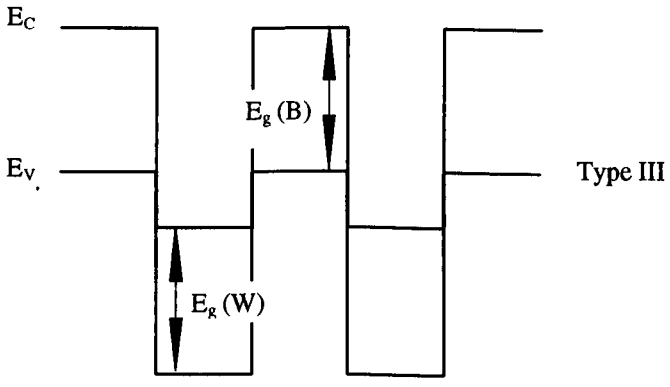

Figure 1.6: Schematic illustration of the band line-up in type III structure.

1.4.2 Single Quantum Well

A single quantum well is the simplest form of a quantum well structure. In principle, it is formed when a thin layer of a semiconductor material of low bandgap is sandwiched between two thicker layers of another semiconductor material of greater

bandgap. The conduction and valence bands are usually aligned in a type I structure as shown in figure 1.7.

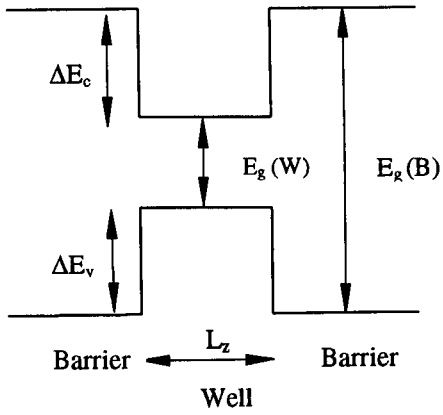

Figure 1.7: The band line-up of a single quantum well structure.

The confinement of the carrier motion in the growth direction *(z)* lifts the electron in the conduction band (and the hole in the valence band) into a number of confined state energy levels. Along the growth direction *(z)*, the carrier motion can be represented by the Schrodinger equation:

$$\left(-\frac{\hbar^2}{2m^*(z)}\frac{\partial^2}{\partial z^2}+V(z)\right)\Psi_n(z)=E_n\Psi_n(z) \tag{1.9}$$

where $\Psi_n(z)$ is the electron envelope wavefunction, $m^*(z)$ is the effective mass of carriers which is written as a function of z because the well and the barrier material may posses different effective masses, $V(z)$ describes the energy level of the bottom of conduction bands and E_n is known as the confinement energy of the carriers. The periodical lattice potential is incorporated in the effective mass term $m^*(z)$. The general solution to the time-independent Schrodinger equation (1.9) inside such a quantum well, defined by $-L_z/2 < z < L_z/2$, is a superposition of standing waves given by [15]:

$$\Psi(z)=A\sin k_1 z+B\cos k_1 z \tag{1.10}$$

where k_1 is the magnitude of the momentum vector in the well which is related to the electron energy by:

$$(k_1)^2=\frac{2m_eE}{\hbar^2} \tag{1.11}$$

where m_e is the effective mass of the electron (or m_h for holes) and E is the energy of electrons (or holes), referenced to the conduction band edge (or valence band edge for

holes). As the wavefunctions outside the well must vanish at $\pm\infty$, the solutions to the wavefunction in this region are:

$$\Psi(z) = C\exp(k_2 z) \; for \; z < -L_z / 2 \tag{1.12}$$

$$\Psi(z) = D\exp(-k_2 z) \; for \; z > L_z / 2 \tag{1.13}$$

where

$$(k_2)^2 = \frac{2m_e(\Delta E_c - E)}{\hbar^2} \tag{1.14}$$

and ΔE_c is the conduction band offset between the well and the barrier materials which in turn represent the height of the potential barrier in the conduction band.

The boundary conditions are that the eigenfunctions and their derivatives must be continuous at $\pm L_z/2$. By employing these conditions the following solutions are found:

$$k_1 \tan\frac{k_1 L_z}{2} = k_2 \quad (even \; solutions) \tag{1.15}$$

$$k_1 \cot\frac{k_1 L_z}{2} = -k_2 \quad (odd \; solutions) \tag{1.16}$$

These two equations, 1.15 and 1.16, give the confined electron (hole) energy levels within the quantum well with $n=1$ being the lowest energy level.

When a free electron in the conduction band and a free hole in the valence band experience a coulomb attraction as a result of their opposite charge an excition is formed.

The energy of emission from a single quantum well can be written as:

$$h\nu = E_g + E_{ne} + E_{nh} - E_{ex} \tag{1.17}$$

where E_g is the bandgap of the well material, E_{ne} is the electron energy level, E_{nh} is the hole energy level and E_{ex} is the exciton binding energy. This clearly indicates that the bandgap of the well material increases by the quantum confinement. Emission is usually governed by the lowest energy i.e. $n_1 \rightarrow h_1$ transition.

Another important feature of quantum wells is their density of states which is quite different from that of the bulk semiconductors. In bulk semiconductors, the three dimensional density of states as a function of energy can be represented as:

$$\rho(E)dE = \frac{1}{2\pi^2}\left(\frac{2m_e}{\hbar^2}\right)^{3/2} E^{1/2} dE \tag{1.18}$$

The density of states function is actually parabolic, where $\rho(E) \rightarrow 0$ as $E \rightarrow 0$. In a two dimensional system with quantum confinement in the z-direction, the two dimensional density of states as a function of energy is given by:

$$\rho(E)dE = \frac{1}{2\pi}\left(\frac{2m_e}{\hbar^2}\right)\frac{1}{L_z}\sum_{n=1}^{\infty} H(E - E_n)dE \qquad (1.19)$$

where the term $H(E-E_n)$ is the Heaviside function for the quantum state energy E_n. This results in a step-like function of energy, figure 1.8. In thick quantum wells the steps

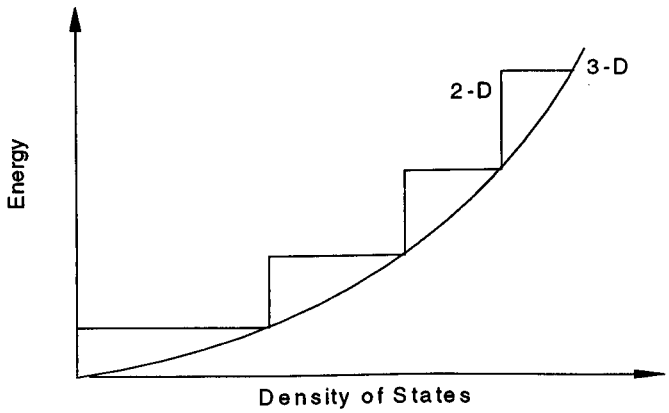

Figure 1.8: The density of states function for electrons in a thin quantum well (2-D) compared to that of a bulk semiconductore (3-D).

are small, but as L_z decreases, the energy steps become larger which means that in thinner quantum wells fewer states are confined. Thus in a 2D system the density of states of the lowest energy *(n=1)* is finite and direct recombination is enhanced. This makes quantum well structures highly efficient emitters and well qualified to the field of lasers and display devices.

1.4.3 Multiple Quantum Wells and Superlattices

When a series of quantum wells are deposited in a periodic arrangement then a multiple quantum well (MQW) structure is formed as shown in figure 1.9. The electronic structure of each well is similar to that of a single quantum well. In a MQW structure, the barrier layers are thick enough that the wavefunctions of adjacent confined states do not interact in any way. Thus the electronic structure of each well can be treated separately as a single quantum well. If however the barriers are sufficiently thin, the wavefunctions at adjacent confined states overlap and interact causing the confined energy levels to split into a number of levels given by the number of coupled wells. Such a structure is known as a superlattice (SL), see figure 1.10. In the limit of sufficiently large number of coupled wells, the energies form a quasi-continuous band known as miniband, as shown in figure 1.10. The width of the

minibands in a SL structure is determined by the band offsets, the effective masses and the well and barrier widths.

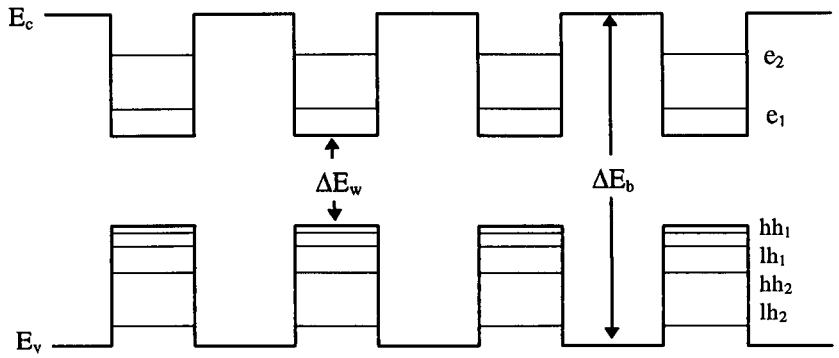

Figure 1.9: A schematic diagram shows the band structure and energy levels in a type I MQW structure.

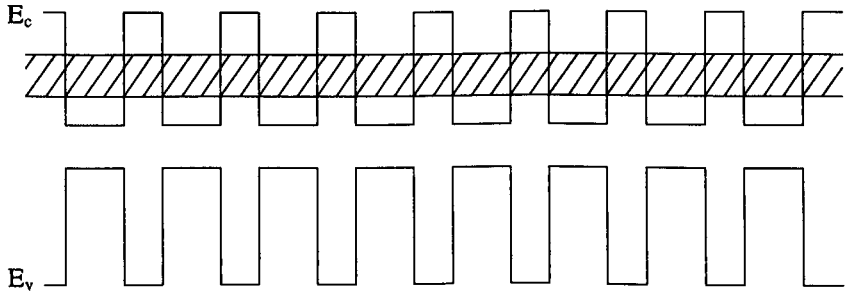

Figure 1.10: A schematic diagram showing the energy levels (minibands) in a superlattice.

1.5 Strain Effects in II-VI Structures

When an epitaxial layer is grown on a substrate it will initially adopt the lattice parameter of the substrate material. Due to the poor availability and high cost of appropriate II-VI substrate materials, III-V substrates are almost always used. This causes a mismatch of the lattice parameters between the epilayer and the substrate material. The in-plane (bi-axial) mismatch can be accommodated by introducing coherent strain in the epilayer provided that the epilayer thickness remain below a critical thickness (h_c). However, when the epilayer thickness exceeds h_c misfit dislocations become energetically favourable and develop at the substrate-epilayer interface allowing the epilayer to relax. Should the critical thickness be exceeded and misfit dislocations form, the optical quality of the structure may be impaired. Such a structure would generally be unsuitable for use in a semiconductor laser. On the other hand, the strain may significantly alter the properties of the structure affecting the band line-ups and the optical properties.

When a strained cubic epilayer is deposited pseudomorphically onto a lattice mismatched substrate, the layer undergoes some kind of a tetragonal distortion as a result of the Poisson ratio. The in-plane (x,y) bi-axial strain (ε) for an epilayer below the critical thickness is equal to the lattice mismatch (ξ) which can be represented by:

$$\varepsilon = \varepsilon_{xx} = \varepsilon_{yy} = \frac{a_\eta - a_0}{a_0} = \xi \tag{1.20}$$

where a_0 is the unstrained lattice parameter of the epilayer material and a_η is the strained in-plane lattice parameter (i.e. the lattice parameter of the substrate material). As the lattice parameters of the layer and substrate change differently with temperature, the mismatch strain is temperature dependent. The biaxial strain also causes a uniaxial strain parallel to the growth axis, which can be written as [16]:

$$\varepsilon_{zz} = -\frac{2C_{12}}{C_{11}}\varepsilon_{xx} = \frac{a_\perp - a_0}{a_0} \tag{1.21}$$

where $a_\perp$ is the perpendicular strained lattice constant and C_{12} and C_{11} are the elastic stiffness constants. As a matter of fact the strain cancels the lattice mismatch in the x, y directions of the layer plane but enhances it in the z direction. However, x-ray diffraction can be used to measure the perpendicular strained lattice parameter $a_\perp$ of the epilayer.

An empirical relation can be employed to evaluate the critical thickness of the epilayer [17] which is given by:

$$\varepsilon\, h_c = 0.8\, nm \tag{1.22}$$

It is quite clear that the greater the lattice mismatch , the smaller the critical thickness. Therefore it is desirable to employ a substrate with lattice parameter as close as possible to the corresponding lattice parameter of the epilayer which is to be deposited.

The biaxial in-plane strain (ε) of an epilayer can be analyzed as the sum of a hydrostatic and a uniaxial strain in the growth direction [18]. This results in a twofold effect on the zincblende band structure. The hydrostatic strain alters the bandgap of the material while the uniaxial (tetragonal) strain lifts the degeneracy at the centre of the fourfold degenerate valence band Γ_8, splitting the heavy hole and light hole states as shown in figure 1.11.

By employing the strain Hamiltonian of Pikas and Bir [19], it is possible to calculate the shifts of the valence band relative to the conduction band. The energy shifts of the valence band edges to the conduction band (ΔE_g^{hh} and ΔE_g^{lh}) are given by [20]:

$$\Delta E_g^{hh} = E_H + E_U \tag{1.23}$$

$$\Delta E_g^{lh} = E_H + \frac{1}{2}(\Delta - E_U) - \frac{1}{2}\sqrt{9E_U^2 + 2\Delta E_U + \Delta^2} \tag{1.24}$$

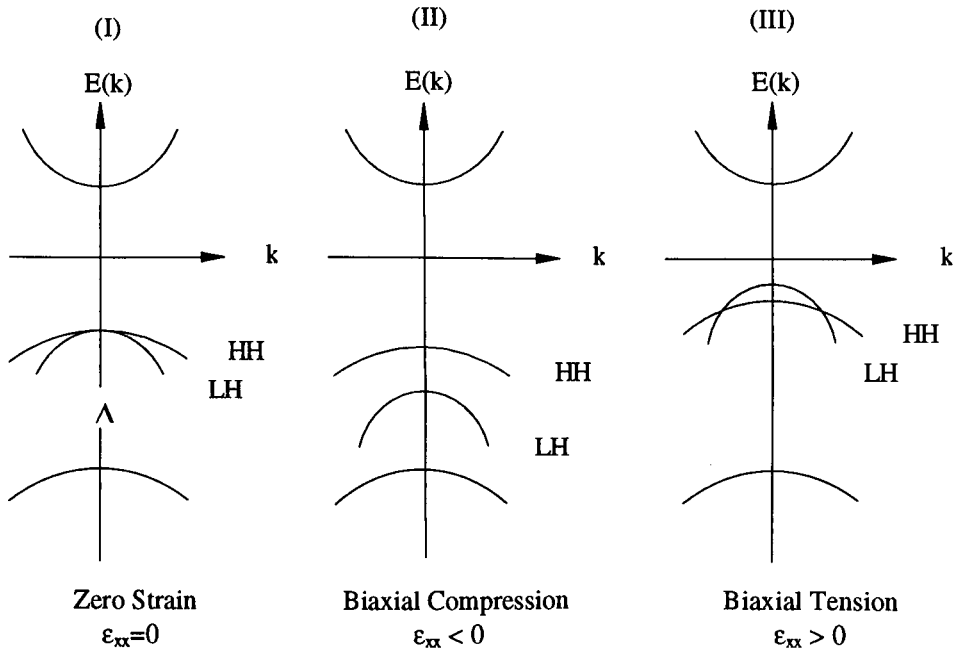

Figure 1.11: The zone centre band structure of a cubic zincblende crystal under: (I) Zero Strain ($\varepsilon_{xx}=0$), (II) Biaxial Compression $\varepsilon_{xx} < 0$ and (III) Biaxial Tension $\varepsilon_{xx} > 0$.

where E_H is the hydrostatic contribution given by:

$$E_H = 2a(\frac{C_{11} - C_{12}}{C_{11}})\varepsilon_{xx} \tag{1.25}$$

and E_U is the unaxial contribution given by:

$$E_U = -b(\frac{C_{11} + 2C_{12}}{C_{11}})\varepsilon_{xx} \tag{1.26}$$

and where Δ is the spin-orbit splitting energy, a is the hydrostatic deformation potential and b is the tetragonal deformation potential. When $\Delta >> E_U$ then the light hole shift can be approximated as:

$$\Delta E_g^{lh} = E_H - E_U \tag{1.27}$$

Camphausen et al [21] has shown that 2/3 of the hydrostatic component of E_H is in the conduction band

Table 1.5 illustrates the deformation potentials and the elastic constants for some II-VI compounds.

	CdTe	ZnS
Deformation Potentials (eV)		
a (hydrostatic)	-3.5	-4.0
b (unaxial)	-1.1	0.8
		0.5
Elastic Constants (GPa)		
C_{11}	53.6	106.7
C_{12}	37	66.6
Spin-Orbit Splitting Δ (eV)	0.8	0.07

Table 1.5: Values of deformation potentials, elastic constants and spin-orbit splitting for CdTe taken from references [22, 23, 8] and for ZnS taken from references [14,24].

1.6 The Shooting Technique

In the present thesis a numerical method was utilized to solve the differential equations such as the Schrodinger equation and the diffusion equations. This method is well-known as the shooting technique [25, 26].

For an electron or a hole in a one dimensional potential $V(z)$ the Hamiltonian is described as the following:

$$H = -\frac{\hbar^2}{2m^*}\frac{d^2}{dz^2} + V(z) \tag{1.28}$$

The Schrodinger equation which is given by

$$H\psi = E\psi \tag{1.29}$$

can be rewritten according to equation (1.28) as the following:

$$-\frac{\hbar^2}{2m^*}\frac{d^2\psi}{dz^2} + (V(z) - E)\psi = 0 \tag{1.30}$$

In order to calculate the single particle energy levels it is not sufficient to find a one-electron energy E which fulfils equation (1.30) for all values of z, but it is also essential to find the function ψ which satisfies the boundary conditions $\psi(z) \to 0$ as $z \to \pm\infty$.

If we consider a general function $f(z)$ as depicted in figure (1.12), then the derivative of $f(z)$ can be approximated by a finite difference

$$\frac{df}{dz} \approx \frac{f(z+\delta z) - f(z-\delta z)}{2\delta z} \tag{1.31}$$

with the approximation becoming exact in the limit as $\delta z \to 0$. Therefore the second derivative

$$\frac{d^2 f}{dz^2} \approx \frac{\left(\frac{\partial f}{\partial z}\right)_{z+\delta z} - \left(\frac{\partial f}{\partial z}\right)_{z-\delta z}}{2\delta z} \tag{1.32}$$

takes the form

$$\frac{d^2 f}{dz^2} \approx \frac{f(z+2\delta z)+f(z-2\delta z)-2f(z)}{(2\delta z)^2} \tag{1.33}$$

Since the small increment δz along the growth (z) direction is as yet arbitrary the transformation $2\delta z \to \delta z$ can be made, thus equation (1.33) can be rewritten as:

$$\frac{d^2 f}{dz^2} \approx \frac{f(z+\delta z)+f(z-\delta z)-2f(z)}{(\delta z)^2} \tag{1.34}$$

Employing this finite difference approximation for the second derivative of a function, the Schrodinger equation (1.30) can be transformed into

$$-\frac{\hbar^2}{2m^*}\frac{\psi(z+\delta z)+\psi(z-\delta z)-2\psi(\delta z)}{(\delta z)^2}+(V(z)-E)\psi(z)=0 \tag{1.35}$$

Therefore

$$\psi(z+\delta z)=[2(\delta z)^2\frac{m^*}{\hbar^2}(V(z)-E)+2]\psi(z)-\psi(z-\delta z) \tag{1.36}$$

Equation (1.36) indicates that if the wavefunction is known at the two points $z-\delta z$ and z, then the value of the wavefunction at $z+\delta z$ can be calculated, for any arbitrary chosen energy E. Using two known values of the wavefunction at $\psi(z-\delta z)$ and $\psi(z)$, a third $\psi(z+\delta z)$, can be evaluated. This process can be reiterated and the complete wavefunction can be found at any particular energy. The solution which ascribes the stationary state of concern has a wavefunction that conforms the standard boundary conditions, i.e. $\psi \to 0$ as $z \to \pm\infty$. This forms the basis of the shooting technique.

In the case of bound states in the structure the wavefunction will decline on both sides of the quantum well, as one moves away from it. At some distance of the well the wavefunction will brought down to effectively zero, these points define the 'effective infinities'. Since the wavefunction does not vary anymore beyond these points towards $\pm\infty$ the structure can be truncated there without altering the eigenvalue E.

If we consider the left end of the structure at $z=0$ and the right end at $z=L$ then

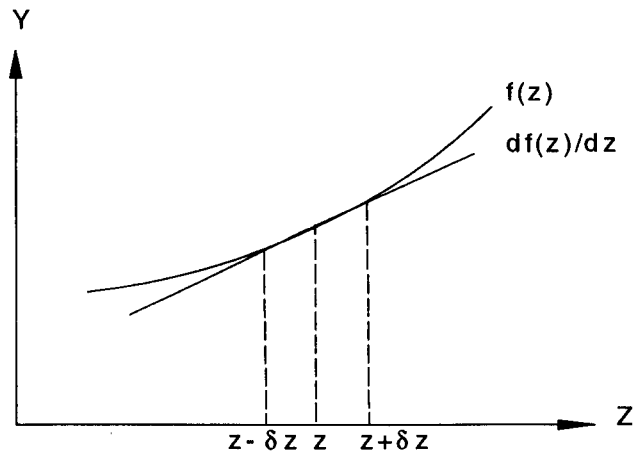

Figure 1.12: Finite difference approximation to a derivative of a function.

the boundary conditions can be rewritten as $\psi(0) = 0$ and $\psi(L) = 0$.

By employing the first of these boundary conditions i.e. $\psi(0) = 0$, one of the first two values of the wavefunction required to commence the iterative process can be obtained. The second value $\psi(\delta z)$ originates from the fact that the wavefunction increases with increasing z. Since the eigenvalue E is independent of the scaling of the wavefunction, thus the magnitude of $\psi(\delta z)$ is arbitrary. Hence

$$\psi(0) = 0 \quad \text{and} \quad \psi(\delta z) = 1, \tag{1.37}$$

Apparently the actual magnitude of δz relies on the required accuracy and the particular system under investigation. This forms the basis of the initial conditions necessary for implementation of the shooting technique to model semiconductor heterostructures that contain stationary states. Furthermore the method can be used to investigate systems with arbitrary potential profiles in which m^* and V are, in general, a function of position.

1.7 Exciton Binding Energy Calculation

In quantum well structures electron-hole pairs, known as excitons, are formed because of the coulombic interaction of the two particles. This results in lowering the total energy of the system. The Hamiltonian of the interaction two-body (electron and hole) system can be expressed as:

$$H = H_e + H_h + H_{eh} \tag{1.38}$$

where H_e and H_h are the one-particle electron and hole Hamiltonian appropriate to motion along the z-direction, whereas H_{eh} represents the electron-hole interaction term and the kinetic energy in the xy-plane of the relative motion, and is given by:

$$H_{eh} = \frac{p_{\perp}^2}{2\mu_{\perp}} - \frac{e^2}{4\pi\varepsilon r} \tag{1.39}$$

where $p_{\perp}$ and $\mu_{\perp}$ are the momentum and reduced mass of the exciton perpendicular to the growth (z) direction. The spatial separation r of the electron and hole is given by:

$$r^2 = (x_e - x_h)^2 + (y_e - y_h)^2 + (z_e - z_h)^2 \tag{1.40}$$

The kinetic energy of the centre-of-mass in the xy-plane has been disregarded since the maximum interest lies with optical absorption and emission for which this energy must equal to zero by momentum conservation.

In order to solve the associated Schrodinger equation, a variational method [27, 28] was utilized. This involves making a choice of a trial wavefunction Ψ within the envelope function approximation which is a product of three terms given by:

$$\Psi = \psi_e(z)\psi_h(z)\varphi(r') \tag{1.41}$$

The first two of these ψ_e and ψ_h represent the uncorrelated one-particle electron and hole wavefunction respectively, whilst the third term $\varphi(r')$ represents the electron-hole interaction which is given by:

$$\varphi(r') = \exp(-\frac{r'}{\lambda}) \tag{1.42}$$

where

$$r'^2 = (x_e - x_h)^2 + (y_e - y_h)^2 + (1-\beta^2)(z_e - z_h)^2 \tag{1.43}$$

with λ and β variational parameters.

The difference in Ψ, from that commonly found in the literature [29, 30], manifests itself in the choice of φ. The parameter β is included in the electron-hole interaction term in order to allow the exciton to assume planar (2D), spherical (3D) or any intermediate symmetry should it be energetically favourable to do so.

Substitution of Ψ into equation (1.38) leads to an equation of the total energy of the system:

$$E = E_e + E_h - E_b \tag{1.44}$$

where E_e and E_h are the electron and hole one particle energies, i.e.

$$E_e = \frac{\langle \psi_e | H_e | \psi_e \rangle}{\langle \psi_e | \psi_e \rangle} \tag{1.45}$$

for the electron, and

$$E_h = \frac{\langle \psi_h | H_h | \psi_h \rangle}{\langle \psi_h | \psi_h \rangle} \tag{1.46}$$

for the hole.
The exciton binding energy is given by:

$$E_b = -\frac{\hbar^2}{2\mu} \frac{\int |\psi_e|^2 |\psi_h|^2 \left|\frac{\partial \varphi}{\partial z_e}\right|^2 d\tau}{\int |\psi_e|^2 |\psi_h|^2 |\varphi|^2 d\tau} - \frac{\int |\psi_e|^2 |\psi_h|^2 (\varphi H_{eh} \varphi) d\tau}{\int |\psi_e|^2 |\psi_h|^2 |\varphi|^2 d\tau} \tag{1.47}$$

The formalism developed so far is independent of the specific form of the (uncorrelated) one-particle electron and hole wavefunctions ψ_e and ψ_h. In particular, it can therefore be utilized in any semiconductor heterostructure whose one-particle Schrodinger equations are solvable.

The variational calculation is implemented by adjusting the parameters λ and β until the exciton binding energy is maximized, thus minimizing the total energy of the system.

References

[1] X. Wang, C. Qiu, and D. Labrie; Thin Solid Films, 213, pp. 155-157 (1992).

[2] *"Introduction to Solid State Physics"*, Seventh Edition, Charles Kittel, (John Wiley & Sons, Inc). Chapter 1, pp. 1-26 (1996).

[3] *"Physics and Chemistry of II-VI Compounds"*, edited by M. Aven and J. S. Prener, North Holland Publishing Company, Chapter 1, pp. 3-72 (1967).

[4] *"Landolt-Bornstein, Semiconductors: Physics of II-VI and I-VII Compounds, Sememagnetic Semiconductors"*, Volume III/17b, edited by O. Madelung, Springer-Verlag (1982).

[5] J. K. Furdyna, J. Appl. Phys. 64, 4, R29 (1988).

[6] L. May, Ph.D. Thesis, University of Hull, UK (1999).

[7] R. L. Harper, Jr, R. N. Bicknell, D. K. Blanks, N. C. Giles, J. F. Schetzina, Y. R. Lee, and A. K. Ramdas, J. Appl. Phys. 62, 624 (1989).

[8] *"Semiconductors Other than Goup IV Elements and III-V Compounds"*, edited by O. Madelung, Spring-Verlag, Berlin (1992).

[9] H. E. Ruda, J. Appl. Phys. 59, pp. 3516 (1986).

[10] P. Lawaetz, Phys. Rev. B 4, 3460 (1971).

[11] L. S. Dang, G. Neu, and R. Pomestain, Solid State Commun. 44, 1187 (1982).

[12] T. Taguchi, C. Onodera, Y. Yamada, and Y. Masumoto, Jpn. J. Appl. Phys. 32, 9B, pp. L1308-L1311 (1993).

[13] T. Yokogawa, T. Ishikawa, J. L. Merz, and T. Taguchi, J. Appl. Phys. 75, 4, pp. 2189-2193 (1994).

[14] *"Landolt-Bornstein, Numerical Data and Functional Relationship in Science and Technology"*, New Series, Part III, Volume 22a, "Semiconductors:

Supplement to Volume III/17", edited by O. Madelung, and M. Schulz, Springer-Verlag (1987).

[15] "*Semiconductor Lasers: Past, Present and Future*", Goving P. Agrawal, Chapter 1, pp. 1-27, AIP Press (1995).

[16] K. Shahzad, D. J. Olego, and C. G. Van der Walle, Phys. Rev. B 38 (2), 1417 (1988).

[17] D. J. Dunstan, P. Kidd, L. K. Howard, and R. H. Dixon, Appl. Phys. Lett. 59, 3390 (1991).

[18] P. Voisin, Surf. Sci. 168, 546 (1986).

[19] G. E. Pikas and G. L. Bir, Sov. Phys. Sol. State, 1502 (1959).

[20] J. C. Hensel and G. Feher, Phys. Rev. 129, 1041 (1963).

[21] D. L. Camphausen, G. Connell, and W. Paul, Phys. Rev. Lett. 26, 184 (1971).

[22] D. G. Thomas, J. Appl. Phys. 32, 2298 (1961).

[23] D. J. Dunstan, B. Gil, and K. P. Homewood, Phys. Rev. B 38, 7862 (1988).

[24] C. G. Van der Walle, Phys. Rev. B39, 1817 (1989).

[25] "*Microcomputer Algorithms*", J. P. Killingbeck, (Adam Hilger, 1992).

[26] "*Fundamentals of Modern Physics*", R. M. Eisberg (John Wiley & Sons, New York, (1961).

[27] C. P. Hilton, W. E. Hagston and J. E. Nicholls, J. Phys. A 25, 2395 (1992).

[28] C. P. Hilton, J. Goodwin, P. Harrison and W. E. Hagston, J. Phys. A 25, 5365 (1992).

[29] J. W. Wu and A. V. Nurmikko, Phys. Rev. B 36, 4902 (1987).

[30] C. R. Proetto, Phys. Rev. B 41, 5081 (1993).

Chapter 2

Experimental Techniques

2.1 Introduction

This chapter describes in details the methods used for the present thesis work. The main experimental techniques to have been carried out are Photoluminescence (PL) Spectroscopy, Photoluminescence Excitation (PLE) Spectroscopy (at zero and various magnetic fields), Reflectivity, Stimulated Emission, and Double Crystal X-Ray Diffraction. Since all the samples used in the current thesis were grown using Molecular Beam Epitaxy (MBE), therefore it is very helpful to give a brief description also of the MBE Technique.

2.2 X-ray Diffraction Analysis

2.2.1 Introduction

X-ray diffraction has always been a very powerful method for studying Epitaxial Low Dimensional Structures (LDS) and a vast amount of work has been carried out by many authors using this technique to extract valuable information of their structures. To understand the optical and electronic properties of thin films semiconductors heterostructures, it is necessary to have an accurate knowledge of the structural parameters. X-ray diffraction offers a non-destructive, highly strain-sensitive method for analysing Low -Dimensional structures and it is a valuable and sensitive method for obtaining information such as the thickness of the layers, the total film thickness, the lattice parameter and the relaxation and composition of the layers [1],[2],[3],[4].

The samples which form the subject of this study have been grown using an advanced crystal growth technique called Molecular Beam Epitaxy (MBE) [5]. MBE structures are ideal systems for studying thin film semiconductor heterostructures because the deposition can be controlled on an atomic scale and nearly perfect crystals can be obtained. Another advantage is the small lattice mismatch between the layers leading to a minimal coherency strains in the structures.

2.2.2 X-ray Diffraction Techniques

2.2.2.1 Single Crystal X-ray Diffractometer

The basic arrangement consists of an x-ray source, slit, sample and a detector figure (2.1). The sample is rotated until a Bragg reflection occurs, the interatomic layer spacing can be calculated by relating the rotation angle through Bragg's law, equation 2.1. The disadvantage of this system is that the x-ray source contains a wide range of wavelengths and the arrangement is wavelength dispersive which limits the spacing resolution [6].

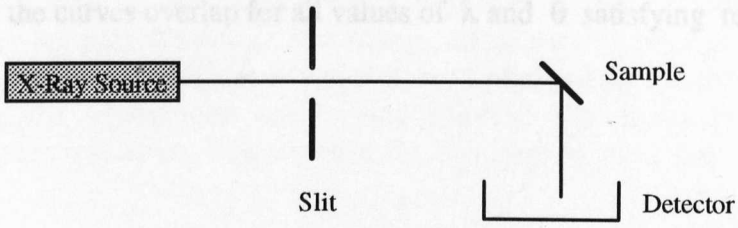

Figure 2.1: Single Crystal X-ray Diffraction Principle.

2.2.2.2 Double Crystal X-ray Diffractometer

The system was installed as shown in figure (2.2), it uses sealed x-ray source to produce the x-ray beam, then the x-ray beam is collimated to produce a low divergence beam which then reflects on the reference crystal which is cut with appropriate set of Bragg planes parallel to the surface, then the x-ray beam reflects symmetrically to the second crystal (the sample), after that the reflected beam can be detected by moving detector through it [1], [6],[7]. Here we apply Bragg's law :

$$2d\sin\theta = n\lambda \tag{2.1}$$

Where d is the layer spacing, θ is the Bragg angle, n is the order number and λ is the wavelength. In this method the sample and the reference crystal must have the same lattice parameter and the reflection planes of both crystals must set parallel to each

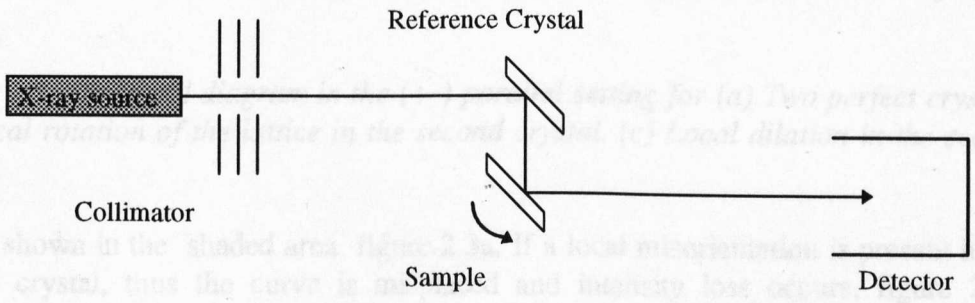

Figure 2.2: Double Crystal X-Ray Diffraction Principal.

other. This system is non-wavelength dispersive only when this condition is met. The diffracted intensity can be plotted against the rotation angle of the sample and then we obtain the rocking curve which is in fact a superposition of the rocking curve of both crystals the reference and the sample. If the (d) spacing of the sample is changed so must that of the reference crystal otherwise the system becomes dispersive.

The Double Crystal Technique is very sensitive to lattice distortion or misorientation. The rocking curve obtained is just the convolution of the two perfect crystal reflecting curves and has a width around 1.4 times the perfect crystal reflecting range. This can be explained by reference to the Du Mond diagram [8] which is a graphical demonstration of Bragg's law [1]. Diffraction will only occur when the curves of the two crystals overlap. The Bragg planes of both crystals are parallel and equispaced, hence the curves overlap for all values of λ and θ satisfying reflection, as

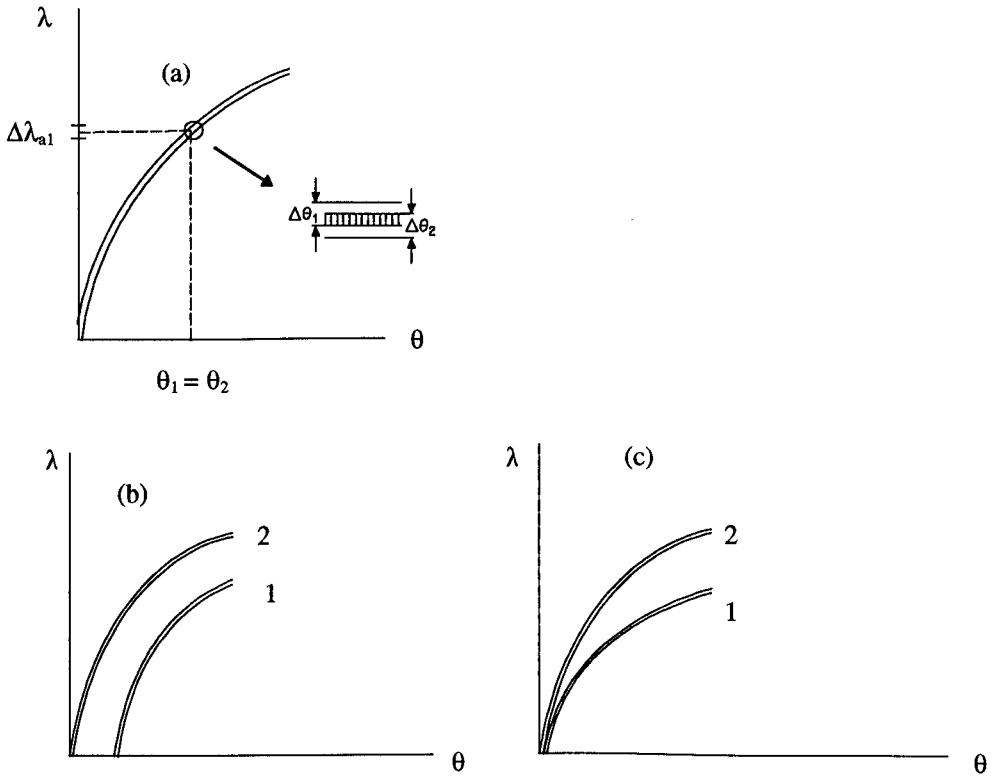

Figure 2.3: Du Mond diagram in the (+-) parallel setting for (a) Two perfect crystals. (b) Local rotation of the lattice in the second crystal. (c) Local dilation in the second crystal.

can be shown in the shaded area figure 2.3a. If a local misorientation is present in the second crystal, thus the curve is misplaced and intensity loss occurs, figure 2.3b. Likewise, no diffraction occurs if a distortion is present within the second crystal and the corresponding Du Mond diagram is shown in figure 2.3c.

2.2.2.3 High Resolution Double Axis Diffractometer

The x-ray beam is collimated to produce a low divergence beam which then passes through a 220 double bounce channel-cut Si beam conditioner. The purpose of which is to reduce the intensity in the wings of the Bragg reflection. The beam is then monochromatised using a 111 cut Si crystal mounted on the first axis of the diffractometer, figure 2.4. The anti-parallel setting of this crystal crosses the Du Mond curves, figure (2.5), and serves to select a portion of the Cu $K\alpha_1$ emission line of approximately the same angular width as the 111 Si reflection, that is approximately 8 arc seconds [1]. The result is a beam of ultra-low angular divergence and wavelength spread. This beam falls on the sample which is placed on the second axis of the diffractometer, having passed through two slits to define the footprint of the beam on the sample. The combination of the complex x-ray optical path and the various slits serve to reduce the background scatter and improve the signal to noise ratio dramatically. In this technique both crystals do not have to have the same lattice

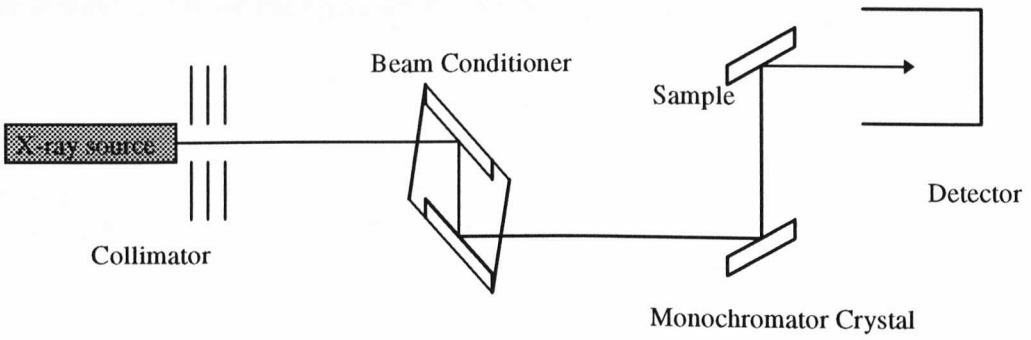

Figure 2.4: High Resolution Double Axes Diffractometer.

parameter. The Du Mond diagram for the (++) setting is shown in figure 2.5. Both crystals have equal plane spacings but non parallel Bragg planes [1]. Only a narrow

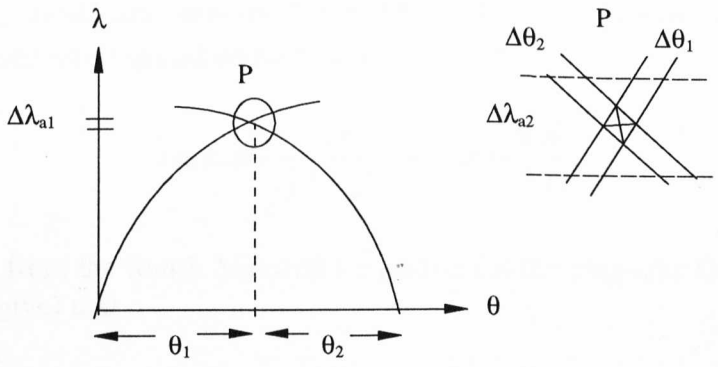

Figure 2.5: Du Mond diagram for the (++) double crystal setting.

band of wavelengths will be diffracted for any kind of crystal orientation, thus the system becomes effectively non-despersive. Now if a local misorientation exist in the second crystal, the intersection point P of the two curves moves along the curves and little change is noticed, and no loss of intensity occurs.

2.2.3 An Introduction to the Theory of X-ray Diffraction

2.2.3.1 The Kinematical Theory

We can consider x-ray diffraction as the specular reflection of x-ray from lattice planes, hence we can apply Bragg's equation (2.1) which gives us the condition at which maxima of diffracted intensity occur.

Kinematical theory [1], [7], [9], [10] assumes that each unit cell sees the same amplitude of the incoming wave, and no rediffraction, i.e. a negligible amount of energy is lost from the incident beam. This is only true for thin crystals of the order of 1μm and for Powder Diffraction, but it is not valid for thick and perfect crystals.
A theory which takes into account all the wavefields propagating within the crystal volume is needed. This is the Dynamical Theory.

2.2.3.2 The Dynamical Theory in a Perfect Crystal

A solution of Maxwell's equations in a periodic medium matched to solutions which are plane waves outside the crystal are needed [1], [11], [12].
The third Maxwell equation [1] can be written as :

$$curl\,\vec{E} = -\frac{\partial\,\vec{B}}{\partial\,t} \tag{2.2}$$

Where $\vec{E}$ is the electric field and $\vec{B}$ is the magnet induction. We know that the electric displacement $\vec{D}$ equals :

$$\vec{D} = \varepsilon_o (1+\chi)\vec{E} \tag{2.3}$$

Where $\chi \equiv \chi_e$ is the electric susceptibility and $\vec{B} = \mu_0 \vec{H}$. Then we substitute equation (2.3) in (2.2) and take the curl on both sides :

$$curl\,curl\frac{\vec{D}}{(1+\chi)\varepsilon_0} = -curl\frac{\partial\,\vec{B}}{\partial\,t} \tag{2.4}$$

But we know from the fourth Maxwell's equation for the magnetic field (in the case of no current to give) that :

$$curl\vec{H} = \frac{\partial\,\vec{D}}{\partial\,t} \tag{2.5}$$

Substituting equation (2.5) in (2.4) and using the approximation that $\frac{1}{1+\chi} = 1-\chi$ where χ is very small in the x-ray region - typically $\approx 10^{-5}$ [7] and the velocity of light in vacuum is $C = \frac{1}{\sqrt{\varepsilon_0 \mu_0}}$, we can write :

$$curl\, curl(1-\chi)\vec{D} = -\frac{1}{C^2}\cdot\frac{\partial\, \vec{D}}{\partial\, t^2} \tag{2.6}$$

The solution gained by this must reflect the periodicity of the crystal lattice, and such functions are identified as Bloch functions. We can write equation (2.5) in a periodic medium as following :

$$\vec{D} = \sum_g \vec{D}_g \exp\left(-2\pi\, i\vec{K}_g\, \vec{r}\right)\exp(i\omega\, t) \tag{2.7}$$

and the susceptibility can be expanded as a fourier series over the reciprocal lattice as:

$$\chi = \sum_h \chi_h \exp\left(-2\pi\, i\vec{h}\,\vec{r}\right) \tag{2.8}$$

where $\chi_h = -\frac{r_e\, \lambda^2 F_h}{\pi\, V_c}$, F_h is the structure factor, V_c is the volume of the unit cell and $r_e = \frac{e^2}{m_e\, c^2}$ is the classical electron radius. Employing the Laue equation, which link the reciprocal lattice vectors $\vec{g}$ and the diffracted wavevectors $\vec{K}_g$:

$$\vec{K}_g = \vec{K}_0 + \vec{g} \tag{2.9}$$

and substituting (2.8) and (2.7) into (2.6) leads, after some manipulations, to the fundamental equation of the dynamical theory [1] :

$$\sum_h \left[\chi_{g-h}\left(\vec{K}_g\cdot\vec{D}_h\right)\vec{K}_g - \chi_{g-h}\left(\vec{K}_g\cdot\vec{K}_g\right)\vec{D}_h\right] = \left[k^2 - \left(\vec{K}_g\cdot\vec{K}_g\right)\right]\vec{D}_g \tag{2.10}$$

where $k = \frac{\omega}{c}$ is the vacuum wavevector. As the Ewald sphere [1] for the x-ray case is large, it is unexpected that more than one reciprocal lattice point provide a diffracted wave of considerable amplitude. Thus, two waves are considered to have appreciable amplitude in the crystal, one for the incident and one for the diffracted wave. Equation (2.10) then reduces to :

$$\chi_g(\vec{K}_g\cdot\vec{D}_0)\vec{K}_g-\chi_g(\vec{K}_g\cdot\vec{K}_g)\vec{D}_0+\chi_0(\vec{K}_g\cdot\vec{D}_g)\vec{K}_g-\chi_0(\vec{K}_g\cdot\vec{K}_g)\vec{D}_g = (k^2-\vec{K}_g\cdot\vec{K}_g)\vec{D}_g \tag{2.11}$$

$$\chi_{\bar{g}}(\vec{K}_0\cdot\vec{D}_g)\vec{K}_0-\chi_{\bar{g}}(\vec{K}_0\cdot\vec{K}_0)\vec{D}_g+\chi_0(\vec{K}_0\cdot\vec{D}_0)\vec{K}_0-\chi_0(\vec{K}_0\cdot\vec{K}_0)\vec{D}_0 = (k^2-\vec{K}_0\cdot\vec{K}_0)\vec{D}_0 \tag{2.12}$$

Taking the scalar product of (2.11) with $\vec{D}_g$ and (2.12) with $\vec{D}_0$ and bearing in mind that $\vec{K}_0\cdot\vec{D}_0=\vec{K}_g\cdot\vec{D}_g=0$, we gain the following :

$$k^2C\chi_{\bar{g}}\vec{D}_g+\left[k^2(1+\chi_0)-\vec{K}_0\cdot\vec{K}_0\right]\vec{D}_0=0 \tag{2.13}$$

$$\left[k^2(1+\chi_0)-\vec{K}_{\bar{g}}\cdot\vec{K}_{\bar{g}}\right]\vec{D}_g+k^2C\chi_g D_0=0 \tag{2.14}$$

where $C=\vec{D}_0\cdot\vec{D}_g$ = 1 for σ polarisation
= $\cos 2\theta_B$ for π polarisation.

For non-trivial solution

$$\begin{vmatrix} k^2C\chi_{\bar{g}} & k^2(1+\chi_0)-\vec{K}_0\cdot\vec{K}_0 \\ k^2(1+\chi_0)-\vec{K}_g\cdot\vec{K}_g & k^2C\chi_g \end{vmatrix}=0. \tag{2.15}$$

considering

$$\alpha_0=\tfrac{1}{2}k\left[\vec{K}_0\cdot\vec{K}_0-k^2(1+\chi_0)\right] \tag{2.16}$$

$$\alpha_g=\tfrac{1}{2}k\left[\vec{K}_g\cdot\vec{K}_g-k^2(1+\chi_0)\right] \tag{2.17}$$

We come to

$$\alpha_0\alpha_g=\tfrac{1}{4}k^2C^2\chi_g\chi_{\bar{g}} \tag{2.18}$$

2.2.3.3 The Dispersion Surface Concept

We show briefly here the dispersion surface concept [1], which is considered one of the most substantial and beneficial concepts relating to dynamical diffraction theory. Equation (2.18) can be represented geometrically as following. We draw first two spheres of radii k and nk about the origin and the reciprocal lattice point G (where $OG=\vec{g}$) respectively, as shown in figure 2.6. Where $\left|\vec{K}_0\right|=nk=k\left(1+\frac{\chi_0}{2}\right)$ is

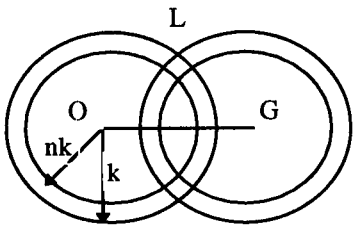

Figure 2.6: Ewald spheres in the reciprocal space around the lattice points 0 and G.

the wavevector inside the crystal and n is the refractive index. Strong diffraction will only occur close to intersection, the Laue point, as long as the Laue equation (2.9) is satisfied. The magnified region close to the Laue point is shown in figure 2.7. The arcs AB and A'B' belong to the spheres with radius k and the arcs CD and C'D' to

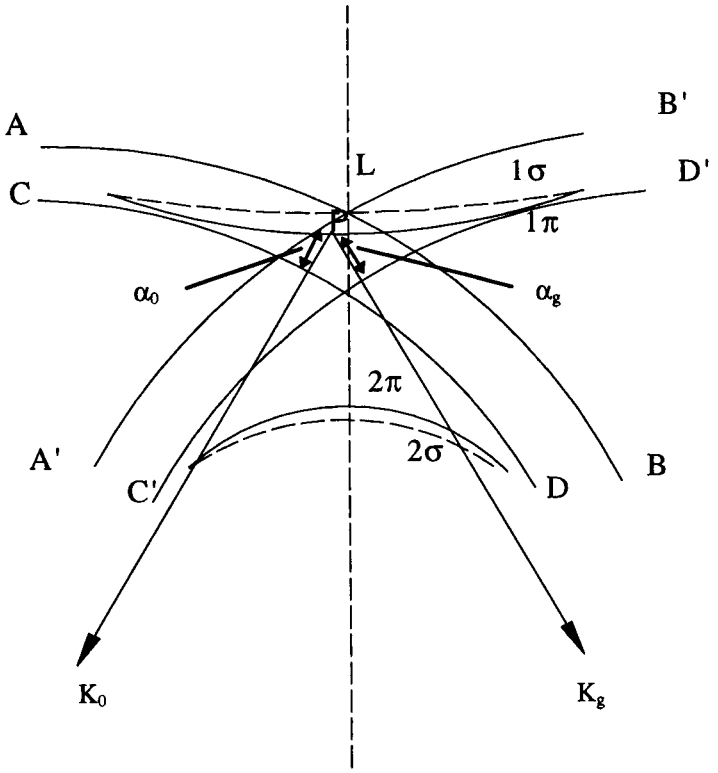

Figure 2.7: The dispersion surface configuration.

those of radius nk. The dispersion surface equation (2.18) determines a hyperbolic where each branch contains two components, one for π and the other for σ polarisation. Any wave propagating in the crystal ought to have two vectors $\vec{K}_0$ and $\vec{K}_g$ laying on

the dispersion surface, then equation (2.7) can be rewritten and the amplitude of the wave becomes :

$$\vec{D} = \exp(i\omega\ t)\left[\vec{D}_0 \exp\left(-2\pi\ i\vec{K}_0 \cdot \vec{r}\right) + \vec{D}_g \exp\left(-2\pi\ i\vec{K}_g \cdot \vec{r}\right)\right] \qquad (2.19)$$

The amplitude ratio [1] is given by :

$$X = \frac{D_g}{D_0} = \frac{2\alpha_0}{Ck\chi_{\bar{g}}} = \frac{Ck\chi_g}{2\alpha_g} \qquad (2.20)$$

where α_0 and α_g are the perpendicular distances from the tie point P to the spheres with radius nk. It is clear that not only the wavevector can be determined from the position of the tie point on the dispersion surface but also the amplitude. The relative strength of the incoming and the diffracted beams emerging from the crystal thus depend on α_0 and α_g which in turn depends on the deviation $\Delta\theta$ of the incident beam from the exact Bragg angle. In fact the dispersion surface concept is applied only for perfect crystals. Both Takagi and Taupin [9], [13], [14], [15] have made a generalised diffraction theory which deals with diffraction of both x-ray and electrons in perfect and imperfect crystals.

2.2.3.4 Takagi-Taupin Diffraction Theory

This theory deals with the passage of x-ray through a crystal with any kind of lattice distortion. Taking into account the two-beam approximation (i.e. only the forward and diffracted beam wavefields have appreciable intensity), and that wavefield inside the crystal is described in a differential form [16], then we can write :

$$\frac{i\lambda}{\pi}\frac{\partial \vec{D}_0}{\partial \vec{s}_0} = \chi_0 \vec{D}_0 + C\chi_{\bar{g}}\vec{D}_g \qquad (2.21)$$

$$\frac{i\lambda}{\pi}\frac{\partial \vec{D}_g}{\partial \vec{s}_g} = \left(\chi_0 - \alpha_g\right)\vec{D}_g + C\chi_g \vec{D}_0 \qquad (2.22)$$

where $\vec{D}_0$ and $\vec{D}_g$ are the amplitude of the wave in the forward and diffracted beam directions, $\vec{s}_0$ and $\vec{s}_g$ are the forward and diffracted beam directions (unit vectors in the directions of $\vec{K}_0$ and $\vec{K}_g$), and α_g represents the deviation of the incident wave from the exact Bragg condition, which is given by :

$$\alpha_g = -2\Delta\theta_g \sin 2\theta_B \qquad (2.23)$$

where $\Delta\theta_g$ is the local deviation from the exact Bragg angle, taking into account the lattice strains, and θ_B is the local exact (vacuum) Bragg angle . The Takagi-Taupin equations (2.21) and (2.22) can be solved analytically and the resulting amplitude ratio is described as :

$$X = \frac{X_0\sqrt{BB-EA}+i(BX_0+E)\tan\left(D\sqrt{BB-EA}\,[z-w]\right)}{\sqrt{BB-EA}+i(AX_0+B)\tan\left(D\sqrt{BB-EA}\,[z-w]\right)} \tag{2.24}$$

where :

$$A = C\chi_{\bar{g}}$$

$$B = \frac{(1-b)\chi_g + \alpha_g \pi}{2}$$

$$D = \frac{\pi}{\lambda\gamma_0}$$

$$E = -Cb\chi_0$$

and $b = \frac{\gamma_0}{\gamma_g}$ is the ratio of the direction cosines of the incident and reflected beams relative to the inward surface normal, z is the depth above the depth w at which the amplitude ratio is the known value X.

For structures of multiple layers, using the RADS computer calculations [16] described in a following section, the amplitude ratio (2.24) is summed from each layer repeatedly until all the layers are scanned and the direct and diffracted intensities are exactly determined. In fact the Takagi-Taupin equations are extremely important for calculating the intensities of the incident and diffracted beams for perfect as well as imperfect crystals.

2.2.4 Rocking Curve Analysis by Dynamical Simulation

Simulation of rocking curves is an extremely powerful method of interpretation of Complex Structures (Multiple or Graded Layers). Modelling the diffraction profiles of thin film semiconductor heterostructures is very reliable method for extracting thickness, composition and other structural parameters. Good agreement can be obtained between the measured profile and a proposed model structure provided that we have insignificant number of defects (i.e. high-quality lattice-matched semiconductors). Using the theories of Takagi [14] and Taupin [15], the simulation of the diffraction profiles from near-perfect semiconductor structures can be successfully performed [12]. The simulation and interpretation of diffraction profiles from partially relaxed layer structures has been carried out [17] and valuable information were

obtained for this type of structures. Furthermore, interdiffusion in epitaxial multilayer structures has been modelled using x-ray simulation techniques [18].

The experimental rocking curves were analyzed using the RADS computer program (Rocking Curves Analysis By Dynamic Simulation) [16] and a theoretical simulations based on a model of the structure were compared with the experimental one. The simulation curves then can be altered until the best fit between the experimental and the simulation rocking curves is achieved [19]. For Superlattice or MQW structures, the diffraction profile contains satellite reflections located symmetrically around the Bragg reflection. The SL structure periodicity can exactly be obtained from the position of the satellites peaks and far more information can easily be calculated from the half widths and intensities of the satellites peaks such as the interface quality of the layers.

2.3 Optical Techniques

One of the major and substantial techniques for obtaining information about semiconductor structures is optical methods. Firstly, they are non-destructive; secondly they are very powerful and efficient tools for the observation of QW confinement, interface and defect states. For example the sample quality can be defined from the PL intensity, and the Mn concentration in CdTe/CdMnTe structures can be found by measuring the energy of the optical transition in CdMnTe layers.

2.3.1 Photoluminescence (PL)

Photoluminescence is a widely known non-destructive technique and a powerful tool in studying bulk materials, epitaxial layers, and low-dimensional structures such as quantum wells and superlattices.

When an electromagnetic wave in the visible part of the spectrum (such as a laser beam) is directed into a material, radiative transitions between the electronic "outer" energy levels within the material occur. If the exciting beam energy is greater than the bandgap of the material i.e. $h\nu > E_g$, electrons in the valence band are excited into the conduction band leading to positive holes being created in the valence band. The excited electrons then relaxes non-radiatively to the lowest energy level in the conduction band and the holes relaxes likewise to the highest energy level in the valence band. Furthermore, these electrons and holes may travel individually throughout the crystal as a free carriers. Another possibility is that an electron and a hole may coulombically be attracted to each other as a result of opposite charges creating what is so-called excitons. Excitons can be found in many forms such as free excitons, excitons bound to lattice defects and excitons bound to impurities sites. If the excited electrons and holes recombine radiatively, electrons drop from the conduction band into the valence band, then photoluminescence is generated in which photons of specific enegry are released. In fact, excitonic transitions are noticed in the PL at energies just below the bandgap of the material at issue owing to impurities states with energies within the forbidden gap. The principal recombination mechanisms observed in semiconductors are discussed below.

2.3.1.1 Fundamental Radiative Transitions in II-VI Semiconductors

I. Free Exciton Recombination

Excitons can be described in a similar way to the hydrogen model [20], their energies can be written as:

$$E_{ex}^{(n)} = E_g - \frac{\mu e^4}{2\hbar^2 n^2 \varepsilon^2} \quad ; \qquad n=1,2,3,.... \tag{2.25}$$

where ε is the dielectric constant, E_g is the material bandgap and μ is the reduced mass of the exciton which is given by:

$$\frac{1}{\mu} = \frac{1}{m_e^*} + \frac{1}{m_h^*} \tag{2.26}$$

where m_e^* and m_h^* are the electron and hole effective masses correspondingly. The principal quantum well number n denotes to the various exciton levels, in which the ground state is ascribed to $n=1$. The radius of the free exciton is then:

$$a_B^{ex} = \frac{\varepsilon n^2}{\mu} a_B \tag{2.27}$$

where $a_B = 0.53$ Å is the bohr radius of the hydrogen atom. The free exciton binding energy [21] is defined in equation (2.25) and can be written as:

$$E_b = \frac{\mu e^4}{2\hbar^2 n^2 \varepsilon^2} \tag{2.28}$$

Free excitons can wander throughout the crystal quite easily, therefore bound excitons emission can readily be recognised while free excitons emission is generally weak because momentum has to be conserved in emission, $\Delta k=0$. The free exciton translational energy is given by [21]:

$$E_T = \frac{\hbar^2 k^2}{2\left(m_e^* + m_h^*\right)} \tag{2.29}$$

Free exciton emission can be seen at low temperatures. The free exciton emission is observed at photon energy of:

$$h\nu = E_g - E_b \tag{2.30}$$

Upon exciton recombination, phonons must be emitted along with photons in order to obtain momentum conservation. In general, free exciton recombination is inefficient

since the probability of a phonon-assisted transition occurance is comparatively low. Furthermore, free exciton transitions can only be observed in semiconductors free of defects and impurities and exceptionally in quantum well structures of good quality where excitons can localise quite easily reducing their translational momentum to recombine and a photon with a chracteristic energy is produced in the process.

II. Bound Exciton Recombination

When a free exciton is trapped at neutral or ionized impurities sites, its translational momentum is effectively brought to zero, therefore bound exciton recombination becomes extremely efficient as no phonon emission is required for this process. In practically all II-VI semiconductors, domination of the bound exciton emission over free exciton emission occurs. This is due to the presence of residual levels of impurities which behave as trapping centres. Shallow neutral donors or acceptors are normally responsible for trapping free excitons leading to bound exciton to a neutral donor D^0X or bound exciton to a neutral acceptor A^0X, respectively. The energy in which bound exciton emission is produced is given by:

$$h\nu = E_g - E_b - E_L^{ex} \tag{2.31}$$

where E_L^{ex} is the localised exciton energy to a neutral impurity. As a matter of fact, E_L^{ex} can be used to identify impurities in semiconductors since its value is highly dependent on the nature of the trapping impurities or defects. This can be done by analysing the PL spectrum of the sample. Shallow bound neutral donors and acceptors emissions are usually detected at energies near the bandedge of the semiconductor, just below the free exciton energy.

III. D-A Pair Transitions

Donor-acceptor pair recombination (DAP) are mainly observed in semiconductors with high levels of impurities. This kind of recombination usually occurs when the hole of the neutral acceptor and the electron of the neutral donor experience a coulombic interaction. The recombination transition energy of this process is given by:

$$h\nu = E_g - E_D - E_A + \frac{e^2}{4\pi\varepsilon r} \tag{2.32}$$

where E_D and E_A are the donor and acceptor ground state energies respectively and r is the donor-acceptor separation. In general, DAP lines are broader than excitonic ones as a results of the separation value, r, being varied over a wide range. Furthermore, a series of phonons might be emitted in the D-A pair recombination process. DAP transitions are produced, in PL, at energies lower than those observed from the related excitonic transitions.

IV. Free-to-Bound Transitions

When a free hole recombines with a donor electron or when a free electron recombines with an acceptor hole, then transitions known as free-to-bound take place. The abbreviations of the previous transitions are ascribed as (D^0, h) and (e, A^0) respectively. This type of recombination is observed at energy of:

$$h\nu = E_g - E_{d,a} \tag{2.33}$$

where $E_{d,a}$ are the donor and acceptor ionization energy respectively. This transition occurs at energy lower than the excitonic transition and higher than the DAP one. Once more, a series of phonons might be emitted in the free-to-bound recombination process.

V. Deep level Transitions

Deep level transitions are produced in semiconductors as a result of the existence of impurities, dislocations, and stacking faults. Short range potentials are formed which cause deep energy levels to exist in the forbidden energy gap of the semiconductor[22]. Due to carrier trapping at these centres, undesirable long wavelength emission such as infra-red emission is produced in PL. As a matter of fact, this kind of emission can be used for the identification of the sample quality since its energy level depends on the impurities and structural defects in the sample. Furthermore, the ratio of the band edge transition intensity to the deep centres transition intensity can indicate whether the sample quality is good or not. Deep level transitions are usually very broad and often very difficult or impossible to be identified in the PL spectrum. This is due to the broad nature of the linewidths of such transitions and also the overlapping features of the various emission bands.

2.3.1.2 PL Technique Set-Up

Figure 2.8 shows a schematic diagram of the PL technique set-up. The sample was enveloped with aluminium foil with a small hole cut into the front face to let the laser beam pass through. The sample was mounted on a five-face copper rod using Oxford Instrument G.E Low Temperature Varnish. The rod was inserted into an Immersion Cryostat filled with liquid helium allowing the temperature to cool down to 4.2 K. The idea behind wrapping the sample with the aluminium foil is to prevent any strain of the sample layers or sample breakage to be introduced when the adhesive varnish solidifies (due to thermal contraction). The temperature of the liquid helium could be brought down to 1.8-2 K by overpumping it to a pressure of 10 to 25 torr. Liquid helium becomes super-fluid below the λ-point, 1.8 K. The principle advantage is to provide a clear and stable optical access to the sample. The sample was usually excited by a Spectra-Physics 2045 Argon Ion Laser capable of producing laser lines from the green to the ultraviolet region at 3005 Å.
The laser beam was directed onto the sample and the resulting emissions were collected by a number of mirrors and quartz lenses. The excitation power used in our measurements was 10-20 mW. The resulting photoluminescence was focused into the slit of a 1 m focal length SPEX monochromator. The monochromator has a resolution

of 0.8 nm per mm slit width. Regular calibration of the monochromator was achieved using a mercury lamp for the UV and visible region and a potassium lamp for the wavelength region of 7000-8000 Å. A multialkaline photomultiplier tube was used to measure the intensity of the dispersed light coming from the monochromator. To stop

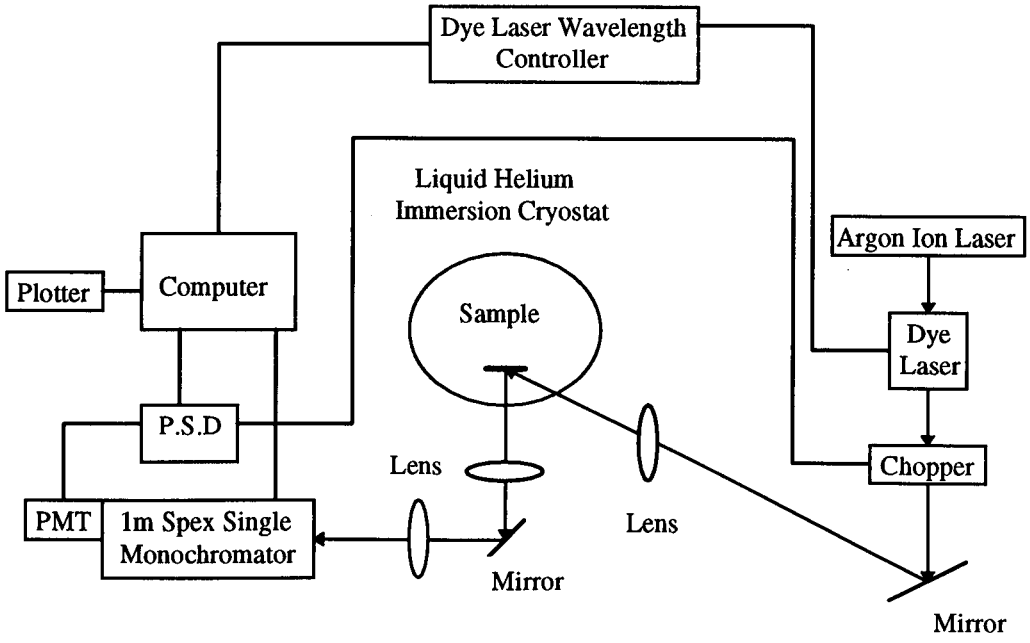

Figure 2.8. Schematic diagram of the Photoluminescence (PL) and Photoluminescence Excitation (PLE) techniques.

any laser lines or scattered light from entering the monochromator, suitable filters were used. The laser beam was chopped mechanically before entering the cryostat. The signal from the photomultiplier along with the reference signal from the chopper were then fed into a phase-sensitive detector. A personal computer was employed for the collection of data and for the control of the monochromator movement.

2.3.2 Photoluminescence Excitation (PLE)

A schematic diagram of the PLE experimental set-up can be seen in figure 2.8. This technique is very similar to the PL one from point of view of set-up but with some modifications. As the PL does, this method has the advantage of studying quite thin samples or even a single quantum well where the absorption methods fail to do so. Furthermore, information about higher energy states of the semiconductor and carriers combination processes can be quite readily obtained from the PLE spectrum. The excitation source was a coherent CR-599 1 W Pyridine Dye Laser pumped by an Argon Ion Laser. The spectral region of the dye was 690-780 nm. The principle of the PLE method can simply be explained as the following. The detection monochromator is set at a specific energy within the resulting PL spectrum and the exciting laser energy was

PAGE
MISSING
IN
ORIGINAL

2.3.4 Magnetic Field Dependent Method

Because of the existence of magnetic ions (Mn) in D.M.S (CdMnTe) structures, magnetic field experiments have become one of the most important tasks to perform on these structures. An Oxford Instruments Superconducting Magnet Cryostat was employed for the PL and PLE study. A schematic diagram of the magnet is depicted in figure 2.10. This magnet is capable of producing magnetic fields up to 13.5 Tesla providing that the magnet is cooled to a temperature of 2 K. The previous task is performed by overpumping the liquid helium in the sample space to a temperature below the λ point. The superconducting magnet consisted of concentric solenoid sections with windings formed from NbTi filaments and was enclosed by a copper radiation shield. An electric heater with a thermocouple placed near the sample was used to control the sample temperature. Optical access to the sample was performed in the Faraday configuration i.e. the emission from the sample is parallel to the magnetic field direction. In order to achieve a circularly polarised, σ^+ or σ^-, excitation quarter-wave plates were positioned into the laser beam. The luminescence from the sample was collected by large mirrors into the monochromator and then detected by PMT and the signal stored in a computer.

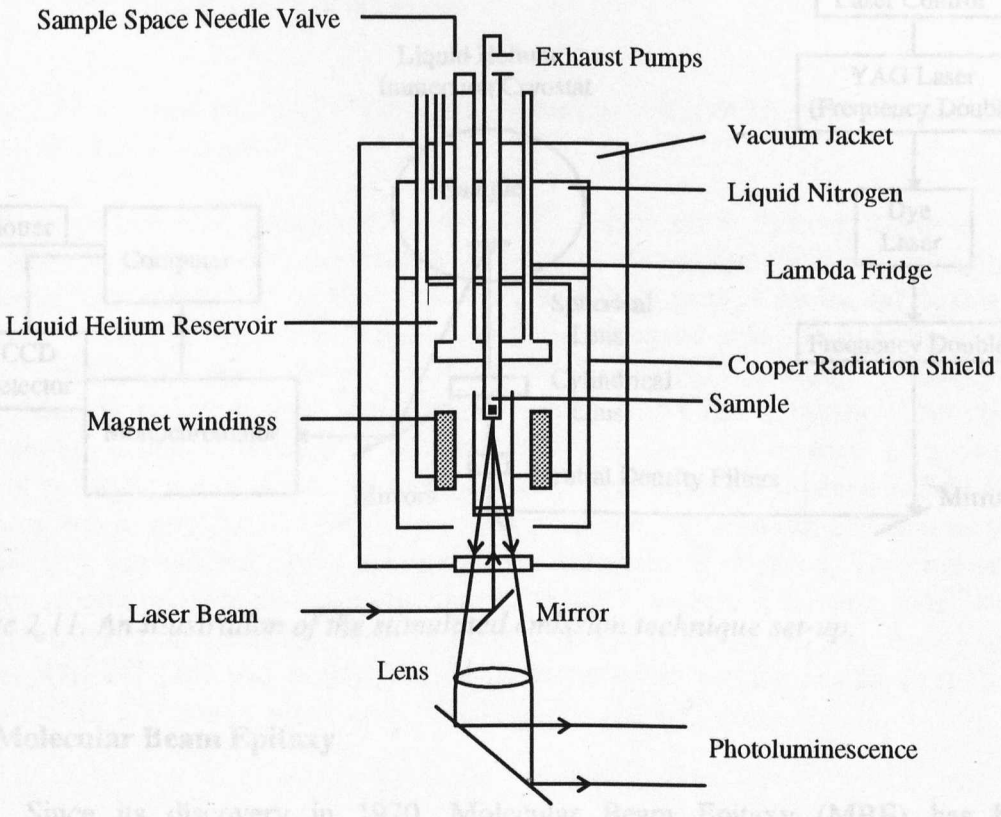

Figure 2.10. A schematic diagram of the superconducting magnet with the optical path.

2.4 Stimulated Emission Technique

Figure 2.11 illustrates a schematic diagram of the stimulated emission set-up. The excitation source was usually a Nd-YAG laser supplied with a frequency doubler which can emit laser pulses of wavelengths about 532 nm. The laser beam then pumps a DCM dye laser with an output in the spectral region of 600-700 nm. The resulting beam is then frequency doubled which in turn produces a UV pulse beam with a wavelength of 308 nm and a pulse width of 7 ns. Neutral density filters were employed to control the laser power. A cylindrical lens was utilised to focus the beam into a narrow line followed by a spherical lens to refocus the line onto the sample. Different mirrors were used where it was necessary to direct the beam into a variable temperature liquid helium immersion cryostat. The sample was mounted on a double-faced copper headed rod in the cryostat. The minimum temperature of the sample in the cryostat was 4-6 K. The resulting emission from the sample entered a monochromator and was detected using a CCD detector. A personal computer, provided with a special software, was used for data collection.

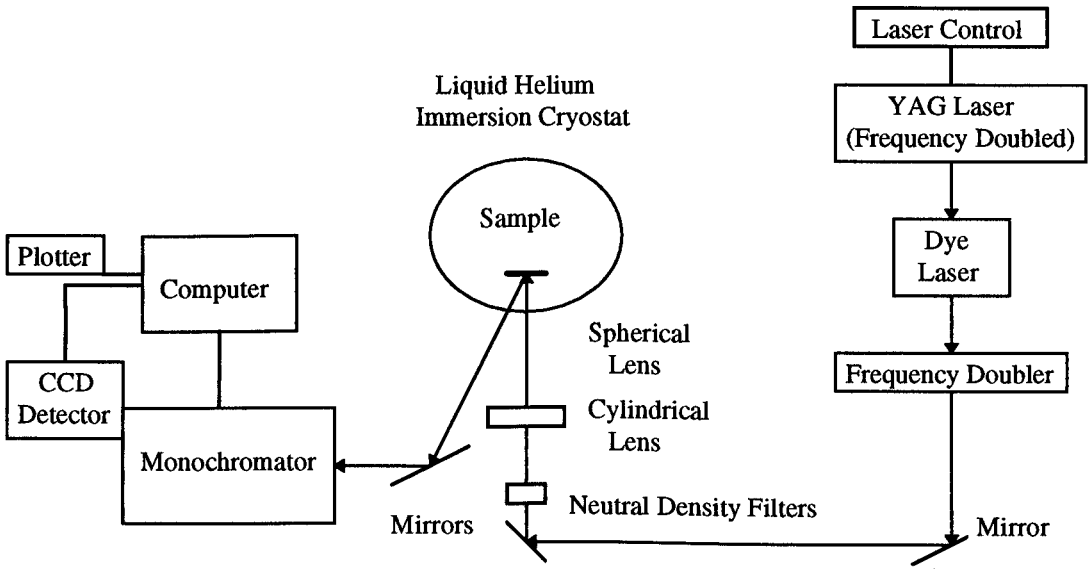

Figure 2.11. An illustration of the stimulated emission technique set-up.

2.5 Molecular Beam Epitaxy

Since its discovery in 1970, Molecular Beam Epitaxy (MBE) has been considered the finest technique for growing II-VI semiconductor structures. GaAs was the first material to be grown by Molecular Beam Epitaxy [23]. In 1978, Gaj et al [24] reported the MBE growth of CdTe thin films. After that the MBE growth of $Cd_{1-x}Mn_xTe$ multilayer structures was performed by Kolodziejsky at el [25], [26] in

1984. Subsequently substantial progress was achieved and vast amount of MBE growth was reported. The great importance behind the MBE growth technique is that high quality epilayers and heterostructures with a tremendous precision can be obtained [27].

The CdTe/CdMnTe and ZnS/ZnCdS samples studied in the current thesis were grown using a VG Semicon V80H MBE system as illustrated in figure 2.12. The

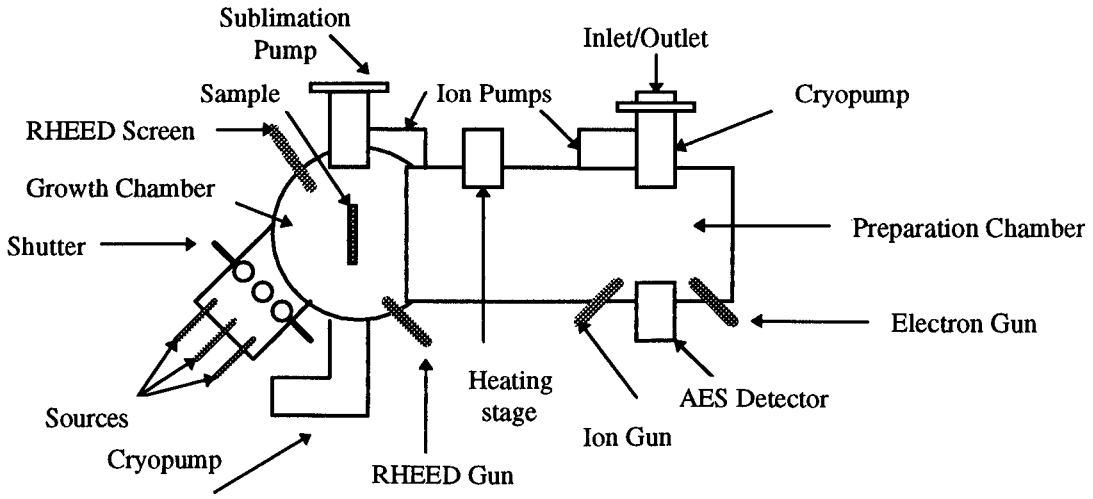

Figure 2.12. A schematic diagram of the VG Semicon V80H MBE system employed for the growth of II-VI samples.

growth procedure was carried out by Dr. D. E. Ashenford at the University of Hull. Ultra-High Vacuum (UHV) conditions of about 10^{-11} torr were applied and rigorous cleanliness was needed to produce materials with high purity. Molecular beams are produced by heating the source materials to the sublimation point. Consequently these beams chemically react when reaching the substrate forming a compound semiconductor which in turn is deposited epitaxially on the substrate. The source materials are usually contained in Knudsen cells and each cell consists of a crucible made of pyrolytic boron nitride. Generally slow growth rates are obtained via the MBE system which is very suitable for the research purposes but from the commercial point of view it is not desired where a large-scale production is required. To monitor the epilayer growth process, several techniques were used , namely Reflection High Energy Electron Diffraction (RHEED), Auger Electron Spectroscopy (AES) and the Ionisation Gauge. RHEED [28] was regularly used to monitor the surface morphology of the epilayer while it grows progressively.

References

[1] X-ray Diffraction Topography, edited by B. K. Tanner, Pergamon Press, Oxford (1976).

[2] Element of X-ray Crystallography, edited by L. V. Azaroff, McGraw-Hill Book Company (1968).

[3] X-ray Crystallography, edited by M. M. Woolfson, Cambridge University Press (1970).

[4] Methods In X-ray Crystallography, edited by J. W. Jeffrey, Academic press London (1971).

[5] C. W. Tu, J. S. Harris, Jr. Molecular Beam Epitaxy, Elsevier Science Publishers B.V.(1991).

[6] Paul. F. Fewster, Semicond. Sci. Technol. 8 (1993) 1915-1934. Printed in the UK.

[7] I.Karla, M.Sc Thesis, University of Hull, (1994).

[8] Du Mond. J. W. M, Phys. Rev. 52, 872-83. (1937).

[9] X-ray Diffraction, edited by A. Guinier, W.H.Freeman and Company London (1963).

[10] W. Z. Shen, S. C. Shen, J. App. Phys. 80, 10, pp. 5941-5944 (1996).

[11] C. R. Wie, T. A. Tobrello, and T. Vreeland, Jr, J. appl. phys . 59, 11 (1986).

[12] P.F.Fewster , C.J.Curling: J. Appl. Phys. 62, 10, (1987).

[13] S. Takagi, and H. H. Wills, Acta. Cryst.15, 1311 (1962).

[14] S. Takagi, J. Phys. Soc. Japan 26 1239-53.

[15] D. Taupin, Bull. Soc. Fr. Mineral. Cristallogr. 57, 469-511 (1964).

[16] RADS Computer Program, from Bede Scientific Instruments Ltd. Version 2.00, (1993).

[17] P. F. Fewster, J. Appl. Cryst. 25, 714-723 (1992).

[18] J. H. C. Hogg, D. Shaw, and D. M. Staudte, Applied Surface Science. 50, 87-91 (1991).

[19] D. E. Ashenford, J. H. C. Hogg, D. Johnson, B. Lunn, C. G. Scott, and D. Staudte, J. Cryst. Growth. 101, 157 (1990).

[20] Introduction to Solid State Physics, edited by C. Kittel, 7th Edition, John Wiley & Sons, NewYork, Chapter 11, pp. 305-332 (1996).

[21] Optical Processes in Semiconductors, edited by J. I. Pankove, Prentice-Hall, Inc., Inglewood Cliffs, Chapter 1, Section 1-D, PP. 12-17 (1971).

[22] K. A. Dhese, PhD Thesis, University of Hull (1993).

[23] Molecular Beam Epitaxy 1988, edited by Y. Shiraki and H. Sakaki, Elsevier Science Publishers B.V. (1988).

[24] J. A. Gaj, J. Ginter, and R. R. Galazka, Phys. Stat. Sol. B 89 pp 655 (1978).

[25] L. A. Kolodziejski, T. Sakamoto, R. L. Gunshor, and S. Datta, Appl. Phys. Lett. 44, pp 799 (1984).

[26] R. N. Bicknell, R. W. Yanka, N. C. Giles-Taylor, D. K. Blanks, E. L. Buckland, and J. K. Schetzina, Appl. Phys. Lett. 45, 92 (1984).

[27] C. T. Foxon and B. A. Joyce in " Growth and Characterisation of Semiconductors", Ed. R. A. Stradling and P. C. Klipstein (Adam Higler/ I.O.P. Publishing Ltd). pp. 35-64 (1990).

[28] T. J. Gregory, Ph.D. Thesis, University of Hull (1990).

Chapter 3

Magneto-optical and Diffusion Study of Pulsed Laser Annealed CdTe/CdMnTe Superlattices

3.1 Introduction

The processing and modification of the surface layers of semiconductors using directed energy sources such as lasers and electron beams has created a new area of materials science (directed energy processing). The spatial and temporal control over the heat flow and the energy deposition by these beams has opened a wide range of new applications varying from growing crystals to quenching alloys into metastable states, and from depositing films to purifying surfaces. The majority of these applications are being achieved by supplying heat to materials in which the beam energy is transformed by different coupling mechanisms.

Pulse laser annealing of semiconductors was first carried out to remove the damage caused by the ion implantation [1]. Nevertheless, laser crystallisation techniques were far more successful in converting amorphous Si or polycrystalline Si on amorphous substrates into a single-crystal Si which in turn led to a new production of semiconductor devices. Moreover, pulse laser annealing process has the ability of producing materials with impurities concentration over the natural solubility limit. This is due to the rapid heating and cooling occurrence in the material which causes recrystallization, where substitutional impurities diffuse into native lattice sites. When the laser pulse is absorbed at the surface region of the target, it generates heating of the sample structure. This localised heat, which depends on the absorbed power, the laser pulse time and characteristics of the sample structure, can cause melting followed by recrystallization of the surface layers in extremely short times if the total pulse energy is sufficient to raise the temperature of the solid up to the melting threshold.

The aim of the present work is to study in detail pulsed laser annealing effects (PLA) with CdTe/CdMnTe superlattice structures. In order to explore fully the behaviour of PLA, a novel method is used to show that these processes can be represented by a simple model which calculates the temperature rise as a function of the

pulse time and the depth into the sample for different laser fluences. The predictions of the model can then be compared to data extracted from the PLA of a MQW structure. The idea is that, as diffusion coefficients are strongly dependent on the temperature, depth resolution may be achieved because wells at different depths will experience different degrees of atomic diffusion. Further, by using a magnetic superlattice structure such as CdTe/CdMnTe, magneto-optical measurements such as PL and PLE can be carried out easily. The experiments give detailed information about the MQW structure after PLA. The energies of the different resulting optical transitions can be compared to calculated values, from which the amount of diffusion may be estimated.

3.2 Pulsed Laser Annealing of Semiconductors

During the past thirty years there has been a tremendous increase of research into, and the use of, transient annealing techniques and their applications to the processing of semiconductors. In fact most of the work was dominated by Si, nevertheless annealing processes of other semiconductors are still of great interest.

Fairfield and Schwuttki were the first to use pulsed lasers for producing alloy diodes in the late 1960's [2], but unfortunately no device applications were accomplished.

Indeed high power laser pulses have been used successfully to anneal damage in ion implanted semiconductors [3], convert amorphous into single crystalline layers [4-5], diffuse dopants into semiconductors deposited with thin layers of dopants [6], and to investigate growth of dislocations during laser annealing [7].

Since 1974, Soviet researchers [8] have claimed to have proved that remarkably high quality PLA Si, which has been widely reported, must be produced by some non-thermal process, while Italian, U.S., and other workers reported that the process is governed by simple thermal melting, rapid crystallisation and quench processes.

The event of melting produced by pulsed Ruby-laser (λ=0.694 μm) irradiation has been investigated by Narayan and White [9]. They found that the removal of dopant precipitates, dislocations, and loops during laser irradiation provides strong indication that melting is taking place. Also the melting depth can be calculated as a function of laser parameters (energy density and laser pulse duration) from the thickness of defect-free regions and lengths of reoriented dislocation segments, whereas Auston [10] has used the optical reflectivity changes of amorphous Si to identify annealing and melting transitions in pulse laser heated semiconductors.

In 1979, it was reported that the rapid liquid epitaxial regrowth which can be achieved by pulsed laser annealing of ion implanted Silicon is capable of incorporating dopants above equilibrium solid solubility limits [11], [12].

It has been shown also that the transition from the amorphous to the crystalline state occurs gradually under the pulsed laser irradiation [13]. Laser annealing of donor implanted GaAs using different laser sources has been reported [14]. Furthermore, laser annealing enhances the electrical activity in ion implanted Si [15] and GaAs [16].
Moreover, Pulsed annealing techniques have demonstrated the capability of obtaining good ohmic contacts on n-GaAs [17].

3.3 Basic Energy Deposition Principals by Laser Beams

3.3.1 Optical Properties of Materials

The interaction between high-intensity optical beams and matter has been studied over many years and many valuable aspects of matter have been discovered. When a material is exposed to electromagnetic radiation, only electrons will interact with it. Furthermore, core electrons are not affected by the small phonons energies of the electromagnetic beam. The optical properties of matter are indeed governed by the energy levels of the atoms' valence bound or free electrons. In fact, only a weak response is attained between the bound electrons and the electromagnetic wave which essentially affects the electrons' phase velocity, whereas, the free electrons can be energised by the incoming wave. These accelerated electrons can then reradiate their energy, which in turn is transmitted to the lattice. This reradiation of energy is the reason for reflection.

Since the excitation wavelengths λ are quite large compared to the atomic distance, the material response to this radiation can be explained in terms of averaged macroscopic quantities, for instance, the complex refractive index $\overline{n} = n + ik$. The ratio of phase velocities in a vacuum and in the material is represented by the real part of the complex refractive index, while the imaginary part describes the damping of the light wave. In fact, material response to light can be described by n and k. Nevertheless, when investigating the energy deposition it is more likely to employ the normal reflectivity R and the absorption coefficient α or the absorption length d concept. For normal incidence these parameters can be linked together with n and k by the following relation:

$$R = \left[k^2 + (n-1)^2\right] / \left[k^2 + (n+1)^2\right] \tag{3.1}$$

and

$$\alpha = 1/d = 4\pi\, k/\lambda \tag{3.2}$$

In the event of normal incidence of light with intensity I_0 (in W/cm^2) on a material, the power density φ (W/cm^3) absorbed at depth z can be written as

$$\varphi(z,t) = I_0(t)\left[1 - R/d\right]e^{-z/d} \tag{3.3}$$

Furthermore, the beam fluence F (J/cm^2) which is the time integral of the intensity I_0, is used to describe the excitation beam. When dealing with materials with a totally filled valence band, the exciting photons can give rise to two types of electronic transitions, specifically, intraband (bound-bound) and band to band (bound-free). Resonant coupling to high-frequency phonons (in accord to bound electrons) can be seen.

If the photon energy of the exciting wave $h\nu << E_g$ (semiconductors in the IR region), only intraband and phonon absorption can be observed. Weak coupling is yielded in this case. The absorption lengths d vary usually from centimetres to meters and sharp decline of the absorption length as a function of intensity or temperature is

expected to happen. In essence, this is undesirable for beam heating. However, when the photon energy $h\nu$ comes closer the material band gap energy, band-to-band transitions are more likely to happen, thus a distinct increase of the absorption level is observed.

Two categories of materials have to be considered here, specifically, direct and indirect band gap materials. In the case of direct transitions, the absorption coefficient is related to the photon energy by [18] :

$$\alpha_d = A\left(h\nu - E_g\right)^{1/2} \qquad \text{for } h\nu \geq E_g \tag{3.4}$$

While the dependence of the absorption coefficient on the photon energy of the indirect transitions can be written as :

$$\alpha_i = B\frac{\left(h\nu - E_g + E_p\right)^2}{\exp\left(E_p/kT\right)-1} \quad \text{for } E_g - E_p < h\nu < E_g + E_p \tag{3.5}$$

$$\text{or } \alpha_i = B\left[\frac{\left(h\nu - E_g + E_p\right)^2}{\exp\left(E_p/kT\right)-1} + \frac{\left(h\nu - E_g - E_p\right)^2}{1-\exp\left(-E_p/kT\right)}\right] \qquad \text{for } h\nu > E_g + E_p \tag{3.6}$$

where A and B are constants and E_p is the phonon energy.
In equation (3.5) only phonon absorption is permitted, while in equation (3.6) phonon emission is vigorously possible. Unfortunately, the above equations ignore detailed structure of the state density of the band edges and only consider single-phonon processes [18]. Up to now, we have briefly discussed principals of optical properties at low light intensities. The response of matter to sufficiently high light intensities, namely, laser beams, is altered by a number of mechanisms. We summarise below some of the effects which directly affect energy deposition.

I. Carrier Excitation

When a semiconductor is exposed to a beam of photons of energy $h\nu > E_g$, absorption occurs and excited carriers are produced at a rate of $1/t_e = I\sigma/h\nu$ where σ is the relevant absorption cross section [19]. Furthermore, at high absorbed intensities I, this rate may approach or even overcome the rate of carrier relaxation resulting in substantial changes in the energy distribution of the carriers. These changes are quite different to what we have experienced for the optical properties at low light intensities. Relaxation of hot carriers is not an easy task to tackle, however, for simplicity, we only consider two independent mechanisms, specifically, carrier-lattice collisions (at a rate $1/t_c$) and recombination (at a rate $1/t_r$). Normally, $1/t_c > 1/t_r$. Thus for the sake of increasing the power density, two systems can be identified. In the case of $1/t_e > 1/t_r$ an important increase of free carriers density occurs, which sequentially rules the optical properties. Once more, if $1/t_e > 1/t_c$ the energy gain of the carriers overcomes that rate

of energy loss to the host lattice. As a result a hot carrier plasma is generated which is no longer in thermal equilibrium with the lattice.

II. Thermal Effects

If the laser pulse energy is sufficiently high enough to elevate the temperature of the solid, then the optical properties of the solid material can change for two primary reasons :

(a) Phonons at elevated temperatures are induced, consequently these phonons undergo an interaction with the photons or with the carriers. We understand that phonons are very important for light absorption in indirect semiconductors at photon energy $h\nu$ close enough to the energy band gap E_g. When the lattice temperature increases, more phonons are generated and an effective increase of the phonon absorption probability takes place, as equation (3.5) confirms. Moreover, phonons deliver energy from the carriers into the lattice. As a result the increase of the carrier- lattice collision rate $1/t_c$ is accompanied by an increase of the lattice temperature. Also at photon energies of $h\nu << E_g$, thermally excited carriers are quite possible to be produced.

(b) Thermal effects can also induce changes in band gap structure. This effect may lead to increase or decrease in the absorption level. In the majority of semiconductors, the band gap energy decreases with increasing temperature. This concerns mainly the absorption coefficient at photon energies close to the semiconductor band gap energy.

However, when melting takes place in some semiconductors, metallic properties are produced [20] and a strong increase in α and R is observed. It is found also that when amorphous semiconductors crystallise, a decrease in α and R is found.

3.3.2 Laser Beams Induced Heating Effects

As we mentioned previously, absorption of laser beams usually generates excited electrons. These excited electrons then thermalize with a time constant of $t \leq 10^{-11}$ secs. When thermal equilibrium between the electrons and the lattice is reached, a fraction of the existed energy is dominated by lattice vibrations or phonons. The diffusion of phonons and carriers, thus, drives the heat from the absorption region into other parts of the material. This can be understood in terms of the thermal diffusivity. If the thermal diffusivity, D, is presumed to be constant, then the heat conduction expression can be written as the following :

$$\frac{\partial T}{\partial t} = D\nabla^2 T + \frac{A}{\rho C_p} \tag{3.7}$$

where ρ is the material density, C_p is the specific heat of the material and A is the rate of heat production per unit per volume. Since the beam has no effects on D (which may happen if a dense of carrier plasma is generated in a non-metal), then we may consider that the distribution of thermal energy production equals that of the absorbed beam power, i.e., $A=\varphi$, where φ is given by equation (3.3). Changes of the penetration depth

d and the reflectivity R occur as a result of the irradiation, consequently variations in the spatial distribution and the integrated value of A take place.

In most annealing procedures, control over the sample temperature is required to obtain the desired results. Nevertheless, especially in pulsed laser annealing, the process time is too small to permit any real time control. Furthermore, laser beams have a finite reproducibility and lateral variations in intensity exist. This in turn leads to a sample temperature variation, which should be minimised as far as possible. In fact the magnitude of the temperature variations rely on the dynamics of the heating process.

If a laser beam of a fluence F is directed into the surface of a sample of thickness L, then heat is created within a surface layer of thickness d (the absorption length for light). Throughout the time of the heat pulse of duration t, heat dissipates over a length of $\delta = 2\sqrt{Dt}$. If the sample thickness L is less than δ then the L substitutes δ in the following discussion. Two regimes need to be considered here :

I. If $d << \delta$, then heat is created at the surface of the sample only. The surface temperature at the end of the pulse is presented by :

$$T(0,t) = 1.13F(1-R)/\rho\ C_p \delta \tag{3.8}$$

The $T(F)$ slope in this regime depends mostly on the behaviour of $R(T)$ and $C_p(T)$. In respect to the case above and if $R(T)$ is constant, $T(F)$ tend to saturate while C_p increases with temperature. This situation is very significant since the material temperature does not vary a lot when considerable fluence variations take place. In fact, this regime is ideal for the processing of complex microstructures such as superlattices.

II. If $d >> \delta$, then heat is created throughout a large depth and the surface temperature in this case can be written as :

$$T(0,t) = F(1-R)/\rho\ C_p\ d \tag{3.9}$$

Here the behaviour of d as a function of temperature or fluence is critical. Actually, a strong decrease in the absorption length for light during irradiation can be related to various mechanisms. A decrease in d yields an increase in temperature, as long as the condition $d >> \delta$ is satisfied.

3.4 The Heat Flow Equation

3.4.1 Introduction

Two major parameters are needed to be taken into consideration when performing laser annealing of materials, namely, the pulse duration time (t) and the coupling depths of the heat source. The coupling of lasers to materials is very sensitive to the laser wavelength and the material state. The rate at which heat is dissipated in a material is represented by the heat diffusivity D which is given by :

$$D = \frac{k}{C_p.\rho} \tag{3.10}$$

where k, C_p, and ρ are the thermal conductivity, specific heat, and density of the material respectively.

The typical heat diffusion length L can then be written as :

$$L = (2Dt)^{1/2} \tag{3.11}$$

The absorbed energy A is given by :

$$A = (1-R)I.t \tag{3.12}$$

where R is the reflected energy, and I is the laser power density.
Subsequently, the average temperature rise in this $(2Dt)^{1/2}$ length in the target material could be written as the following :

$$\Delta T = \frac{(1-R)I.t}{C_p.\rho\,(2Dt)^{1/2}} \tag{3.13}$$

When the absorption length α^{-1} is less than the heat diffusion length i.e. $\alpha^{-1} < (2Dt)^{1/2}$, then the heating and cooling rates of the material could be represented by $(\Delta T/t)$. The composition and structure of the laser annealed material are mainly resolved from the cooling rate. Also we should be aware that the velocity of crystallisation of the molten layers is very significant parameter to investigate while performing the laser annealing process.

3.4.2 Analytical Solution of the Heat Equation in a Material

We present in this section the laser heating equation and its solution for a simple two-layer system [21]. The two-layer system was assumed to be composed of a thin film of thickness d on a thick substrate. The two layers were in perfect thermal contact. Several assumptions were taken into consideration in order to solve the heat equation. It was assumed that the incident laser irradiance q_0 on the front surface of the two-layer system is constant and that it is partly reflected and partly absorbed. Loss arising from thermal radiation was neglected. The physical parameters of the thin film and the substrate were assumed to be temperature independent. The heat flow was considered one-dimensional [22]. Moreover, it was assumed that no plasma is formed at the front surface for the considered values of the incident laser flux. The multireflections within the two-layer system were also neglected.

The heat diffusion equations for both the thin film and the substrate can be written as follows [21]. For the thin film layer:

$$\frac{\partial T_f(x,t)}{\partial t} = \alpha_f \frac{\partial^2 T_f(x,t)}{\partial x^2}, \quad t>0, \quad 0 \le x \le d; \tag{3.14}$$

For the substrate layer:

$$\frac{\partial T_p(z,t)}{\partial t} = \alpha_p \frac{\partial^2 T_p(z,t)}{\partial z^2}, \quad t > t_s, \quad 0 \le z \le \infty, z = (x-d); \tag{3.15}$$

Under the above conditions, equations (3.14) and (3.15) can be solved and the temperature in the film (subscript f) and the temperature in the substrate (subscript p) are given by [21]:

$$T_f(x,t) = \sum_{n=0}^{\infty} \frac{q_0 A_f}{\lambda_f} B^{n+1} \Big(\sqrt{4\alpha_f t/\pi}\, \exp\{-\frac{[2d(1+n)-x]^2}{4\alpha_f t}\}$$
$$-[2d(1+n)-x]\, erfc \frac{2d(1+n)-x}{\sqrt{4\alpha_f t}} \Big)$$
$$+\sum_{n=0}^{\infty} \frac{q_0 A_f}{\lambda_f} B^n \Big\{ \sqrt{4\alpha_f t/\pi}\, \exp[-\frac{(2nd+x)^2}{4\alpha_f t}] - (2nd+x)\, erfc \frac{(2nd+x)}{\sqrt{4\alpha_f t}} \Big), \tag{3.16}$$

$$T_p(z,t) = \sum_{n=0}^{\infty} \frac{2q_0 A_f}{\lambda_f} \frac{B^n}{(1+\varepsilon)} \Big(\sqrt{4\alpha_f t/\pi}\, \exp\{-\frac{[z\sqrt{\alpha_f/\alpha_p} + (1+2n)d]^2}{4\alpha_f t}\}$$
$$-[z\sqrt{\alpha_f/\alpha_p} + (1+2n)d]\, erfc\{\frac{[z\sqrt{\alpha_f/\alpha_p} + (1+2n)d]}{4\alpha_f t}\} \Big). \tag{3.17}$$

where :

T_f : Temperature in the film.
T_p : Temperature in the substrate.
q_0 : Laser flux.
A_f : Optical surface absorptance of the thin film, dimensionless.
λ_f : Thermal conductivity of the film.
α_f : Thermal diffusivity of the film.
α_p : Thermal diffusivity of the substrate.
t : Time variable.
t_s : Time transit, defined as the time taken for the excess temperature T of the rear surface of the thin film to change from zero.
d : Thickness of the thin film.
ρ : Density.
x,z : Spatial variables.

$$\varepsilon = \frac{\sqrt{\lambda_p \rho_p (C_p)_p}}{\sqrt{\lambda_f \rho_f (C_p)_f}}$$

$B = (1-\varepsilon)/(1+\varepsilon)$, $B<1$

Equations (3.16) and (3.17) are used latter to map out the temperature-time history at any depth within the material.

The temperature of the front surface is obtained by substituting x=0 in equation (3.16). This gives:

$$T_f(0,t)=\sum_{n=0}^{\infty}\frac{q_0 A_f}{\lambda_f}B^{n+1}\Big(\sqrt{4\alpha_f t/\pi}\exp\{-\frac{[2d(1+n)]^2}{4\alpha_f t}\}$$
$$-[2d(1+n)-x]erfc\frac{2d(1+n)}{\sqrt{4\alpha_f t}}\Big)$$
$$+\sum_{n=0}^{\infty}\frac{q_0 A_f}{\lambda_f}B^{n}\Big\{\sqrt{4\alpha_f t/\pi}\exp[-\frac{(2nd)^2}{4\alpha_f t}]-(2nd)erfc\frac{(2nd)}{\sqrt{4\alpha_f t}}\Big), \qquad (3.18)$$

3.5 Diffusion in Quantum Wells

Diffusion in semiconductor heterostructures has in recent years aroused increased general interest. The significance of diffusion in the post growth fine tuning of devices is an important area of research, as is the effect on the lifetime of devices, where diffusion during operation cannot be ignored. We present in this section the effects of manganese diffusion onto the shape of the quantum well profile.

The essential relations linking the material flux $\vec{J}$ with the concentration gradient $\vec{\nabla}c$ was first found by Fick. These are ascribed as Fick's first and second laws of diffusion [23][24]:

$$\vec{J}=-D\vec{\nabla}c \qquad (3.19)$$

$$\frac{\partial c}{\partial t}=div\left(D\vec{\nabla}c\right) \qquad (3.20)$$

where D is the diffusion coefficient and c is the concentration of atoms.
In fact the diffusion coefficient is a very strong function of the temperature T and can be expressed as:

$$D=D_0 e^{-\frac{Q}{kT}} \qquad (3.21)$$

where D_0 is a constant and Q is an activation energy.
For a constant diffusion coefficient (the linear case), Fick's second law, equation (3.20) can be written in one dimension (x) as :

$$\frac{\partial c}{\partial t}=D\frac{\partial^2 c}{\partial x^2} \qquad (3.22)$$

The solution of equation (3.22) is:

$$c = \frac{A}{\sqrt{t}} e^{-x^2/4Dt} \tag{3.23}$$

where A is an integration constant depends on the initial conditions. For an extended initial distribution of the diffusing material satisfying $c = c_0$ for $x < 0$, and $c = 0$ for $x > 0$ at the time $t = 0$, Crank [23] has deduced the following solution:

$$c(x,t) = \frac{c_0}{2} erfc\left(x/2\sqrt{Dt}\right) \tag{3.24}$$

Equation (3.24) describes the diffused material concentration in relation to the time and distance. Actually, this solution (under the assumption of linearity) can be superposed and combined for any MQW structure.

The extent of diffusion in a quantum well can be approximated by using the expression $l_d = 2[D(T)t]^{1/2}$ where l_d is the diffusion length and D is the diffusion coefficient. Figure 3.1 shows the diffusion profiles for manganese diffusion in an 75 Å CdTe well surrounded by $Cd_{0.85}Mn_{0.15}Te$ barriers for Dt values of [a] 0, [b] 10^2, [c] $3x10^2$, [d] $5x10^2$, [e] 10^3, and [f] $5x10^3$ Å^2. Examiniation of the diffusion profiles in figure 3.1 show that at the onset of diffusion the manganese close to the interface with the CdTe is able to move directly into the well. This results in raising the potential in the well and reducing the potential in the barrier close to the interface. Therefore on an energy scale the well appears to narrow at lower energies and widen at higher energies. Nevertheless, manganese eventually diffuses into the centre of the well, converting it into a dilute form of the barrier alloy. Hence the potential at the centre of the well is increased. This has the effect of increasing the apparent band gap. A meaningful characteristic of the CdTe/CdMnTe system is the 6:1 ratio of the effective mass of the heavy hole to that of the electron. This has the effect of a lower confinement energy and hence a higher degree of localisation for the hole, compared to the electron [25].

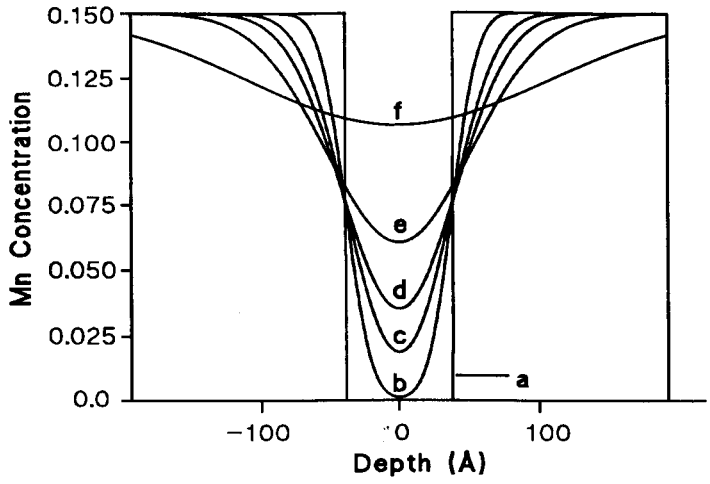

Figure 3.1: Caculated potential well profiles following diffusion of the Mn ions from the barrier region into the QW for Dt values of [a] 0, [b] 10^2, [c] $3x10^2$, [d] $5x10^2$, [e] 10^3, and [f] $5x10^3$ Å^2.

3.6 Interface and Surfaces

In surface processing materials, it is necessary to study the motion of the crystalline interface. When melting of the surface layers of the target occurs, this in general is followed by rapid increase of the crystalline velocity. This behaviour can be explained in terms of the much higher mobility of the atoms in the liquid phase and the very high temperature gradient present in laser annealing.

Both, Baeri and Campisano [15] show that the recrystallisation velocity can be varied by means of the temperature gradient and laser pulse length. While Spaepen and Turnball [26] reported that the recrystalline velocity is governed by the undercooling of the melt. The higher the undercooling, the greater the velocity. Moreover, tracing the interface motion can be achieved by observing the impurities position after the interface has advanced. As a matter of fact, pulsed laser annealing is a unique technique for surface processing in which dopants could be associated onto lattice sites at concentration far in excess of solid solubilities (White, Appleton, and Wilson) [27]. When a material is pulsed laser annealed, the interface velocity is very high and a high impurity trapping is expected. However, these trapping events are velocity and orientation dependent and a near equilibrium crystal growth can be achieved. The constitutional supercooling at specific velocities and impurities concentration, makes the interface unsteady resulting in the incorporation of dopants into cellular arrays. Thus remarkable microstructures can be obtained by means of surface laser irradiation.

3.7 Magnetic Properties of CdMnTe

3.7.1 The Paramagnetic Phase

In magnetic materials, the orientation of the magnetic moments are responsible for the magnetic effects of these materials. Two magnetic moments exist, namely the electron spin dipole moment and the electron orbital dipole moment.

The magnetic susceptibility per unit volume is defined by:

$$\chi = \frac{\mu_0 M}{B} \tag{3.25}$$

where M is the magnetisation of the material, and B is the applied magnetic field.
If a negative susceptibility in the material is sustained, this is referred as diamagnetic while a material with a positive susceptibility is called paramagnetic. The existence of the Mn ions in diluted magnetic semiconductors gives rise to the magnetisation M of the material. Before discussing the magnetisation of DMS materials, it is very useful to give a brief study of the magnetisation of isolated Mn ions. The magnetic moment of a single Mn ion can be expressed as:

$$\mu = -g \mu_B \frac{S}{\hbar} \tag{3.26}$$

where $\mu_B = e\hbar/2m$ is the Bohr magneton, g = 2 is the Lande factor, and M_J = -5/2,....., 5/2, for the ground state. The total magnetisation of a system of non-interacting paramagnetic ions in the dilute limit ($x < 0.01$), can be given by:

$$M = -x N_0 g \mu_B \langle S_z \rangle = x N_0 g \mu_B S B_s(y) \tag{3.27}$$

where N_0 is the number of cations per unit volume, S=5/2 for Mn ions, $\langle S_z \rangle$ is the thermal average spin per Mn site (or the mean spin density), x is the Mn concentration, and $B_s(y)$ is the Brillouin function defined as [28]:

$$B_s(y) = \frac{(2S+1)}{2S}\coth\frac{(2S+1)y}{2S} - \frac{1}{2S}\coth\frac{y}{2S}\,;\ where\ \ y = \frac{g\mu_B SB}{kT} \tag{3.28}$$

We can realize from equations (3.27) and (3.28) that the magnetisation is highly dependent on the temperature and the applied field. In case of low field and high-temperature limit (i.e., $g\mu_B SB/kT \ll 1$), there is a linear relation between M and B and the susceptibility is represented by the Curie's law:

$$\chi = \frac{C}{T} \tag{3.29}$$

where C is the Curie constant equal:

$$C = xN_0\mu_0(g\mu_B)^2 S(S+1)/3k \tag{3.30}$$

In the case of interacting paramagnetic ions, a critical temperature exist, below which, in the absence of external magnetic field, an internal exchange interaction aligns the spins. This is explained in terms of the Heisenberg spin exchange hamiltonian which is given by:

$$H_{ex} = -\sum_{R_i} J_{NN}(r - R_i) S_i \cdot S_j \tag{3.31}$$

where J_{NN} is the nearest neighbour paramagnetic ion exchange integral, and S_i and S_j are the spin operators for the spin momenta of ions i and j. In DMS, this kind of interaction is known as superexchange interaction in which the anion between the Mn ions takes part.

In a system of Mn ions, an antiferromagnetic interaction between the spins occur. This was observed from the negative sign of the exchange integral which indicates an antiparallel spin alignment. Furthermore, in an antiferromagnet, the temperature dependence of the susceptibility and the specific heat capacity have a cusp at a critical temperature known as the Neel temperature T_N. At temperatures higher than T_N the susceptibility displays a Curie-Weiss behaviour [29] which is given by:

$$\chi = \frac{C}{T + T_{\Theta}} \tag{3.32}$$

where C is already defined in equation 4.30 and T_{Θ} is the Curie-Weiss temperature. In fact, the above expression can be used for DMS at high temperatures and approximate values of χ can be found. For higher values of x at low temperature, departure from the Curie-Weiss law is noticed. However, no quantitative analysis has been made of this behaviour. For DMS of arbitrary values of x the magnetisation M cannot be expressed by the standard Brillouin function because of the Mn-Mn interactions. Nevertheless, a qualitative similarity between the observed M vs B behaviour and the Brillouin function still exists. According to this similarity, Gaj, Planel, and Fishman [30] put forward an empirical but very beneficial expression given by:

$$M = -xN_0 g\mu_B \langle S_z \rangle = xN_0 g\mu_B S_0 B_s \left(\frac{g\mu_B SB}{k(T + T_0)}\right) \tag{3.33}$$

where T_0 and S_0 are phenomenological fitting parameters defined as the effective temperature and the effective spin respectively. Both T_0 and S_0 are functions of x and are related to the antiferromanetic interactions between the Mn ions. As a matter of fact, the above expression can be applied satisfactory for the observed magnetisation of DMS alloys but it is purely a phenomenological model.

The profile of the M vs B curve is determined by the effective temperature T_0. While the correct magnitude of M is attained from the effective spin S_0. Figure. 3.2 shows the effective temperature T_0 and effective spin S_0 variations with the Mn concentration x for $Cd_{1-x}Mn_xTe$ [30], as determined from optical data.

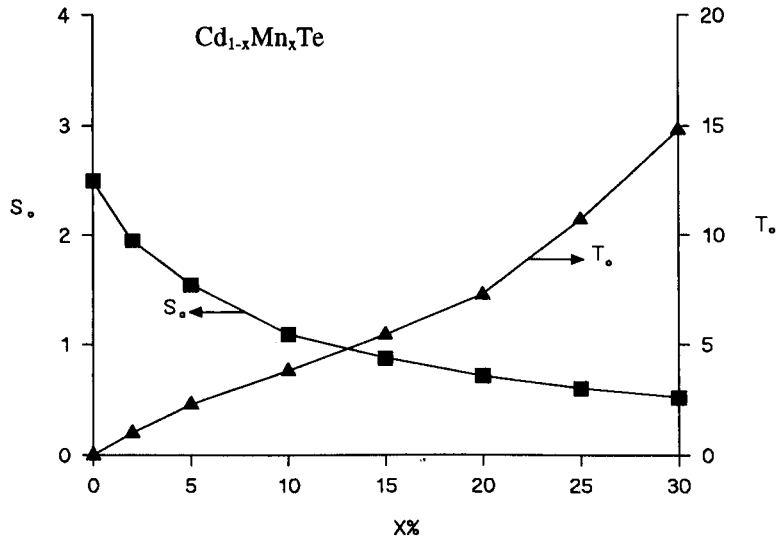

Figure 3.2: The effective temperature T_0 and effective spin S_0 variation with Mn concentration x for $Cd_{1-x}Mn_xTe$, Gaj et al [30].

A qualitative interpretation of the magnetisation expression given in 3.33 shows that a fraction of Mn ions are unable to respond to an external field due to the spin-pairing effects with a neighbouring ion. As a result of this, a fraction of Mn ions do not contribute to the magnetisation of the system. Consequently, only a reduced set of Mn ions (x_{eff}) contribute to the magnetisation, in which each of these Mn ions contributes its maximum spin S=5/2. According to this, xS_0 in equation 3.33 is better represented by:

$$xS_0 = x_{eff} S \tag{3.34}$$

where x_{eff} is the effective Mn concentration in which Mn ions remain unpaired. At very high fields (B>10 Tesla) even the empirical expression (3.33) is no longer valid and the behaviour of M vs B shows a steplike function [31,32]. This is a direct indication of the existence of antiferromagnetically coupled nearest neighbour pairs, and can be readily justified as follows. The energy level for a pair of Mn ions in the magnetic field is given by:

$$E_T = -J_{NN}[S_T(S_T+1) - \frac{35}{2}] + g\mu_B m_T B \tag{3.35}$$

where J_{NN} is the nearest-neighbour Mn-Mn exchange integral; the parameter S_T is the total spin for a pair, which can have integral values from 0 to 5; and m_T has values of S_T, S_T-1,....., -S_T. For J_{NN} >0, the ground state is nonmagnetic at zero field, with S_T=0, and it remains the ground state as long as $g\mu_B B|J_{NN}|^{-1} < 2$. While this condition holds, pairs do not contribute to the total magnetisation. However, once the value of $g\mu_B B|J_{NN}|^{-1}$ exceeds 2, the energy for S_T=-1 becomes the ground state and suddenly a contribution to the magnetisation from all the pairs occur. This results in a step in the magnetisation. Other such steps are similarly predicted for higher fields and the magnetic fields at which this steps take place consequently provide a straight measure of J_{NN}:

$$J_{NN} = -g\mu_B \frac{B_2 - B_1}{2} \tag{3.36}$$

where B_1 and B_2 are two adjacent crossing fields.

3.7.2 The Spin-Glass Phase

DMS alloys can be categorised into another type of magnetic material which is known as the spin-glass phase. Due to the existence of short-range spin ordering, the temperature dependence of the susceptibility (but not of the specific heat capacity) has a cusp at a characteristic temperature. This is the main difference from an antiferromagnet. Figure 3.3 shows the magnetic phase diagram for CdMnTe [33]. The figure illustrated below indicates that CdMnTe material is paramagnetic above a critical temperature defined as T_g. The low-temperature phase is discernibly disordered and exhibits many of the features of the spin-glass state. Especially, the low-temperature specific heat has a linear temperature dependence and, at least in samples with x<0.65,

does not reveal any peculiarity at T_g. The spin-glass behaviour in DMS has regularly been attributed to frustration of the antiferromagnetic interactions between the Mn ions, arising from the lattice topology of the $II_{1-x}Mn_xVI$ alloys. This is establish by theoretical arguments which indicate that, for a dilute magnetic *fcc* lattice with nearest-neighbour interactions only, a spin-glass state becomes possible when the magnetic ion concentration exceeds a percolation threshold above $x \cong 0.19$ [34]. Furthermore, neutron scattering experiments showed small antiferromagnetically ordered clusters already exist above T_g and become larger with decreasing temperature. When the characteristic temperature T_g is attained, then the neighbouring clusters become sufficiently large that they touch. As the large clusters interlock, their ability to orientate becomes frozen and they no more respond to an external field. Nevertheless, when the Mn concentration is decreased the spin ordering effects are restrained to lower temperature as figure 3.3 reveals, where T_g decreases with decreasing x.

3.7.3 The Exchange Interaction in $II_{1-x}Mn_xVI$ Alloys

The exchange interaction in DMS occurs as a result the interaction between the *s* and *p* band electrons and the $3d^5$ electrons associated with the Mn ions. It is because of this *sp-d* exchange that magneto-optical and high field magneto-transport properties of DMS are, indeed, different from those observed in their nonmagnetic counterparts. This kind of exchange interaction essentially occurs in the paramagnetic phase.

When a semiconductor in question contains localized magnetic moments, the exchange interaction of these moments (i.e., the $3d^5$ electrons of Mn ions) with *sp* band electrons will modify the band structure of the semiconductors. The hamiltonian of this interaction is given by [33]:

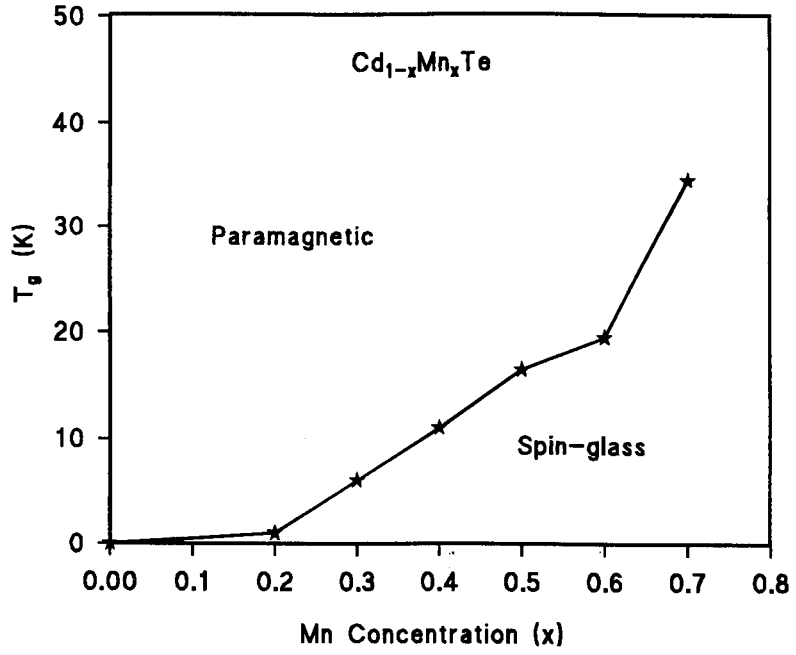

Figure 3.3: Magnetic phase diagram for $Cd_{1-x}Mn_xTe$, Furdyna [33].

$$H_{ex} = -\sum_{R_i} J^{sp-d}(r - R_i)S_i \cdot \sigma \tag{3.37}$$

The summation is only over the lattice sites occupied by the Mn ions, where r and R_i are the coordinates of the conduction band electron and the Mn ion respectively, J^{sp-d} is the electron-ion sp-d exchange coupling constant, and σ and S_i are the spin operators for the band electrons and the Mn ion respectively. Adding the H_{ex} term to the original hamiltonian H_0 will give the total hamiltonian of the system:

$$H_{total} = H_0 + H_{ex} \tag{3.38}$$

For a non-magnetic semiconductor the Landau levels and the Zeeman (spin) splittings of the band electrons are represented by the same original hamiltonian H_0. To simplify the term H_{ex} two convenient approximations are carried out. First, since the electronic wavefunction is very extended, the electron "sees" a large number of Mn ions at any time. Therefore we can use the molecular field approximation, where we replace S_i by the thermal average $\langle S_z \rangle$ of all Mn ions in the direction of the applied field, which is related to the magnetisation of the system [see equation (3.33)]. Second, and also because the electronic wavefunction spreads over a large number of lattice sites, J^{sp-d} can be replaced by $xJ^{sp-d}(r-R)$, where R denotes to the position of every cation site. With these approximations, the exchange hamiltonian can be written as:

$$H_{ex} = -\sigma\langle S_z \rangle x \sum_R J^{sp-d}(r - R) \tag{3.39}$$

The summation is carried out over all cation sites R.

It is quite obvious from the above equation that the exchange contribution is essentially related to the operator σ_z and it is therefore expected to have an important effect on the characteristics which involve the spin state of the electron. By considering an ideal parabolic Γ_6 conduction band, the energies of the two spin substates of the lth Landau level are expressed as:

$$E_l(\uparrow) = E_g + (l + \frac{1}{2})\hbar\omega_c + \frac{1}{2}\left(g^*\mu_B B - N_0\alpha x\langle S_z \rangle\right) \tag{3.40}$$

$$E_l(\downarrow) = E_g + (l + \frac{1}{2})\hbar\omega_c - \frac{1}{2}\left(g^*\mu_B B - N_0\alpha x\langle S_z \rangle\right) \tag{3.41}$$

where E_g is the energy gap, $\omega_c = \frac{eB}{m^*}$ is the cyclotron frequency, g^* is the band g factor (i.e., that obtained by solving H_0), and α is the exchange integral for the s-like Γ_6 electrons which is given by:

$$\alpha = \frac{\langle S|J^{sp-d}|S\rangle}{\Omega_0} \tag{3.42}$$

where Ω_0 is the volume of an unit cell.

The Landau ladder term $(l+\frac{1}{2})\hbar\omega_c$ and the term $\pm\frac{1}{2}g^*\mu_B B$ originate from H_0 and are only present when B is nonzero. The term $\pm\frac{1}{2}N_0\alpha x\langle S_z\rangle$ arises from the exchange hamitonian H_{ex}. The energy expression can be rewritten in the form of:

$$E_\pm = E_g + (l+\frac{1}{2})\hbar\omega_c \pm \frac{1}{2}g_{eff}\mu_B B \tag{3.43}$$

where the upper and lower signs correspond to the $\uparrow$ and $\downarrow$ spin states, accordingly, and the g_{eff} is an effective g factor, expressed as:

$$g_{eff} = g^* - \frac{N_0\alpha x\langle S_z\rangle}{\mu_B B} \tag{3.44}$$

The case in a DMS alloy is thus essentially as in a non-magnetic parent, but with the spin splitting expressed by a modified g factor which is related to the lattice temperature, composition, and magnetic field.

In wide-gap $II_{1-x}Mn_xTe$, the magnetic splitting related to H_{ex} is much larger than the Landau and/or spin splitting predicted by ordinary *sp* band theory. This results from the much larger effective masses m^* in wide-gap materials and the "*sp* band" g factors (g^*), which are of the order of unity. In the parabolic example, mentioned previously, the terms containing $\hbar\omega_c$ and g^* can be neglected in equations (3.40) and (3.41). Therefore, the splitting of the levels is dominated by only the exchange term H_{ex}, at least at low and moderate fields. The splitting of the Γ_6 conduction band with field can be written as:

$$\Delta E_c = -xN_0\alpha\langle S_z\rangle m_j; \quad m_j = \pm\frac{1}{2} \tag{3.45}$$

Similarly, the splitting of the Γ_8 valence band in a magnetic field is given by:

$$\Delta E_v = -\frac{1}{3}xN_0\beta\langle S_z\rangle m_j; \quad m_j = \pm\frac{1}{2},\pm\frac{3}{2} \tag{3.46}$$

where β is the exchange integral for p-like electrons in the Γ_8 band, expressed as:

$$\beta = \frac{\langle X|J^{sp-d}|X\rangle}{\Omega_0} \tag{3.47}$$

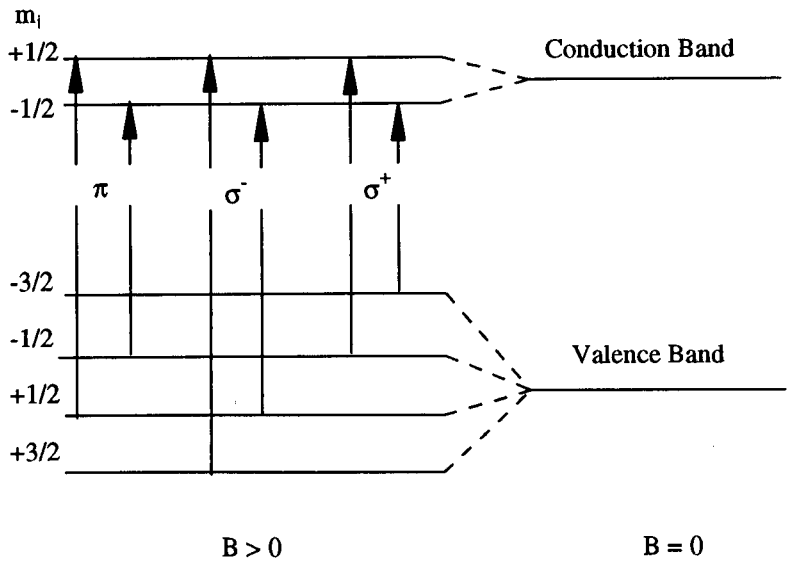

Figure 3.4: A schematic diagram of the exchange splitting for the Γ_6 conduction band and Γ_8 valence band. The diagram also shows the optical allowed transitions (arrows) for the two circular polarisation (σ^+ and σ^-) and the linear polarisation (π).

Figure 3.4 shows the spin splitting of the conduction band (Γ_6, two fold splitting) and the valence band (Γ_8, four fold splitting) at nonzero field for a wide-gap II-Mn-VI alloy. The diagram displays as well the electric-dipole allowed transitions for the two circular polarisations rotating transverse to the applied field (which, when observed in the Faraday geometry, are referred to as σ^+ and σ^- transitions), and for linear polarisation observed parallel to the field (which is seen in the ordinary Voigt geometry, defined as π transition).

In low temperature magneto-optical measurements, the splitting of these levels can be observed through the free exciton transitions with the polarisation of the emission either $\sigma^{\pm}(\Delta m_j = \pm 1)$ or π $(\Delta m_j = 0)$. Recalling equation (3.45) and (3.46), the energy difference between the σ^+ and σ^- exciton transitions for the heavy hole exciton $(\Delta m_j = \pm 3/2)$ is given by [28]:

$$\Delta E_{fx}(HH) = -xN_0(\alpha - \beta)\langle S_z \rangle \tag{3.48}$$

In a similar way, the energy difference between the σ^+ and σ^- exciton transitions for the light hole exciton $(\Delta m_j = \pm 1/2)$ is expressed as:

$$\Delta E_{fx}(LH) = xN_0(\alpha + \frac{1}{3}\beta)\langle S_z \rangle \tag{3.49}$$

In fact, the parameters $N_0\alpha$ and $N_0\beta$ can be determined by evaluating the energy splitting of the heavy hole exciton and the light hole exciton separately. Values of these two parameters have been measured for CdMnTe where, it is found that

$N_0\alpha = 0.22\,eV$ and $N_0\beta = -0.88\,eV$. Thus the ratios of the HH to LH splittings are almost 15 to 1.

3.7.4 Examples of the *sp-d* Exchange Interaction Effects in DMS

In semiconductors containing magnetic ions there is generally a sizeable exchange interaction between the spins of conduction electrons (or valence band holes) and the local moments of the magnetic ions. This interaction, the sp-d exchange interaction, is responsible for various novel spin-dependent effects.

3.7.4.1 The Giant Exchange Splitting of the Free Exciton

The most important and convenient observation of the *sp-d* exchange interaction in wide-gap DMS is the exchange splitting of the free exciton transitions [35]. What is unique about the free exciton exchange splitting is the very large size of the field that would be required to achieve the same splitting as for the normal Zeeman splitting at saturation, which would require, in a nonmagnetic semiconductor, fields of the order of a 100 T. Furthermore, due to the large size of the splitting and the simplicity of measuring sharp exciton lines, the parameters α and β and information of the magnetisation M could readily be determined.

3.7.4.2 The Giant Faraday Rotation

Another fascinating example of the *sp-d* exchange interaction effect is the giant Faraday rotation. Due to the large exchange splitting of the absorption edge in wide gap DMS, this results in a sizeable large difference in dispersion (i.e., large difference in the index of refraction) of the two circular polarisations of light, $\sigma^{\pm}$, in the Faraday geometry. This dispersion generates the exceedingly large Faraday rotation with values of the order of 10^6 mT at liquid helium temperatures [36]. In fact Faraday rotation in a DMS has regularly been used as an excellent tool to map various aspects of magnetisation, both static and dynamic [37].

3.7.4.3 The Magnetic Polaron Effect

Another remarkable phenomenon resulting from the *sp-d* exchange interaction is the bound magnetic polaron (BMP), which is observed at zero magnetic field. When an electron is bound to a donor then the electron orbit (which is described by the hydrogenlike orbit model) encloses a large number of Mn ions. Consequently, the electron interacts with the Mn ions through the sp-d exchange. This interaction polarizes the Mn spins, leading to a finite magnetisation on the donor orbit scale. Furthermore, the spontaneous fluctuations of magnetisation results in a finite magnetic moment on the same local scale. As a result of both contributions the bound electron perceives a finite magnetisation, and energy is then needed to flip the spin of the donor electron even at zero magnetic field. This can lead to a reduction of the total energy of the system. Such a complex is known as magnetic polaron (MP). The photon energy of a recombining polaron complex is given by:

$$h\nu = E_g - E_{ex} - E_{mp} \tag{3.50}$$

where E_{mp} is the magnetic polaron energy.

When free excitons are bound to impurities or alloy fluctuations, the exciton polarizes the Mn spins within its volume creating a local ferromagnetic order. This ordering leads to a reduction of the exciton energy. This is known as a bound exciton magnetic polaron. Theoretical calculations of impurity-bound magnetic polarons (resulting from charge carriers bound to donor or acceptor ion sites) in DMS have been performed [38]. The magnetic field, temperature, and concentration of the magnetic ions dependence on the polaron energy were evaluated. Optical experiments have given the most convincing evidence for the existence of bound magnetic polarons in semimagnetics [39] where it has been shown in CdMnTe structures that at $x > 0.1$ the broadening of photoluminescence lines and the Stoke's shifts occur as a result of the formation of magnetic polarons [40], from which the corresponding values of the polarons energies were determined.

3.8 Experimental Results

3.8.1 Sample Structure

The CdTe/$Cd_{1-x}Mn_xTe$ MQW used in the present work was grown by MBE on a (001) InSb substrate. Its structure consisted of a 0.1 μm CdTe buffer layer, a 1.5 μm thick $Cd_{1-x}Mn_xTe$ barrier layer and a stack of 18 QWs with 75 Å quantum wells and 150 Å barriers. The buffer layer was grown with a lower Mn concentration than the barrier layers in order to achieve better lattice matching to the QW stack. Different sections, cleaved from the sample, were annealed at different fluences with a Lumonics TE-860-4 XeCl laser, emitting 32 ns pulses at 308 nm, in argon gas at one atmosphere pressure in order to provide an inert atmosphere to limit ablation effects. The laser fluences used were 50, 60, 70, 80, 90, 100. 130, 150, and 180 mJ cm^{-2}. PL and PLE measurements were carried out in magnetic field with an Oxford Instruments superconducting magnet cryostat capable of providing magnetic fields up to 13.5 Tesla. The sample was mounted strain-free in the cryostat at 2K, see chapter 2. Optical access to the sample was performed in the Faraday configuration. The excitation source was a Pyridine-2 or DCM dye laser, pumped with an Argon ion laser at 514 nm. Double Crystal X-Ray Diffraction measurements were used to obtain information about the sample structure, the manganese ion concentration and the lattice relaxation of the epitaxial layers.

3.8.2 DCXRD Measurements

Double Crystal X-Ray Diffraction (DCXRD) spectra of the structure prior to and after annealing are shown in figure 3.5, where they are compared to a simulated spectrum of the control sample (curve a), calculated using the Dynamical Theory of X-ray Diffraction, see chapter 2. Weaker satellite peaks from the QWs are seen at either side of the stronger substrate and buffer layer peaks. The line widths of the satellite peaks are broad when compared to their calculated values, pointing to a fairly non

uniform value of the well width L_z in the present sample. Little change was observed to the DCXRD spectrum when annealing at low fluence up to 50 mJ cm^{-2}. However

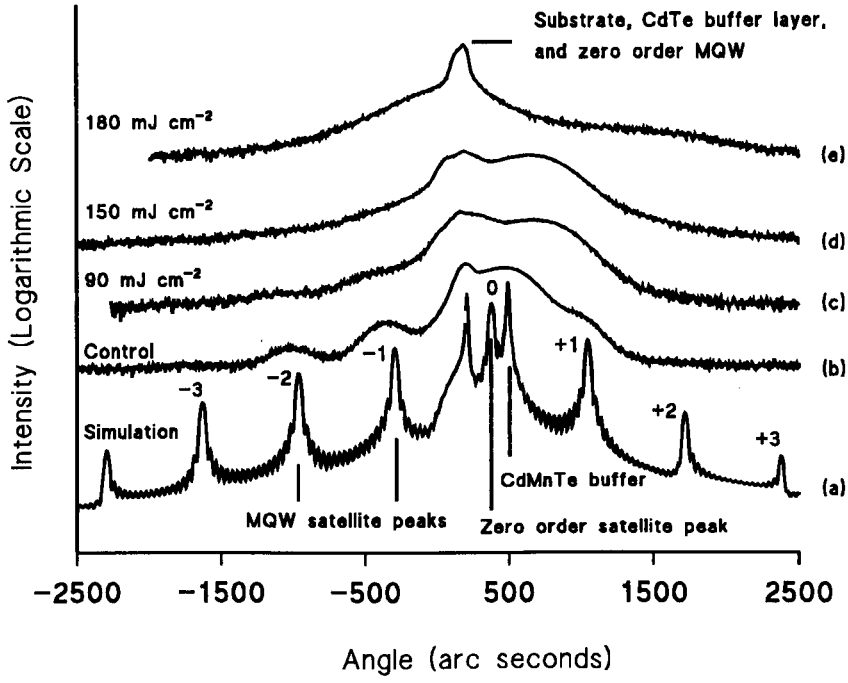

Figure 3.5: DCXRD of the unannealed control sample, b, and the pulsed laser annealed samples, c, d and e, of the CdTe/CdMnTe MQWs used in the present work. The spectra are compared with the simulation (a), calculated using the Dynamical Theory of X-ray Diffraction.

thereafter a progressive weakening of the satellite MQWs peaks takes place with increasing fluence up to 150 mJ cm^{-2} , at which point the satellite peaks have completely vanished; only the substrate peak and a broadened CdMnTe buffer layer peak remain, spectrum (d). At 180 mJ cm^{-2}, the CdMnTe buffer layer peak has also disappeared and only the substrate peak and a weak broad peak around 1500 arcsec can be observed, spectrum (e). Spectrum (a) shows the simulated rocking curve of the control sample. Assuming the Mn concentration in the barriers of the QWs to be 0.15 (as determined from the PLE, see below), the best fit to the spectrum of the control sample was found with a well width of 75 Å and a barrier thickness of 190 Å. The Mn concentration of the thick CdMnTe buffer was found to be 0.128 with the layer fully relaxed (as determined from the PL, see below).

3.8.3 Photoluminescence

The PL spectra of some of the MQW structures before and after annealing with different laser energy fluences are shown in figure 3.6. Prior to annealing, emissions are only observed around 1.62 eV and 1.784 eV. The strongest emission is assigned to an exciton bounded at a neutral donor D^0X [41]. Other weaker emissions on the high

energy tail probably result from D^0X emissions in regions of the structure with narrower quantum wells. No essential change in the PL spectrum is seen in samples annealed up to 60 mJ cm^{-2}. However at a fluence of 70 mJ cm^{-2}, emission A disappears and emission B appears at 1.815 eV. A further emission also appears just above D^0X, emission E. Also shown in figure 3.6 is the PLE of the control sample recorded while monitoring the D^0X emission. Both emission A and a peak at 1.841 eV are observed in the PLE spectrum of the D^0X emission. From the concentration dependence of the CdMnTe band-gap of Twardowski et al [42], which is given by

$$E_{fx}(4.2K) = 1.595 + 1.587x \quad (eV), \tag{3.51}$$

the concentration of Mn in the barrier layers is found to be 0.15. Emissions A and B correspond to emissions from excitons trapped at alloy fluctuations in CdMnTe, commonly called the L2 emission. From the energy dependence of the L2 emission [43] which is given by:

$$E_{L2}(4.2K) = 1.6047 + 1.397x \quad (eV) \tag{3.52}$$

emission B corresponds to a Mn concentration of 0.15 whilst that of emission A corresponds to that of 0.12, which agrees with the DCXRD results. Thus emission B is identified with excitons trapped in the barrier layers whilst emission A may be identified with excitons trapped in the buffer layer which was grown with a lower Mn concentration.

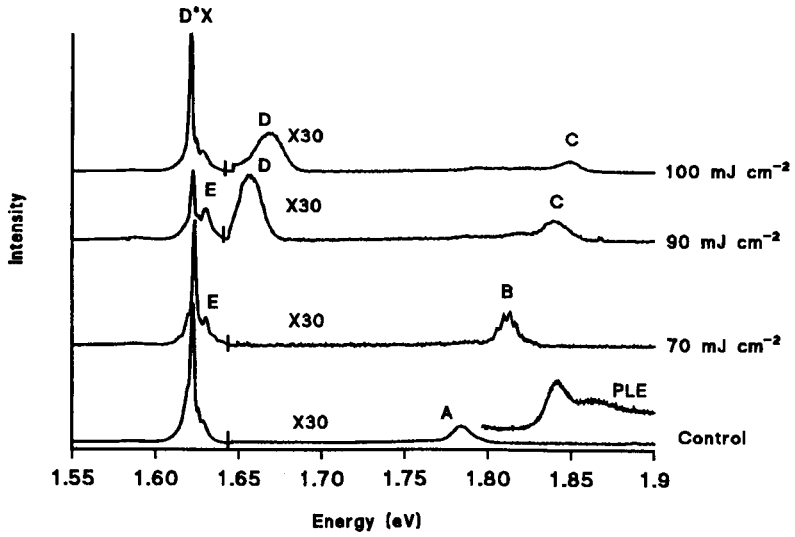

Figure 3.6: Photoluminescence spectra of the CdMnTe/CdTe MQW sample before and after annealing at different laser energy fluences.

At 80 mJ cm^{-2} no further change occurs to the spectrum but when the laser fluence is increased to 90 mJ cm^{-2}, emission B virtually disappears to be replaced by emission C at 1.840 eV and emission D at 1.655 eV. Some strengthening of emissions in the vicinity

of E is also seen. At 100 mJ cm^{-2} emissions C and D move to higher energies, whilst at higher fluences, progressive weakening of the entire spectrum takes place with some variation in the energies of emissions C and D. Generally this variation is no more than seen in figure 3.6, but the overall nature of the spectrum remains the same except for progressively weakening . Above 150 mJ cm^{-2} no emission is observed. There was no significant non-uniformity across the sample.

3.8.4 Photoluminescence in a Magnetic Field

PL measurements of the MQW structures were performed when a magnetic field is applied. Shifts of the various emissions at different magnetic fields were observed. Figure 3.7 shows the PL spectra of the control sample at 2K and various magnetic fields. The intensity of the D^0X line drops with increasing fields and the free exciton line becomes dominant. This decline of the D^0X transition is caused as a result of the antiparallel nature of the D^0X electron spins [44]. The energy shift of emission (A) at 1.79 eV (emission from the thick CdMnTe buffer layer) into lower energies is quite large, owing to the presence of the manganese in the thick CdMnTe layer. Moreover, emission A narrows when increasing the magnetic field. The energy shift of emission (A) vs magnet field is presented in figure 3.8. Equations (3.45) and (3.46) were used to calculate the energy shift of emission A at various magnetic fields. These calculations were carried out at different Mn ion concentrations and the fit between the experimental data and the calculated one is presented in figure 3.8. A value of 12.5% for the Mn ion concentration is obtained.

The PL spectra of the 70 mJ cm^{-2} annealed sample at various magnetic fields can be seen in Figure 3.9. Emission from the barrier layers B at 1.815 eV is shifted into lower energies when increasing magnetic field. Again, emission B narrows and gets

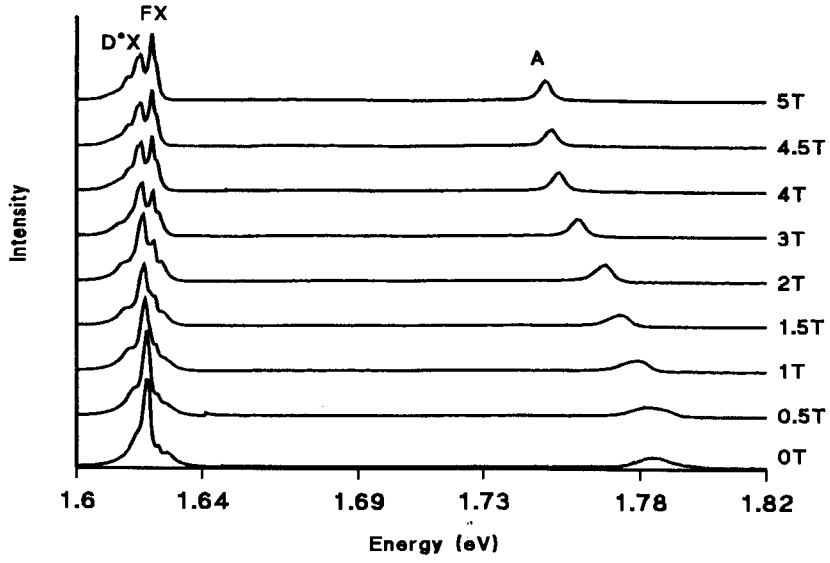

Figure 3.7: PL spectra of the control sample at 2 K and at various magnetic fields, A is the emission from the thick CdMnTe buffer layer.

sharper when increasing the magnetic field. Also the FX emission increases and the D^0X emission decreases when increasing the magnetic field. In a similar way, using equations (3.45) and (3.46), the corresponding Mn ion concentration is found to be 14.5%, as illustrated in figure 3.10.

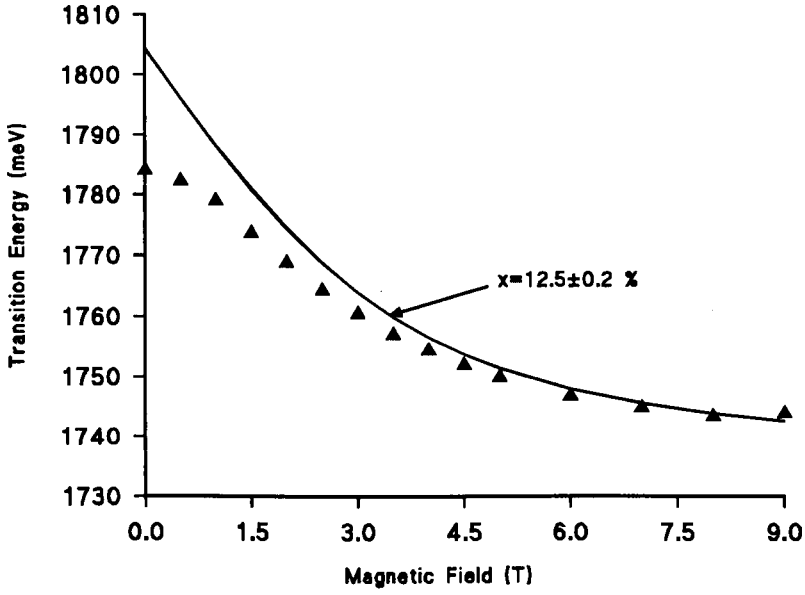

Figure 3.8: Measured energy shift of the e1hh1 (σ^+ component) of emission (A) vs magnetic field of the control sample (solid triangles) and calculated values (solid line) using equations (3.45) and (3.46).

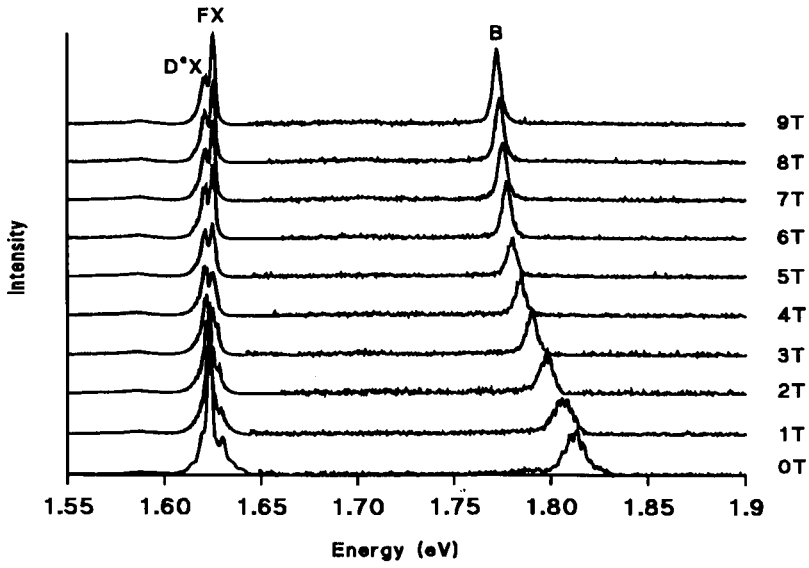

Figure 3.9: PL spectra of the 70 mJ cm^{-2} annealed sample at 2 K and various magnetic fields.

Figure 3.11 shows the PL spectra of the 90 mJ cm^{-2} annealed sample at different magnetic fields. Prominent red shifts of emissions (D) and (C) are observed with increasing magnetic field. A value of 16.5% was found for the Mn ion concentration, from equations (3.45) and (3.46), figure 3.12. Again an increase of the FX emission and narrowing of emission C are observed when increasing the magnetic field.

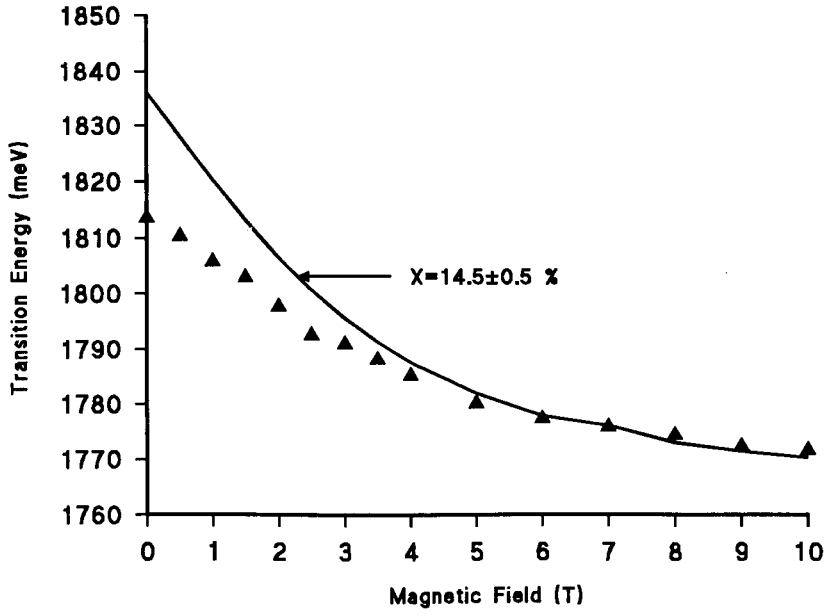

Figure 3.10: Measured energy shift of the e1hh1 (σ^+ component) of the barrier emission B (see figure 4.8) vs magnetic field of the 70 mJ cm^{-2} annealed sample (solid triangles) and calculated values (solid line) using equations (3.45) and (3.46).

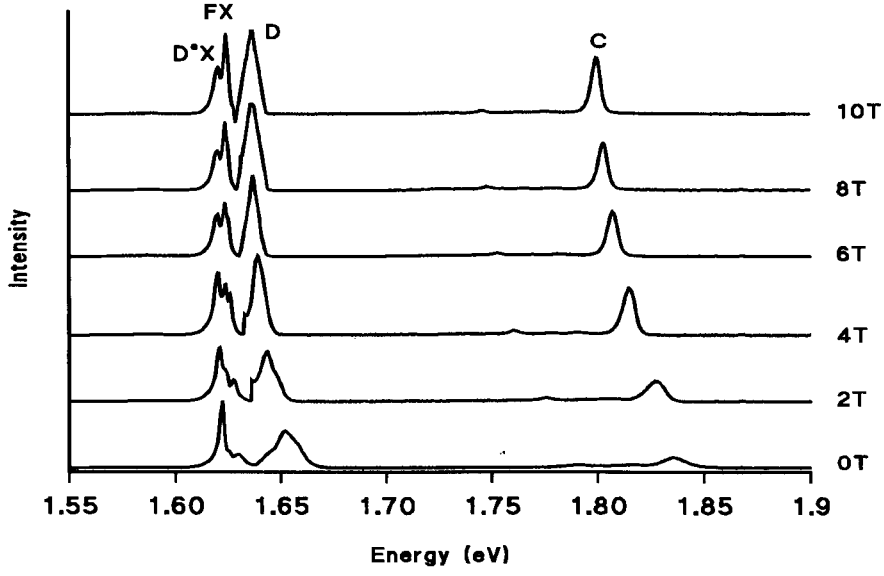

Figure 3.11: PL spectra of the 90 mJ cm^{-2} annealed sample at various magnetic fields.

The energy shifts of the various transitions vs magnetic field of the 100 mJ cm^{-2} annealed sample are shown in Figure 3.13. The corresponding Mn ion concentration was estimated as 17.2%, Figure 3.14. Also an increase of the FX emission and narrowing of emission C are observed when increasing the magnetic field.

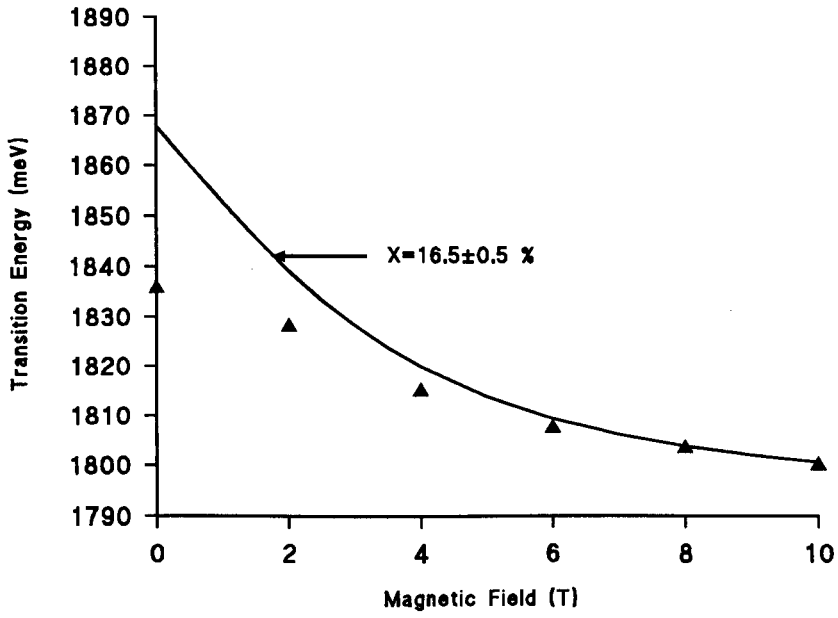

Figure 3.12: Measured energy shift of the e1hh1 (σ^+ component) of the barrier vs magnetic field for the 90 mJ cm^{-2} annealed sample (solid triangles) and calculated values (solid line) using equations (3.45) and (3.46).

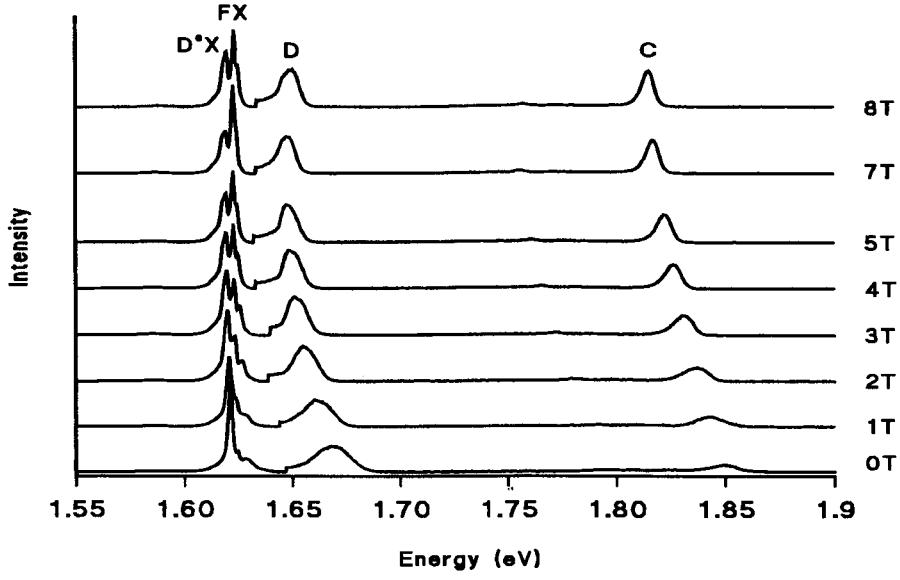

Figure 3.13: PL spectra of the 100 mJ cm^{-2} annealed sample at various magnetic fields.

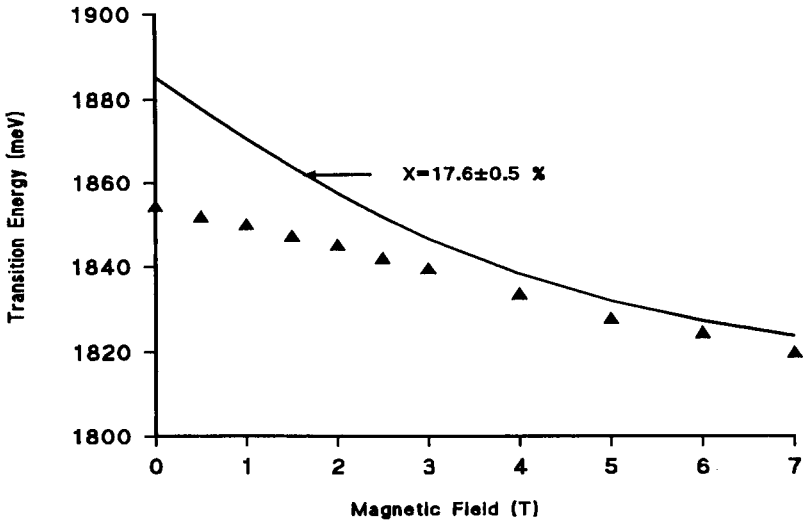

Figure 3.14: Measured energy shift of the e1hh1 (σ^+ component) of the barrier vs magnetic field for the 100 mJ cm^{-2} annealed sample (solid triangles) and calculated values (solid line) using equations (3.45) and (3.46).

There are some common features to the four PL figures, 3.7, 3.9, 3.11, and 3.13; the barrier (or CdMnTe buffer for the control sample) peaks narrow and are accompanied with an intensity increase when increasing the magnetic field. Also the FX emission increases whilst the D^0X emission decreases with increasing magnetic field. Broadening of the exciton emissions from the barrier or buffer layers observed in the different samples arises principally from random alloy compositional fluctuations which modulate the bandgap. A further contribution to the line broadening can also arise from the formation of magnetic polarons. This can occur when excitons are localised either at impurities or at the alloy fluctuations themselves. The linewidth reduction of emissions A, B, C, and D in an applied magnetic field can be clarified in the following way. For a given alloy fluctuation, the associated potential well decreases in magnitude in the presence of a magnetic field. This in turn will lead to more extended exciton orbits and hence reduced values for the polaron energies [45]. Furthermore, when large magnetic field is applied, extensive polarisation of the Mn ions occur, hence formation of magnetic polarons becomes more difficult. When the magnetization is saturated magnetic polaron effects are absent. These two effects taken together will lead to smaller polaron energies and hence narrower exciton line widths when the magnetic field is applied [46].

3.8.5 PLE Measurements

3.8.5.1 PLE at Zero Magnetic Field

In order to explore more fully the behaviour of PLA the PLE spectra of the control sample and the 90 mJ cm^{-2} annealed sample were recorded. These PLE spectra are shown in figure 3.15.

The PLE spectrum of the control sample (a) was recorded while monitoring the D^0X emission at 1.620 eV. From calculations of the energies of the various transitions (see figure 3.18 below) the lines at 1.626 eV and at 1.647 eV can be identified as the e1hh1 and e1lh1 free exciton transitions. The broad peaks at higher energies at 1.730 eV and 1.780 eV are identified as the e2hh2 and e2lh2 exciton transitions.

For the 90 mJ cm^{-2} annealed sample spectrum (b) was recorded while monitoring the D^0X emission whilst spectra (c) and (d) were recorded whilst monitoring emissions E and D respectively (see figure 3.6). For (b), figure 3.15, the e1hh1 and e1lh1 transitions are close to those observed from the control sample but with slightly higher energies, at 1.629 and 1.651 eV respectively, whilst the e2hh2 and e2lh2 exciton transitions are observed at energies of 1.737 eV and 1.782 eV. In spectrum (c), the e1hh1 and e1lh1 transitions are again blue shifted and observed at energies of 1.634 eV and 1.655 eV respectively. Furthermore, the transitions related to the e2hh2 and e2lh2 excitons are seen at energies of 1.74 eV and 1.792 eV respectively. The PLE spectrum observed whilst monitoring emission D at 1.653 eV shows further blue shifts with lines at 1.666 eV and at 1.685 eV. These are again assigned to the e1hh1 and the e1lh1 exciton transitions, while the peaks at 1.780 eV and at 1.805 eV are assigned to the e2hh2 and e2lh2 exciton transitions respectively. Generally the larger the blue shift is, the broader the transitions. In (a), (b) and (c), figure 3.15, the broad peak at 1.685 eV is unknown, but certainly does not fit e1hh2 or e2hh1 transitions.

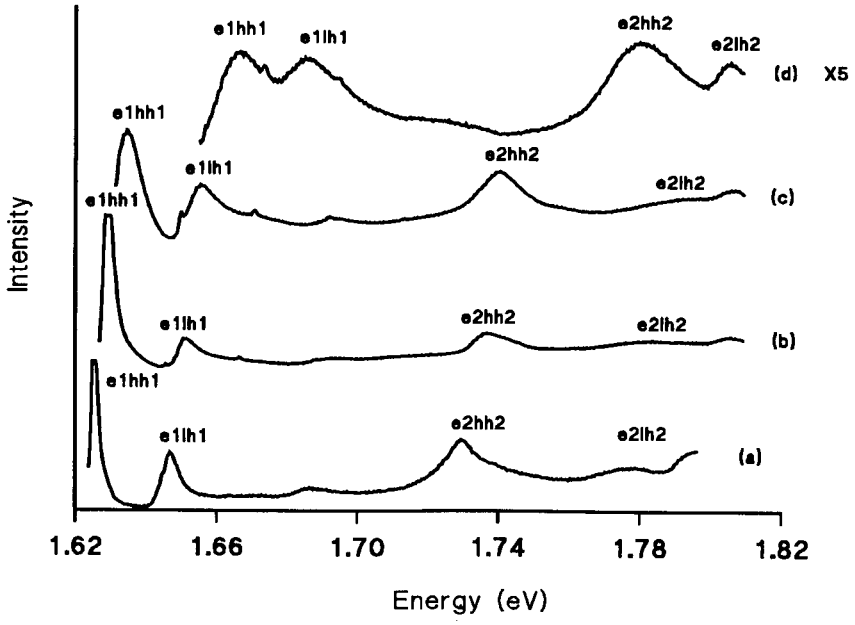

Figure 3.15: Photoluminescence excitation spectra of control sample (a), 90 mJ cm^{-2} annealed sample (b) [while monitoring the D^0X emission], 90 mJ cm^{-2} annealed sample (c) [while monitoring emission (E) at 1.653 eV] and 90 mJ cm^{-2} annealed sample (d) [while monitoring emission (D) at 1.653 eV] at zero magnetic field.

3.8.5.2 PLE in Magnetic Field

In a magnetic field each of the lines of figure 3.15 splits into two components. Figures 3.16 and 3.17 show the PLE spectra of the control sample while monitoring the D^0X emission at various magnetic fields for the σ^+ and σ^- components respectively.

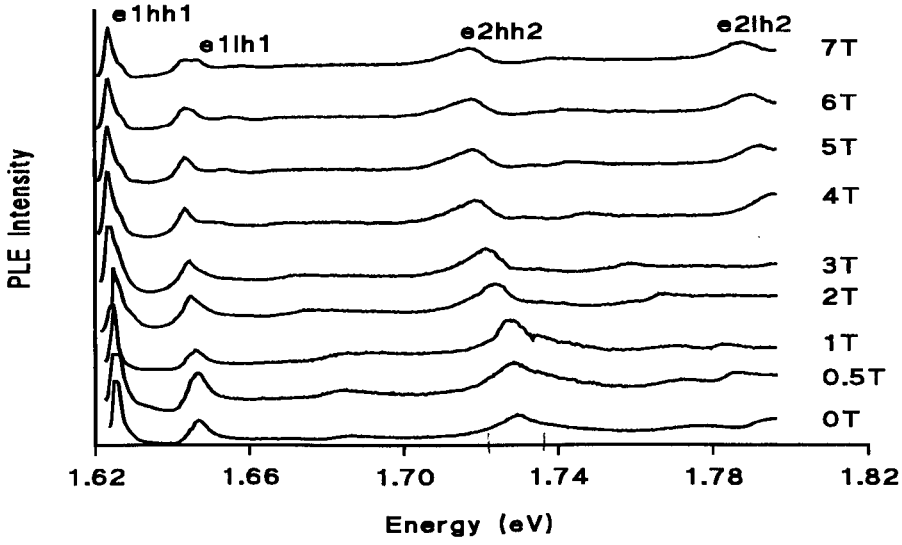

Figure 3.16: Photoluminescence excitation spectra of the control sample while monitoring the D^0X emission at 1.621 eV for σ^+ component at various magnetic fields.

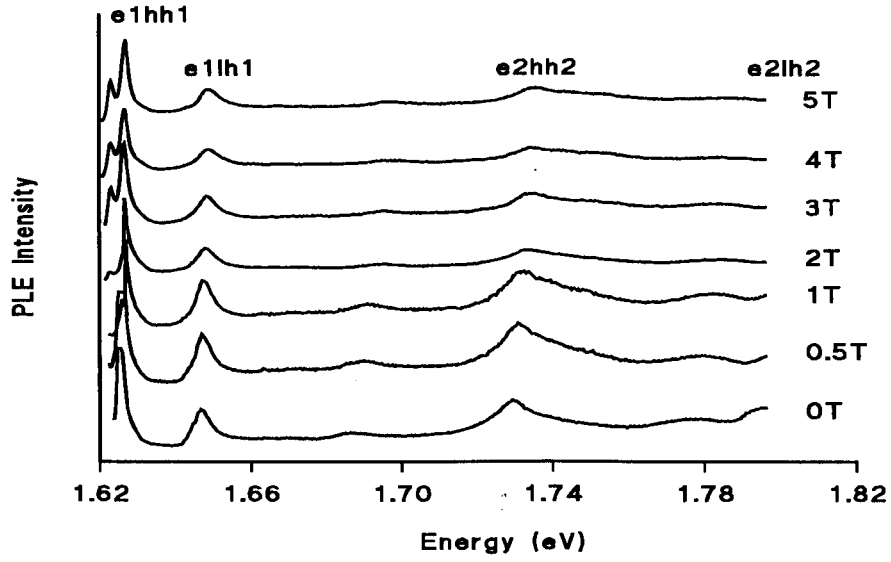

Figure 3.17: Photoluminescence excitation spectra of the control sample while monitoring the D^0X emission at 1.621 eV for σ^- component at various magnetic fields.

The fan diagram for the control sample, taken from figures 3.16 and 3.17, is shown in figure 3.18. The splitting between the σ^+ and σ^- components is quite small, typically 3 and 15 meV for the e1 and e2 components respectively at 4T.

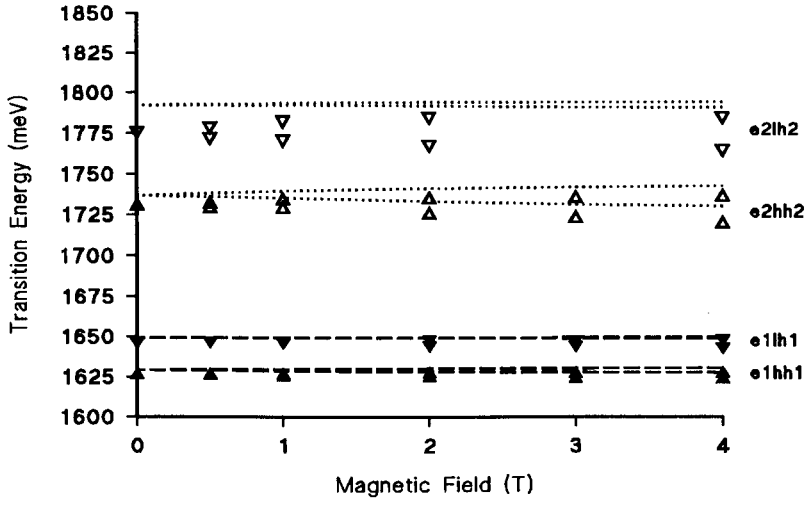

Figure 3.18: Measured exchange splittings of the different excitonic transitions of the control sample and the calculated values of these transitions assuming a valence band offset of 40% [47, 48].

The PLE spectra of the 90 mJ cm^{-2} annealed sample while monitoring the D^0X emission at various magnetic fields for the two polarised components $\sigma^{\pm}$ are shown in figures 3.19, and 3.20. The corresponding fan diagram, taken from figure 3.19 and 3.20

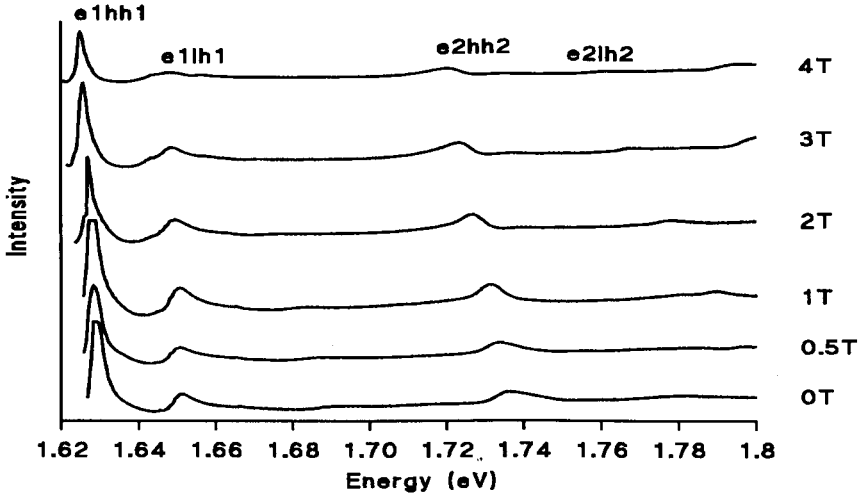

Figure 3.19: Photoluminescence excitation spectra of the 90 mJ cm^{-2} annealed sample while monitoring the D^0X emission at 1.624 eV for σ^+ component at various magnetic fields.

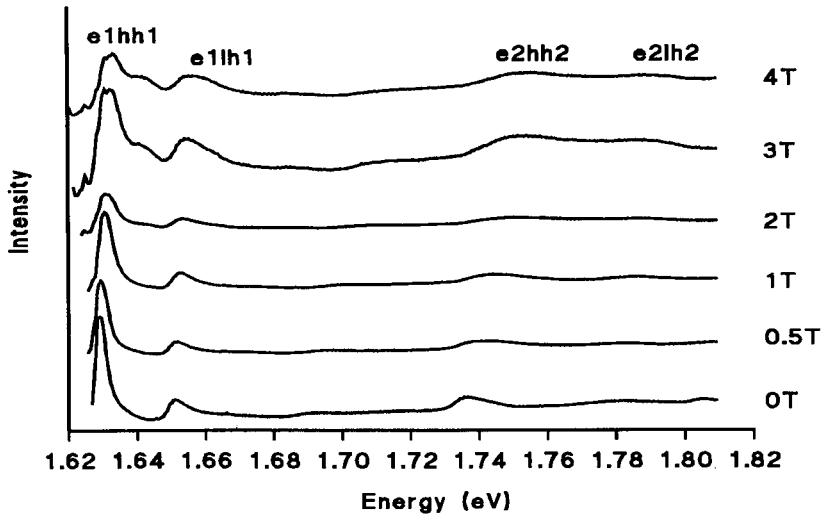

Figure 3.20: Photoluminescence excitation spectra of the 90 mJ cm^{-2} annealed sample while monitoring the D^0X emission at 1.624 eV for σ^- component at various magnetic fields.

with the different excitonic transitions (i.e. e1hh1, e1lh1, e2hh2, and e2lh2 transitions) for both polarisation components $\sigma^{\pm}$ is shown in figure 3.21. The splittings between the $\sigma^{\pm}$ components is quite small for the e1hh1, typically 7.6 meV at 4T, while the splitting of the e2hh2 is quite large, 33 meV at 4T.

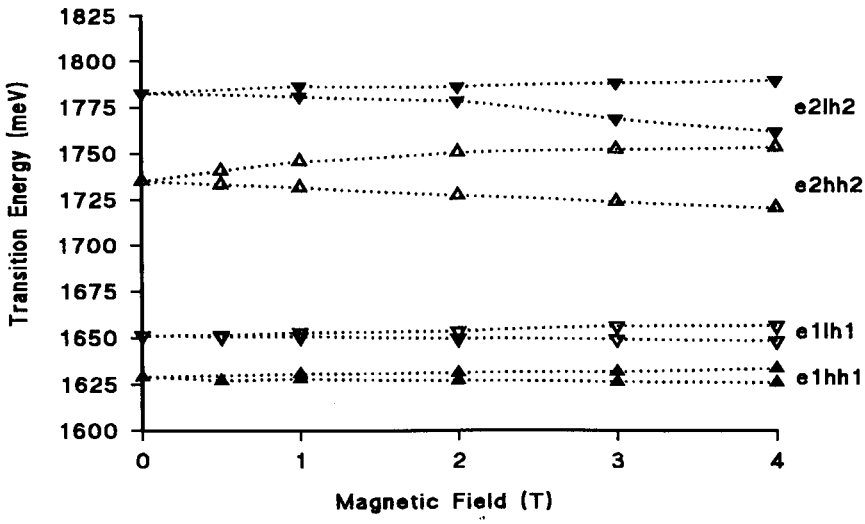

Figure 3.21: The fan diagram with the various transitions of the 90 mJ cm^{-2} annealed sample while monitoring the D^0X emission at 1.624 eV for σ^- (higher energy) and σ^+ (lower energy) components at various magnetic fields. Dotted lines are a guide for the eye.

The PLE spectra of the 90 mJ cm^{-2} annealed sample while monitoring emission E at 1.629 eV at various magnetic fields for the two polarised components $\sigma^{\pm}$ are shown in figures 3.22, and 3.23

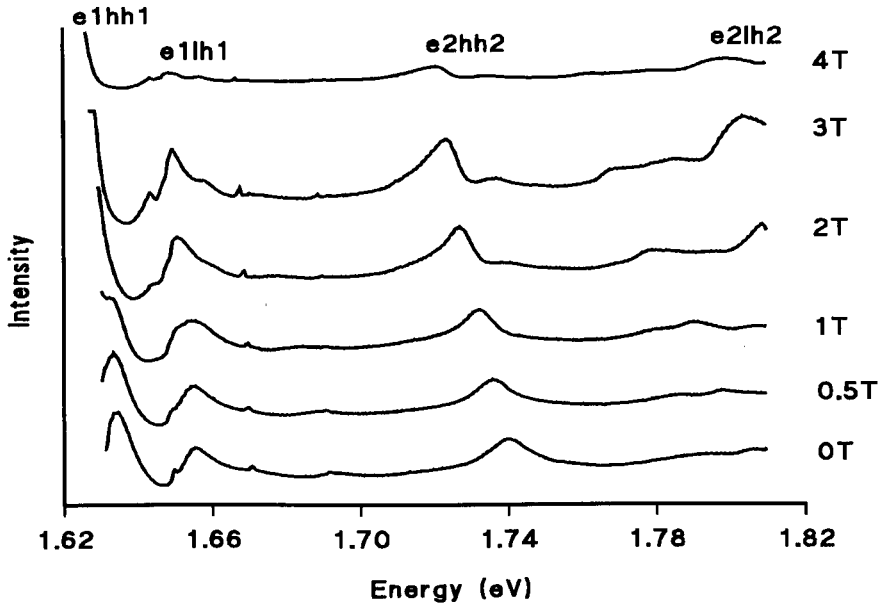

Figure 3.22: Photoluminescence excitation spectra of the 90 mJ cm^{-2} annealed sample while monitoring emission (E) at 1.629 eV for σ^{+} component at various magnetic fields.

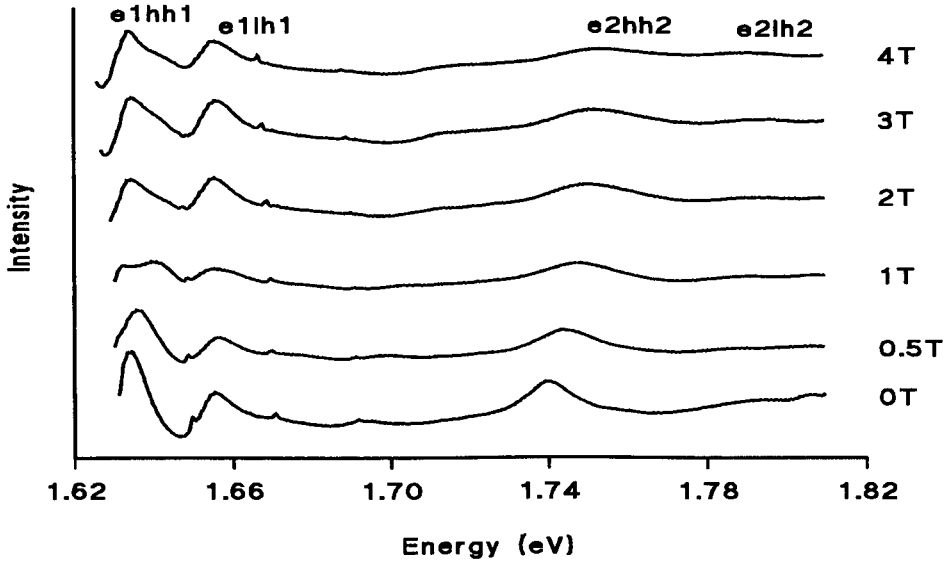

Figure 3.23: Photoluminescence excitation spectra of the 90 mJ cm^{-2} annealed sample while monitoring emission (E) at 1.629 eV for σ^{-} component at various magnetic fields.

The fan diagram of the 90 mJ cm^{-2} annealed sample while monitoring emission E at 1.629 meV, taken from figures 3.22 and 3.23, for $\sigma^{\pm}$ polarisation components at various magnetic fields is shown in figure 3.24. The splittings between the $\sigma^{\pm}$ components of the e1hh1 is quite smaller than that observed for the e2hh2, typically 8 meV and 33 meV for the e1hh1 and e2hh2 components respectively at 4T.

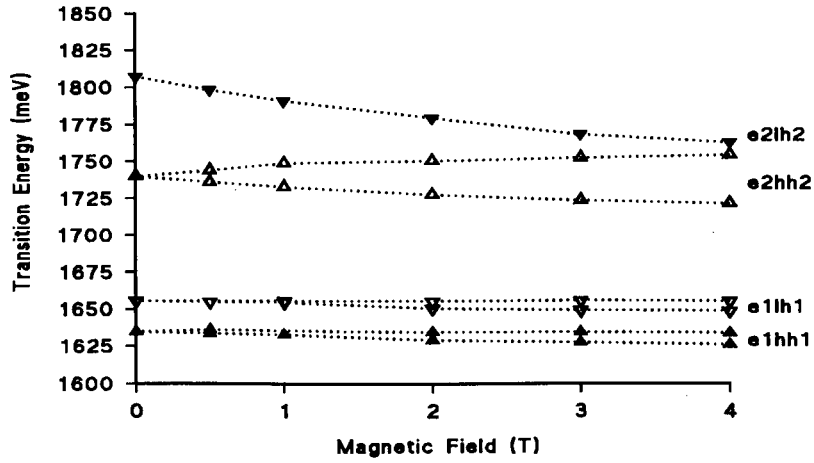

Figure 3.24: The fan diagram with the various transitions of the 90 mJ cm^{-2} annealed sample while monitoring emission (E) at 1.629 eV for σ^{-} (higher energy) and σ^{+} (lower energy) components at various magnetic fields. Dotted lines are a guide for the eye.

Figures 3.25, and 3.26 show the PLE spectra of the 90 mJ cm^{-2} annealed sample while monitoring emission D at 1.653 eV at deferent magnetic fields for the two polarised components $\sigma^{\pm}$.

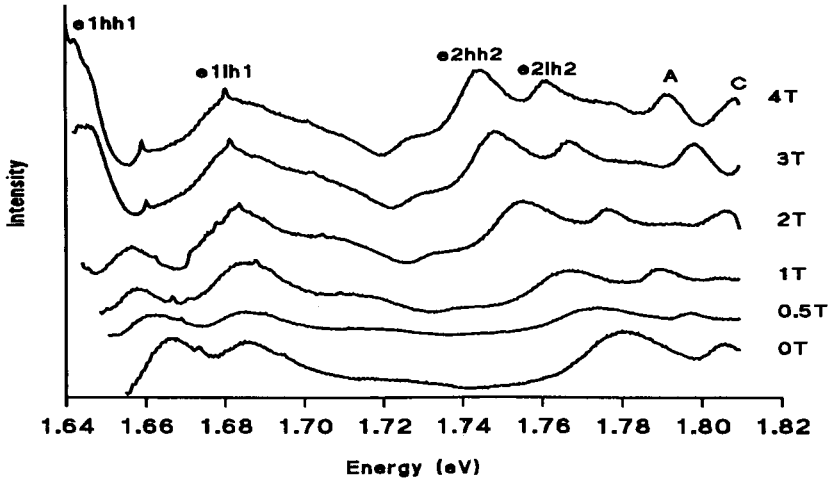

Figure 3.25: Photoluminescence excitation spectra of the 90 mJ cm^{-2} annealed sample while monitoring emission (D) at 1.653 eV for σ^{+} component at various magnetic fields.

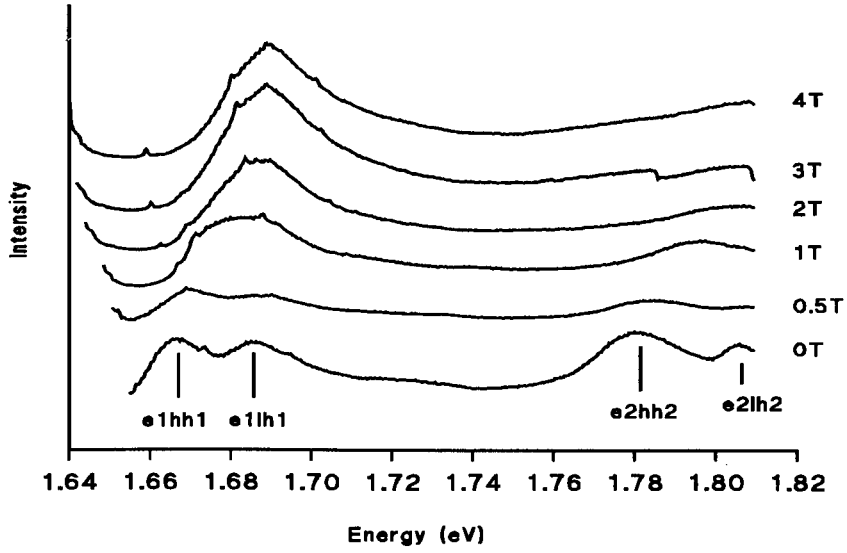

Figure 3.26: Photoluminescence excitation spectra of the 90 mJ cm^{-2} annealed sample while monitoring emission (D) at 1.653 eV for σ^- component at various magnetic fields.

The fan diagram of the 90 mJ cm^{-2} annealed sample while monitoring emission D at 1.653 meV, taken from figures 3.25 and 3.26, for $\sigma^{\pm}$ polarisation components at various magnetic fields is shown in figure 3.27. The splittings between the $\sigma^{\pm}$ components is quite large, typically 46.3 meV and 61.8 meV for the e1hh1 and e2hh2 components respectively at 4T.

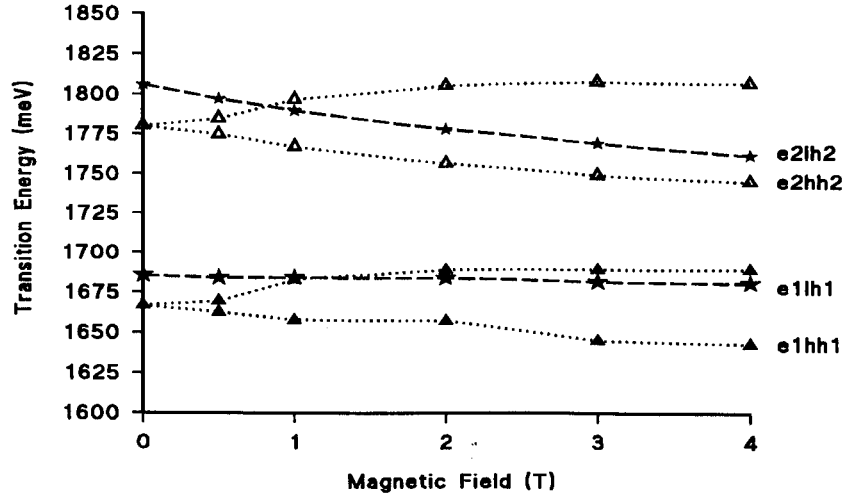

Figure 3.27: The fan diagram with the various transitions of the 90 mJ cm^{-2} annealed sample while monitoring emission (D) at 1.653 eV for σ^- (higher energy) and σ^+ (lower energy) components at various magnetic fields. Dotted lines are a guide for the eye.

In figure 3.28 the energies of the two components of the e1hh1 transitions when monitoring emissions D, E and D^0X are compared with those of the control sample. The splitting between the two components for the e1hh1 transition increases as the energy of the zero field transition increases; whilst monitoring emission D the splitting is typically 46 meV at 4T, whilst it is typically 9 meV when monitoring emission E and 3 meV when monitoring the $D^0(X)$ emission of either the control sample or the annealed samples. The splittings of the e2 transitions likewise increase in the annealed sample.

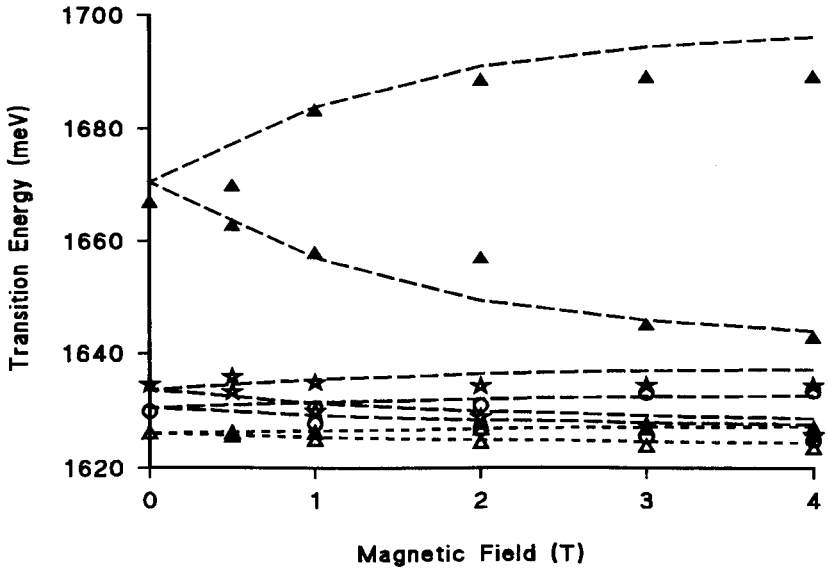

Figure 3.28: Exchange splittings of the e1hh1 transitions recorded in figure 3.15. The four sets of data recorded whilst monitoring emissions D (solid triangle), E (star), the $D^0(X)$ emission of the 90 mJ cm^{-2} annealed sample (circle), and the D^0X emission of the control sample (open triangle). The calculated splittings are shown by the broken lines, assuming differing amounts of Mn diffusion into the QW and a valence band offset of 40%.

3.9 Discussion

3.9.1 Diffusion Measurements and a Theoretical Model of Pulsed Laser Annealing of the MQW Structure

The experimental data can be explained using a simple model of laser heating for a two layer system [21] in which a homogeneous layer of CdTe 2005 nm thick is placed on an InSb substrate. A homogeneous layer is used because there are no reliable thermal constants for CdMnTe in the literature and furthermore no analytical solutions capable of dealing with a multiple quantum well stack. The principal simplifying assumptions of the model are that the heat is absorbed at the surface, which is nearly correct for material with a high absorption coefficient at the laser wavelength, that the thermal properties do not vary with temperature, which is certainly not the case, and

that the irradiance, or optical power density, is constant over the duration of the laser pulse, which again is not true. Nevertheless, in spite of these assumptions, the model can satisfactory account for the PLA processes in CdTe, as shown below.

Equations (3.16) and (3.17) can be used to find the temperature-time history at any depth within the material, as shown in figure 3.29 for an incident fluence of 75 mJ cm^{-2} and a pulse duration of 26 ns. It is noticeable that close to the surface the temperature rise is recorded as being close to 1200 °C, but this is an over estimate, as the model takes no account of phase changes and the thermal properties associated with them, for example the latent heat of fusion or changes in density and thermal conductivity of the molten layer, etc. The calculation assumes that CdTe is still solid at this temperature, and therefore the temperatures above the melting point of 1090 °C strictly have no physical meaning. Furthermore, it is a feature of analytical solutions such as this that surface temperatures are overestimated slightly. A numerical solution of the heat diffusion equation performed under identical assumptions shows that the temperature profiles flatten off toward the surface [49], whereas the profiles predicted by equations (3.16) and (3.17) continue to rise toward the surface.

The effect of the temperature changes in figure 3.29 on the quantum well structure can be understood in terms of the diffusion of Mn ions from the barriers into the QWs at the elevated temperatures. This modifies the potential profile of the QWs and causes the excitonic energies to increase. At the same time the magnetic effects become more pronounced. The amount of diffusion is strongly dependent on the laser fluence owing to the strong temperature dependence of the atomic diffusion coefficients. Their values at different temperatures are shown on the right of figure 3.29. They have been determined by interpolation from known values at 500 and 800 °C [50,51]. Assuming an exponential dependence of diffusion on temperature, the diffusion coefficient D(T) can be described by the empirical relation ,

$$D(T) = \exp(0.031T - 46.9) \times 10^{16} \ , \qquad (3.53)$$

in units of $Å^2\ s^{-1}$ where T is in Kelvin. The extent of the Mn diffusion into the QW is then determined by the integrated value of D(T)t, where t is the time the material is at a temperature T. Values of D(T)t vary greatly with depth, as shown in figure 3.30 [25].

The most significant change that occurs in the PL spectrum is at a laser fluence of 90 mJ cm^{-2} and above. The normal melting point of CdTe is 1090 °C and from the temperature rises shown in figure 3.30 it seem reasonable to ascribe the threshold fluence to the point at which melting just starts at the surface. At fluences above this threshold more of the material melts and the melt depth increases. Both the PL and DCXRD data indicate little annealing below about 50 mJ cm^{-2}. However above this fluence some annealing of the MQW stack occurs, as seen principally in the weakening of the satellite peaks in the DCXRD spectrum, figure 3.5. In the optical spectra, PLA at 70 and 80 mJ cm^{-2} causes emission B to appear, figure 3.6, which , from the energy of the PLE spectrum shown for the control sample is attributed to the recombination of carriers in the barrier layers. On the other hand emission A is associated with the buffer layer; its energy is equivalent to a Mn concentration of 0.12, in agreement with that found from the DCXRD analysis. From the PLE spectrum the x value for the barrier layers is 15.0%. We expect that the laser induced damage at the top of the stack reduces the carrier mobility, so increasing the probability of recombination in the barrier

layers and also reducing the number of carriers reaching the buffer layer, so that emission A is no longer observed following PLA.

The most significant change in the PL spectrum shown in figure 3.6 occurs at 90 mJ cm^{-2} where emission D appears, which is believed to arise from a quantum well into which Mn has diffused from the adjacent barrier layers. All wells in this stack are nominally identical so it is not immediately apparent which well (or wells) has given rise to this emission. However, the temporal history of the temperature can be used to calculate the total diffusion during the laser heating and afterward, and it is apparent from figure 3.30 that the greatest diffusion occurs from the well just below the molten material, whilst wells within the melt depth can expect to homogenize completely. Thus emission D is attributed to emission from the first quantum well beneath the melt front (see below) and emission E, figure 3.6, and blue shifts of the PLE peaks seen in figure 3.15 are attributed to deeper quantum wells with less diffusion. At higher laser fluences the surface melts to a greater depth and the melt front advances into the QW structure, whilst the energy of emission D remains about the same. (In other samples the difference in the energy at different fluences is in fact much less than seen in figure 3.6). The emission now originates from a deeper QW, again just beneath the melt front and again heavily diffused. Above the threshold emission C also appears with an energy above that of the barrier emission, B. Emission C must therefore correspond to emission from a region of the structure with a greater Mn ion concentration than that of the barriers. From its energy the peak is associated with a Mn concentration of 18%. It is possible that the cause of the increased concentration is the partial segregation of the Mn ions in the melted region during recrystalization. The observation of this emission, C, provides a further indication that the observed threshold corresponds to the start of lattice melting.

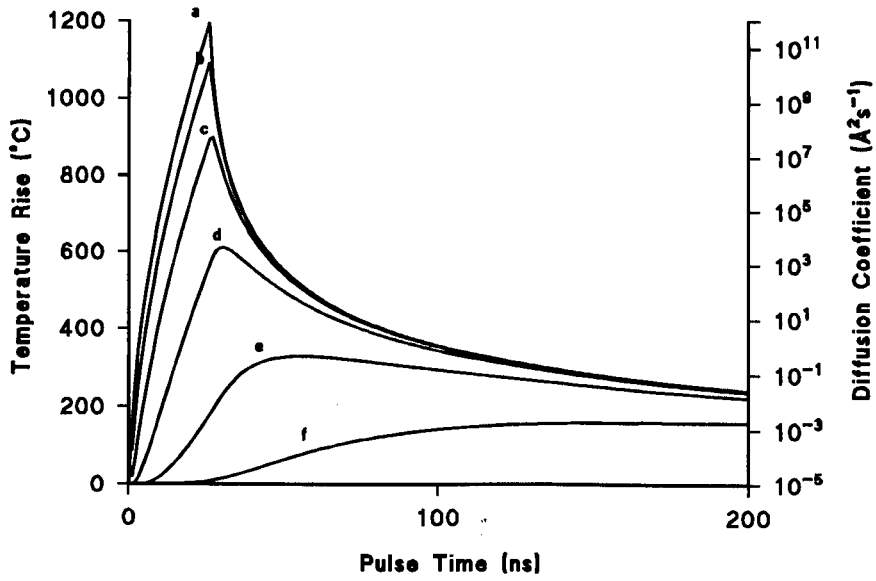

Figure 3.29: Temperature- Time- Diffusion Coefficient curves calculated at different depths from the surface for a laser fluence of 75 mJ cm^{-2}. Curves (a) to (f) represent the temperature rise at depths of 35.5, 72, 145.5, 295, 596, and 1207 nm respectively.

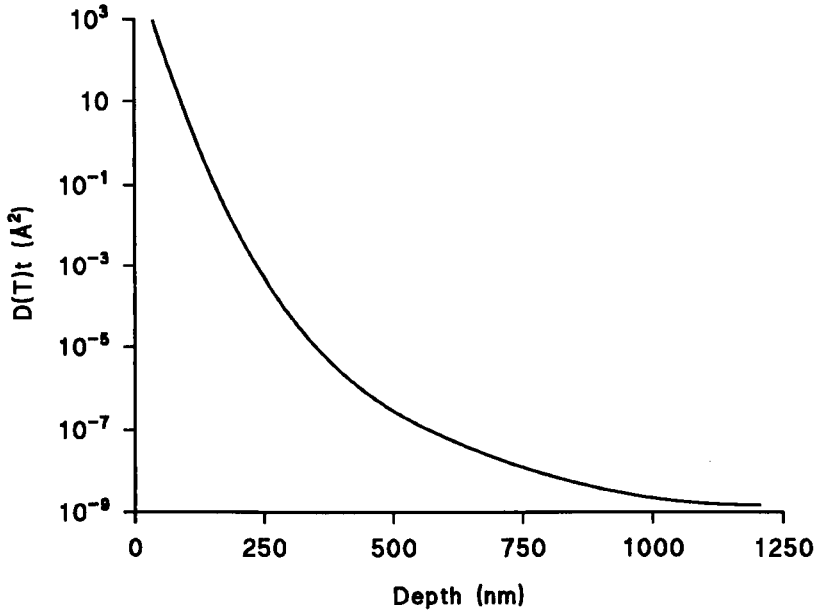

Figure 3.30: Calculated D(T)t values at different depths from the surface and a pulse laser fluence of 75 mJ cm^{-2}.

In order to provide further confirmation for the validity of the model, exciton energies have been calculated in diffused QWs, that are characterised by their values of D(T)t. The potential profile of the QWs and their corresponding e1hh1 exciton energies are shown in figure 3.31. The diffusion profiles of the QW were calculated [25] by solving the second Fick diffusion equation (3.20) and representing the diffusion profile by an error function with a diffusion length $l_d = 2[D(T)t]^{1/2}$, see section 3.5. The e1hh1 exciton energies have been calculated in the diffused QWs by a self consistent method [52] starting from the one dimensional electron and hole wavefunctions in the diffused QW. These initial wavefunctions were determined by solving the 1-dimensional Schrodinger equation for the diffused potential with the shooting technique. Before diffusion the well is assumed to have abrupt interfaces with a Mn barrier concentration of 0.15 and with well and barrier thicknesses 75 Å and 190 Å respectively (section 3.8.2). Figure 3.31 shows that for values of D(T)t above about 50 Å^2 the exciton energy starts to increase significantly. Values of D(T)t for the QWs that give rise to emissions D, E and the D^0X of the 90 mJ cm^{-2} annealed sample are found from the energy differences of the e1hh1 peaks observed in PLE for these emissions, figure 3.15(d), 3.15(c), and 3.15(b) with the same peak for the control sample, figure 3.15(a). From these energies and figure 3.31 values of D(T)t are 300 Å^2, 30 Å^2 and 10 Å^2 respectively. Table 3.1 shows the corresponding D(T)t values of the e1hh1 transition for the control sample and 90 mJ cm^{-2} annealed sample (while monitoring emissions D^0X, E, and D) along with their transition energies taken from figure 3.15 (and shown at zero magnetic field in figure 3.28). It is quite clear that the e1hh1 transition is increasingly blue shifted by diffusion, which itself can be quantified by the values of D(t)T given in table 3.1.

e1hh1 Transition	Control Sample	(D^0X Emission) Annealed Sample	(Emission E) Annealed Sample	(Emission D) Annealed Sample
Transition Energy (eV)	1.621	1.629	1.634	1.667
D(T)t ($Å^2$)	0	10	30	300

Table 3.1: The e1hh1 transition energy with the corresponding D(T)t values for the control sample and the 90 mJ cm^{-2} annealed sample (for D^0X, E, and D emissions), taken from figure 3.28.

Further confirmation that the blue shift of the emissions D and E arise as a result of Mn diffusion into the QW (and not a different process, such as the generation of point defects) comes from the magnetic field dependence of the exciton transitions shown in figures 3.18 and 3.28. This dependence confirms the values of D(T)t for the various transitions presented in table 3.1. The splitting of the electron and heavy hole band edges in a magnetic field can be expressed as:

$$\Delta E_e = -x N_0 \alpha \langle S_z \rangle m_j \; ; \quad m_j = \pm\frac{1}{2}. \tag{3.54}$$

$$\Delta E_{hh} = -\frac{1}{3} x N_0 \beta \langle S_z \rangle m_j \; ; \quad m_j = \pm\frac{3}{2} \tag{3.55}$$

Since the energy shifts in equations (3.54) and (3.55) are non-linear in Mn concentration owing to the non-linear way S_0 changes with x, see figure 3.1, the shape of the diffused potential well profiles shown in figure 3.31 change when a magnetic field is applied. However by applying equations (3.54) and (3.55) to each point across the potential profiles shown in figure 3.31 and recalculating the exciton energy in the modified potential well, the effect of the magnetic field on the PLE spectrum to be calculated. For example, at 4 T the energies of the $\sigma^{\pm}$ components of the e1hh1 exciton line are shown in figure 3.31 as a function of the amount of diffusion. In figure 3.28 the values of D(T)t previously found for the D, E and D^0X emissions (for the 90 mJ cm^{-2} annealed sample) from the zero field blue shifts of 300 $Å^2$, 30 $Å^2$ and 10 $Å^2$, table 3.1, are used to fit the splitting of the $\sigma^{\pm}$ components. The fit is remarkably good and provides excellent confirmation that the QWs responsible for both emissions are linked to the diffusion of Mn atoms following PLA, with considerably more diffusion in the QW associated with emission D. Among other things, the overall fit of the optical data to the theory justifies choosing an error function for the diffused potential profile.

The values of D(T)t determined from the magneto-optical data are now compared to those predicted from the simple theory of PLA described in section 3.4.2. The melting point of CdTe is 1090 ^{0}C; figure 3.30 predicts that for a laser fluence of 75 mJ cm^{-2} this point would occur 25 nm from the surface i.e. about one QW period. It is of course impossible to say just where the melt front would be with respect to the position of the QWs, but if the front were just above the QW at a temperature of about 1090 ^{0}C then D(T)t is predicted to be 10^3 $Å^2$, if the QW were one period below the

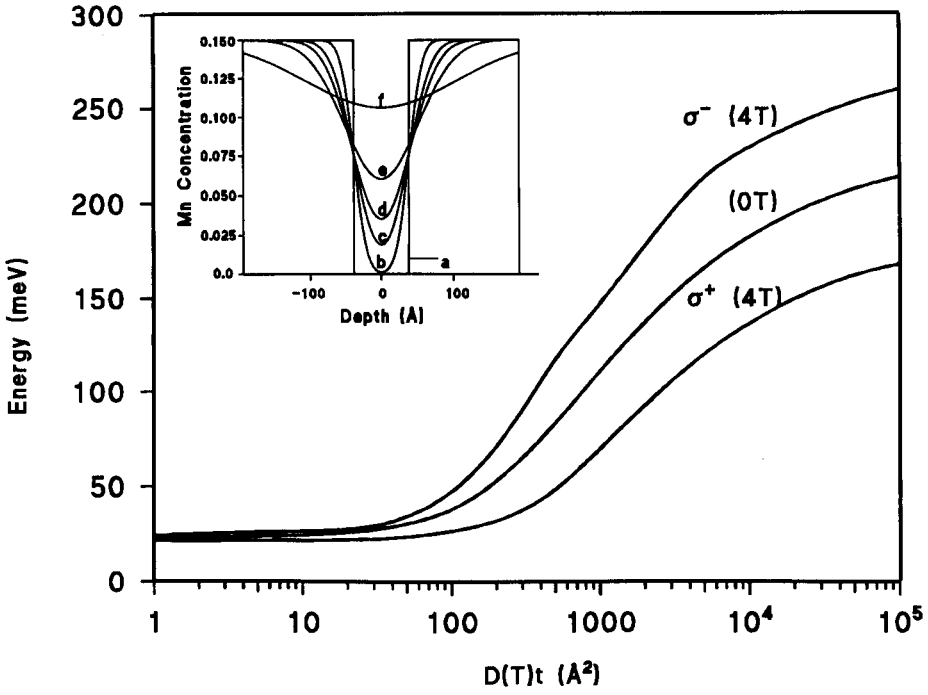

Figure 3.31: (a). Calculated energy of the e1hh1 exciton in a single QW at 0T and 4T for both σ^+ and σ^- components with different amounts of diffusion DT. (b). Calculated potential well profiles following diffusion of the Mn ions from the barrier region into the QW for DT values of [a] 0, [b] 10^2, [c] $3x10^2$, [d] $5x10^2$, [e] 10^3, and [f] $5x10^3$ Å^2.

melt front then D(T)t would be 300 Å^2. Hence the first QW beneath the melt front is expected to have a value of D(T)t in this range. The value found for the QW that produces emission D is at the lower end of this range, whilst the value for D(T)t found for the equivalent emission in the 100 mJ cm^{-2} is estimated as 500 Å^2. Both values lie within the range expected for a QW that lies just below the melt front. Returning to figure 3.30 the initial slope is such that the corresponding figures of D(T)t for the second QW below the melt front are 300 and 25 Å^2 . Again the value found for emission E is at the lower end of this range. Altogether these values provide striking confirmation of two points. Firstly that rapid diffusion of Mn atoms occurs in the QW just beneath the melt front following PLA, but that the diffusion is very much less in the underlying QWs. Secondly that the one dimensional model of heat diffusion described in section (3.4.2), although assuming a number of simplifying assumptions, gives a perfectly adequate description of PLA in a semiconductor such as CdTe.

Finally, we consider the behaviour of the DCXRD spectra as the fluence is increased. Here the significant feature is that the QW peaks, figure 3.5, have disappeared at a fluence of 150 mJ cm^{-2}, which we attribute to the diffusion in all of the QWs. Even partial homogenization would probably lead to the loss of the QW satellite lines which are already relatively broad in the control sample. At 180 mJ cm^{-2} the underlying buffer layer peak has decreased and broadened to between -500 and +1000

arc sec. We tentatively attribute this to melting to the top part of the buffer layer and the generation of tensile and compressive strains, of up to 0.6 and 0.2 % respectively, following cool-down.

3.9.2 Observations of Stokes Shift and Bound Magnetic Polarons in the MQW Annealed Structure

Energy shifts of several meV between photoluminescence excitation absorption lines and the corresponding photoluminescence emission have been obtained experimentally in both III-V and II-VI quantum wells [53,54]. These shifts, which are known as Stokes shifts, were found to exist even in high-quality materials exhibiting narrow absorption and emission lines. These shifts can be attributed to small scale interface disorder [55]. In photoluminescence, carriers are excited by the incoming photons and free excitons are created. These free excitons are able to wander around in the plane of the well quite easily. At low temperatures they are unable to advance into areas of increased disorder (comparable to where they were created), since this movement would require an increase of the total energy of the system. Nevertheless, the excitons are able to release acoustic phonons and lower their energy by moving into regions of lower disorder. Therefore, when the exciton finally recombines and emits a photon in the process, it will be red-shifted with regard to the absorption. Moreover, the presence of magnetic polarons, as well as well width fluctuations, contributes to the Stokes shift.

In the present sample, Stokes shifts have been observed on all of the transitions. The energy difference between the peak of e1hh1 transition observed in PLE, figure 3.15, and in PL, figure 4.5, is 11 meV, 6 meV, 4 meV, and 4 meV for emissions D, E, D^0X of the 90 mJ cm^{-2} annealed sample and the D^0X emission of the control sample respectively, as shown on table 3.2. With less Mn in the QW the Stokes shift is smaller. For the D^0X emission the Stokes shift arises partly from the localisation energy of the exciton to the D^0 centre and partly from wellwidth fluctuations. However for the diffused QWs the Stokes shift is expected to arise from the formation of the bound magnetic polaron in the QWs, as has been observed in QWs with abrupt interfaces when the width of the QW is less than about 30 Å [56, 57].

	(D^0X Emission) Control Sample	(D^0X Emission) Annealed Sample	(Emission E) Annealed Sample	(Emission D) Annealed Sample
Stokes shift (meV)	4	4	6	11

Table 3.2: Stokes shifts of the control sample and 90 mJ cm^{-2} annealed sample for the D^0X, E, and D emissions.

Furthermore the FWHM of the D^0X emission observed in figure 3.6 is about 3 meV which corresponds to a one monolayer well width fluctuation.

In fact another unusual phenomenon was observed in the present sample. This is the bound magnetic polaron formation, which was observed when performing the PL measurements at different magnetic fields on the diffused QWs. Details about magnetic

polarons in diluted magnetic semiconductors were described in section 3.7.4.3. However, experimental and theoretical investigations of the magnetic polaron effects in semimagnetic QWs and SLs have also been carried out [58,59]. It was found that in CdTe/CdMnTe structures the magnetic polaron energy depends markedly on the well width [57,59]. When the well width is increased the magnetic polaron energy decreases sharply. Furthermore, when the well width is above 30 Å, the magnetic polaron energy becomes less than 1 meV [57]. Figure 3.7 shows the PL spectra of the control sample at different magnetic fields, while figure 3.8 represent the energy shift of emission A at various magnetic fields. A comparison between the measured energy shifts of emission A vs magnetic field and calculated values of these shifts were carried out using equations (3.45) and (3.46). The best fit were obtained, because of the absence of magnetic polarons at high magnetic field, at a Mn concentration of 12.5%, figure 3.8, which agrees with the value obtained from the L_2 transition, equation (3.52). At zero magnetic field, the magnetic polaron energy has a value of 20.4 meV. The same calculations were performed on the 70 mJ cm^{-2} annealed sample, figures 3.9 and 3.10. The best fit was attained at Mn concentration of 14.5% (emission B) and the corresponding magnetic polaron energy at zero field was found 22.65 meV. Similarly, the 90 mJ cm^{-2} annealed sample was treated at the same way, figure 3.11 and 3.12, and a value of 16.5% of the Mn concentration was calculated (emission C). The magnetic polaron energy was calculated as 32.2 meV. Figure 3.13 and 3.14 shows the PL spectra and the energy shift of emission C at different magnetic fields, respectively. The Mn concentration was estimated as 17.6% (emission C) and the corresponding magnetic polaron energy was 31.14 meV, table 3.3.

	Control Sample	70 mJ cm^{-2} Annealed Sample	90 mJ cm^{-2} Annealed Sample	100 mJ cm^{-2} Annealed Sample
BMP Energy (meV)	20.4	22.65	32.2	31.14

Table 3.3: The bound magnetic polaron energy for the control sample and the 70, 90, 100 mJ cm^{-2} annealed samples.

The magnetic polaron energy as a function of the Mn concentration of the control, 70, 90, and 100 mJ cm^{-2} annealed samples is illustrated in figure 3.32. The diagram below shows that above a laser fluence of 100 mJ cm^{-2} (correspond to Mn concentration of x=17.6%) the magnetic polaron energy starts to decrease.

Furthermore, according to the results obtained in section 3.9.1, we expect that the diffused QWs are asymmetrical as the integrated diffusion, Dt, changes very rapidly with depth in the 90 mJ cm^{-2} annealed sample, figure 3.30. This is expected to make the interface of the QW closest to the molten layer to suffer more diffusion than the other side of the QW. One consequence of an asymmetrical QW is to relax the strictly forbidden $\Delta n=\pm 1$ selection rule, but no evidence of forbidden QW transition eg., e1hh2 and e2hh1 transitions, have been found in the samples studied.

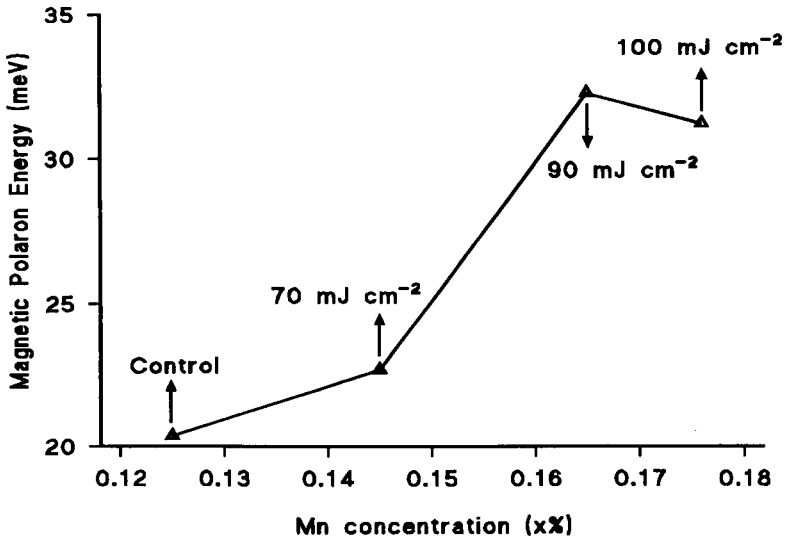

Figure 3.32: Measured magnetic polaron energy as a function of the Mn concentration of the CdMnTe layers of the control, 70, 90, 100 mJ cm^{-2} annealed samples.

3.10 Conclusion

The amount of diffusion associated with a laser fluence of 90 mJ cm^{-2} has been found, D(T)t = 300 Å. A simple diffusion model based on the heat diffusivity of the laser pulse into the sample was found to give an accurate values of diffusion and in good agreements with the experimental values. We found that the diffusion coefficient drops by a factor of 10 when the pulse heat progress from one QW to another beneath the melt front of the sample. Stokes shifts and magnetic polarons were observed in the present sample and values were estimated for both at different laser fluences.

More work is still needed to be done on stokes shift and magnetic polarons in these annealed samples to discover the mechanism and the behaviour of these remarkable phenomena.

References

[1] G. A. Kachurin, N. B. Pridachin, and L. S. Smirnov, Sov. phys. Semicon. 9 pp 946 (1976).

[2] J. M. Faifield, and G. H. Schwuttke, Solid. State. Electron. 11 pp 1175 (1968).

[3] J. Narayan, R. T. Young, and C. W. White, J. Appl. Phys. 49, 3912 (1978); C. W. White, J. Narayan, and R. T. Young, Science 204, 461 (1979).

[4] J. C. Beam, H. J. Leamy, J. M. Poate, G. A. Rozgonyi, T. T. Sheng, J. S. Williams, and G. K. Celler, Appl. Phys. Lett. 33, 227 (1978).

[5] R. T. Young, J. Narayan, and R. F. Wood, Appl. Phys. Lett. 35, 448 (1979).

[6] J. Narayan, R. T. Young, R. F. Wood, and W. H. Christie, Appl. Phys. Lett. 33, 338 (1978).

[7] J. Narayan, and F. W. Young, Jr., Appl. Phys. Lett. 35, 330 (1979).

[8] I. B. Khaibullin, E. I. Shtyrkov, M. M. Zaripov, R. M. Bayazitov, and Galjautdinov, Radiation Effect 36, 225 (1978).

[9] J. Narayan, and C. W. White " Laser and Electron Beam Processing of Materials" edited by C. W. White, and P. S. Peercy., Academic Press INC, NewYork (1980).

[10] D. A. Auston, J. A. Golovchenko, A. L. Simons, C. M. Surko, and T. N. C. Venkatesan, Appl. Phys. Lett 34, 777 (1979).

[11] C. W. White, P. P. Pronko, S. R. Wilson, B. R. Appleton, J. Narayan, and R. T. Young, J. Appl. Phys. 50, 3261 (1979).

[12] B. R. Appleton, B. C. Larson, C. W. White, J. Narayan, S. R. Wilson, and P. P. Pronko, Laser-Solid Interactions and Laser Processing , ed. by H. J. Leamy, and J. M. Poate (AIP, NewYork p.291 1979)

[13] M. Bertolotti, G. Vitali, and W. E. Spear " Laser and Electron Beam Processing

of Materials" edited by C. W. White, and P. S. Peercy., Academic Press INC, NewYork (1980).

[14] S. U. Campisano, Solid State Electron. 21, 485 (1978).

[15] P. Baeri, S. U. Campisano, G. Foti, and E. Ramini, J. Appl. Phys. 50, 788 (1979) and references therein.

[16] R. Tsu, J. E. Baglin, G. J. Lasher, and J. C. Tsang, Appl. Phys. Lett. 34, 153 (1979) and references therein.

[17] P. A. Barnes, H. J. Leamy, J. M. Poate, S. D. Ferris, J. S. Williams, and G. K. Celler, Appl. Phys. Lett. 33, 965 (1978).

[18] *Optical Properties of Solids*, edited by F. Wooten, Academic Press, NewYork (1972).

[19] *Laser Annealing of Semiconductors*, edited by J. M. Poate, and James. W. Mayer., Academic Press, London (1982).

[20] K. M. Shvarev, B. A. Baum, and P. V. Gel'd, Sov. Phys.-Solid State (Engl. Transl.) 16, 2111 (1975).

[21] M. K. El-Adawi, M. A. Abdel-Naby, and S. A. Shalaby, Int. J. Heat Mass Transfer. Vol. 38, No. 5, pp. 947-952 (1995).

[22] J. F. Ready, Effects due to absorption of laser radiation, J. App. Phys. 36 (2), 462-468 (1965).

[23] *The Mathematics of Diffusion*, edited by J. Crank, Clarendon Press, Oxford (1975).

[24] *Diffusion in Solids*, edited by P. G. Shewmon, Mc. Graw-Hill Book Company, NewYork (1963).

[25] P.Harrison, E.E.Hagston, T.Stirner, Phys. Rev. B47, 16404 (1993).

[26] F. Spaepen, and D. Turnbull " Laser Annealing of Semiconductors" edited by J. M. Poate, and James. W. Mayer., Academic Press, London (1982).

[27] C. W. White, B. R. Appleton, and S. R. Wilson " Laser Annealing of Semiconductors" edited by J. M. Poate, and James. W. Mayer., Academic Press, London (1982).

[28] P.Chen. PhD. Thesis, University of Hull, UK, 1997.

[29] S. B. Oseroff, Phys. Rev. B 25, 6484 (1982).

[30] J. A. Gaj, R. Planel, and G. Fishman, Solid State Commun. 29, 435 (1979).

[31] Y. Shapira, S. Foner, D. H. Ridgely, K. Dwight, and A. Wold, Phys. Rev. B 30, 4021 (1984).

[32] R. L. Aggarwal, S. N. Jasperson, P. Becla, and R. R. Galazka, Phys. Rev, B 32, 5132 (1985).

[33] J. K. Furdyna, J. Appl. Phys. 64, R29 (1988).

[34] C. Domb, and N. W. Dalton, Proc. Phys. Soc. (London) 89, 859 (1966).

[35] J. A. Gaj, J. Ginter, and R. R. Galazka, Phys. Status. Solidi. B 89, 655 (1978).

[36] J. A. Gaj, in Semiconductors and Semimetals, R. K. Willardson, and A. C. Beer, Treatise Editors; J. K. Furdyna, and J. K. Kossut, Volume Editors (Academic, Boston, MA, 1988) Vol. 25, p. 275.

[37] M. A. Buttler, S. J. Martin, and Baughman, Appl. Phys. Lett. 49, 1053 (1986).

[38] W. E. Hagston, T. Stirner, P. Harrison, O. F. Holbrook, and J. P. Goodwin, Phys. Rev. B 50, 5264 (1994).

[39] P. A. Wolff, and J. Warnock, J. Appl. Phys. 55, 6 (1984).

[40] T. J. Gregory, C. P. Hilton, W. E. Hagston, J. E. Nicholls, and J. J. Davies, Semicond. Sci. Technol. 7, 912 (1992).

[41] P.J.Dean, G.M.Williams and G.Blackmore, J. Phys D: Appl. Phys.17, 2291 (1984).

[42] A. Twardowski, M. Nawrocki, and J. Ginter, Phys. Statues. Solidi 96. 497 (1979).

[43] D. Heiman, P. Becla, R. Kershaw, D. Ridgley, K. Dwight, A. Wold, and R. R. Galazka, Phys. Rev. B 34. 3961 (1986).

[44] T. J. Gregory, J. E. Nicholls, J. J. Davies, J. O. Williams, and N. Maung, Semicond. Sci. Technol. 3, pp. 1193-1195 (1988).

[45] P. A. Wolff, Semiconductors and Semimetals, Edited by J. K. Furdyna, and J. Kossut (NewYork: Academic 1988), Vol 25, p 413.

[46] T. J. Gregory, C. P. Hilton, W. E. Hagston, J. E. Nicholls, and J. J. Davies, Semicond. Sci. Technol. 7, 912-917 (1992).

[47] A. Wasiela, Y. Merle d'Aubigne, J. E. Nicholls, D. E. Ashenford and B. Lunn, solid. Stat. Commun, 76. 263 (1990).

[48] A. Wasiela, P. Peyla, Y. Merle d'Aubigne, J. E. Nicholls, D. E. Ashenford and B. Lunn, Semicond. Sci. Technol. 7, 571 (1992).

[49] J. P. Hayes, H. V. Snelling, D. Sands, A. G. Jenner, and R. D. Greenough, "Proceedings of the XI International Symposium on Gas Flow and Chemical Lasers and High-Power Laser Conference", SPIE Volume 3092 pp. 643-646 (1996).

[50] N.Y.Jamil, PhD.Thesis, University of Hull, UK, 1990, p.87.

[51] D. Tönnies, G. Bacher, A. Forchel, A. Waag, and G. Landwehr, Appl. Phys. Lett. 64, 766 (1994).

[52] T.Piorek, P.Harrison, W.E.Hagston, Phys. Rev. B52, 14111 (1995).

[53] M. J. L. S. Haines, N. Ahmed, S. J. A. Adams, K. Mitchell, I. R. Agool, C. R. Pidgeon, B. C. Cavenett, E. P. O'Reilly, A. Ghiti, and M. T. Emeny, Phys. Rev. B 43, 11944 (1991).

[54] V. A. Wilkinson, A. D. Prins, J. D. Lambkin, E. P. O'Reilly, D. J. Dunstan, L. K. Howard, and M. T. Emeny, Phys. Rev. B 42, 3113 (1990).

[55] W. E. Hagston, P. Harrison, and T. Stirner, "Advanced Materials for Optics and Electronics", Vol 3, 95 (1994).

[56] T. Stirner, W. E. Hagston, P. Harrison, and J. P. Goodwin, J. Appl. Phys. 75, 7, 3466 (1994).

[57] T. Stirner, P. Harrison, W. E. Hagston, and J. P. Goodwin, Phys. Rev. B 50, 8, 5713 (1994).

[58] D. R. Yakovlev, W. Ossau, G. Landwehr, R. N. Bichnell-Tassius, A. Waag, S. Schmeusser, and I. N. Uraltsev, Solid State Commun. 82, 29 (1992).

[59] D. R. Yakovlev, G. Mackh, B. Huhn-Heinrich, W. Ossau, A. Waag, G. Landwehr, R. Hellmann, and E. O. Gobel, Phys. Rev. B 52, 12033 (1995).

Chapter 4

Low-Power Pulsed Laser Annealing of Ion Implanted CdTe/CdMnTe DQW Structures

4.1 Introduction

One of the first applications of semiconductor laser annealing was the removal of defects in ion implanted layers [1] and a considerable amount of work has been carried out by this tool in semiconductor processing and device manufacture. During the last several years different techniques have been developed for annealing samples with structural disorder introduced through ion implantation, and several of these techniques found their way to the application sector [2]. Ion implantation of thin film structure by accelerating ions to keV energies is accompanied by damage to the host crystal. This damage takes the form of dislocations, stacking faults, dislocation loops, and a variety of point defects, which can to some extent be removed by thermal annealing, but this treatment leads to degradation of electrical performance. Laser annealing of the ion-implanted layers has defeated several of these boundaries [1], [3]. With pulsed laser heating, complete recrystallization of the implanted layers has been achieved [4].

The present chapter is mainly concerned with CdTe/CdMnTe DQW structures. The main purpose of this work is to study laser annealing and diffusion effects on the DQW structure by implanting it with Ar^{+2} ions to increase the defects of the crystal structure. Hence low-power pulsed laser annealing is used to anneal out the damage caused by the ion bombardment without melting the material. The damage and its recovery is monitored by the optical properties of the QWs. Another aspect of the present work is to determine the extent of diffusion and to calculate the diffusion coefficient, since the diffusion is dramatically enhanced in the implanted samples.

Several techniques such as a Photoluminescence (PL) Spectroscopy, Photoluminescence Excitation (PLE) Spectroscopy and Double Crystal X-Ray Diffraction (DCXRD) have been used to examine the nature and extent of diffusion in the DQW structures. Theoretical models have been also used, such as Rocking Curve Analysis by Dynamic Simulation (RADS) and The Trim Computer Program to calculate

the Stopping and Range of Ions in Matter [5]. The samples, which are the subject in this work, have been grown using the Molecular Beam Epitaxy (MBE) growth technique.

4.2 Ion Implantation process

4.2.1 Introduction

Ion implantation has been a considerable interest in the modification of surface layers using ion beams. Surfaces play an essential role in many technologies, such as integrated circuit fabrication and up to now the most successful surface alteration in semiconductor technology has been ion implantation in QW structures. Quantum well intermixing has been performed using ion implantation on GaAs/AlGaAs structures to increase the bandgap energy in a spatially selective manner [6], [7]. Furthermore ion implantation has regularly been utilized to alter the shape of quantum wells following thermal annealing by enhancing the interdiffusion [8]. It has been announced by many researchers [8, 9] that diffusion of the vacancies created by the ion implantation are responsible for enhanced intermixing.

4.2.2 Fundamental Processes of Ion Implantation

Four basic processes are expected to take place when a beam of ions is directed into a material [10]. When a single ion of keV energies is accelerated towards the target, a series of energy-loss collisions happens. One is regarded as nuclear collisions (collisions with the target atoms) and the other is regarded as electronic collisions (collisions with electrons). The implanted ions come to rest few hundreds of atoms

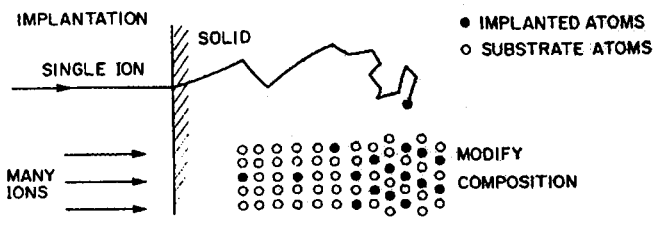

Figure 4.1: A schematic diagram of the implantation process of an energetic ion beam.

beneath the surface, figure 4.1. The radiation damage caused by an energetic ion beam is illustrated in figure 4.2. The lattice atoms are scattered from their original sites while the ions are penetrating the target. A single heavy ion can lead to the displacement of many hundreds of lattice atoms within a volume surrounding the ion trajectory. These processes result in the production of completely amorphous zones about ion tracks in semiconductors. Ion irradiation can also cause a sputtering processes, where the surface atoms are rejected from their lattice sites, figure 4.3. This process can lead to appreciable erosion of the target surface, hence erosion of an unwanted species on the surface can be achieved.

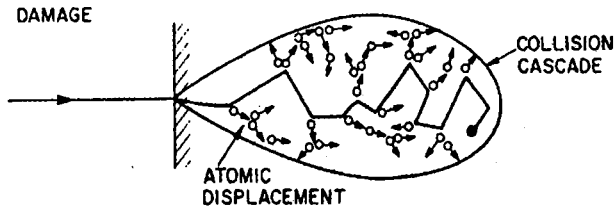

Figure 4.2: An illustration of the irradiation damage process using energetic ion beam.

The final implantation process is atomic intermixing, figure 4.4. This process allows metastable phases and novel alloys to be produced.

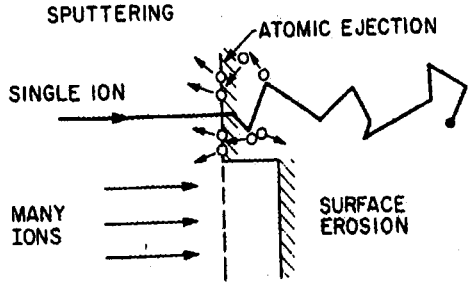

Figure 4.3: A schematic diagram of the sputtering process using energetic ion beam.

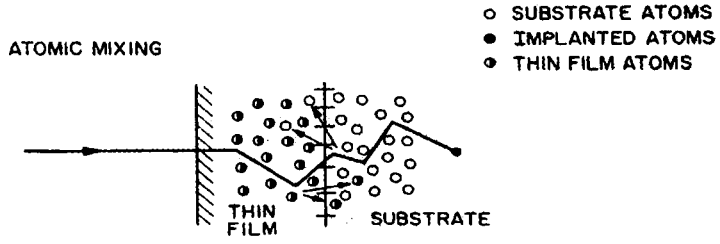

Figure 4.4: A schematic diagram of the atomic mixing process using energetic ion beam.

4.2.3 The Ion Implantation System at the University of Hull for Research Purposes

The system as illustrated in figure 4.5 consists of [9]:

1- The Ionization Stage where the arc-chamber is filled with argon gas. The argon atoms are then ionized by collisions with the accelerated electrons coming from the heated filament.

2- The Acceleration Stage in which ions are accelerated by applying a high potential of about ≤ 300 kV.
3- The Focussing Stage where the resulting beam enters a mass spectrometer after being focused by electrostatic quadrupole focusing elements. Subsequently only one isotope with the desired mass can pass through if the isotope selection slit is sufficiently small.
4- The Scanning Stage where the beam passes through two sets of electrostatic scanning plates to be scanned over the target area to ensure a uniform distribution of ions. The entire process takes place in a vacuum to prevent impacts with atoms of the air.

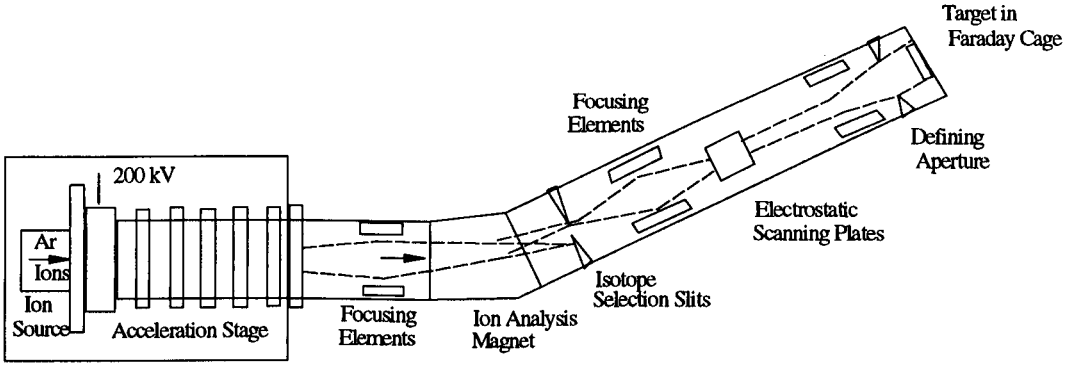

Figure 4.5: The Ion Implantation System at The University of Hull.

4.2.4 Ion Range Theory

Two main independent processes act to slow down the implanted ion and reduce its energy, namely nuclear and electronic collisions.
The total path length for an ion slowing down from an energy E_0 [11] can be written as:

$$R = \frac{1}{N}\int_0^{E_0} \frac{dE}{S_n(E) + S_e(E)} \tag{4.1}$$

where N is the number of target atoms per unit volume, E_0 is the initial ion energy, E is the ion energy, $S_n(E)$ and $S_e(E)$ are the nuclear and electronic stopping powers respectively. The solution of equation (4.1) is the average total distance travelled by a particle in coming to rest. At high energies electronic stopping dominates the slowing down process and the ion path is essentially a straight line in the original direction of motion, but with slight deflections at the end of its trajectory due to nuclear collisions, whereas at low energies nuclear stopping is the dominating process and the ion suffers large deflections and its path looks like a zigzag shape [11], figure 4.6. When only nuclear stopping is considered, the total range (the distance between the surface and the point where the ion comes to rest) in the fundamental units of $\mu g/m^2$ can be written as:

$$R_{tot} = \frac{3}{5}\frac{\sqrt{\sqrt[3]{Z_1^2} + \sqrt[3]{Z_2^2}}}{Z_1 Z_2}\frac{(M_1 + M_2)M_2}{M_1}E \qquad (4.2)$$

where Z_1 and Z_2 are the atomic numbers of the incoming ion and the target atom respectively. The above equation was obtained using a simplified scattering potential represented by the inverse square relationship i.e. $V(r) \sim 1/r^2$ and the energy E is measured in keV. The best well known theory for calculating ion ranges, due to Lindhard, Scharff and Schiøtt (LSS), can be found in many references [11], [12]. In

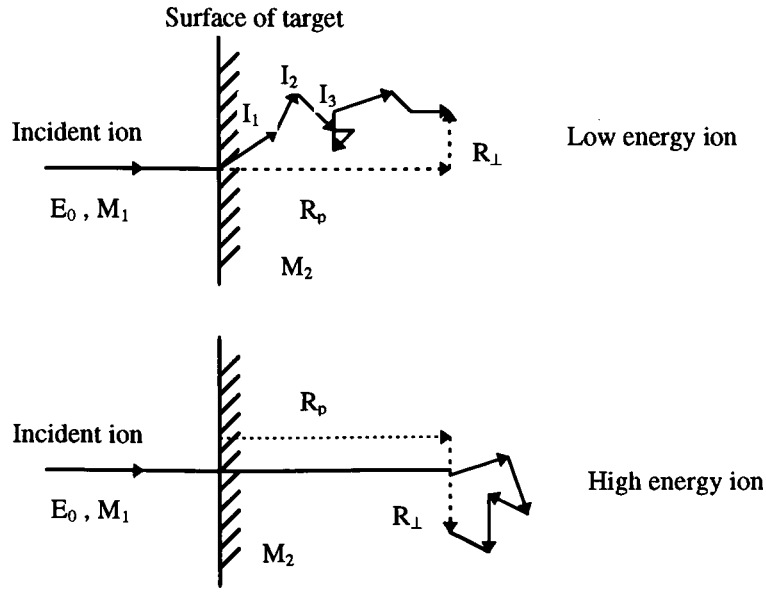

Figure 4.6: Basic range concept for low and high energy ions.

many cases we must consider the average projected range R_p (the mean penetration distance of the ion beam into the target) and the standard deviation ΔR_p as can be seen in figure 4.7. A differential equation relating the total range with the average projected range have been calculated by using the LSS theory:

$$\frac{R_{tot}}{R_p} = \frac{1}{4}\left[\left(\frac{M_2}{M_1} + 5\right)\frac{M_1 - M_2}{2M_1}\arccos\left(\frac{M_1 - M_2}{M_1 + M_2} - 3\frac{M_2}{M_1} - 1\right)\right] \qquad (4.3)$$

where M_1 and M_2 are the mass of the incoming ion and the target atom respectively. Equation 4.3 can be approximated and simplified as:

$$\frac{R_{tot}}{R_p} = 1 + \frac{M_2}{3M_1} \qquad (4.4)$$

This formula is well applied when $M_1 > M_2$ but it still gives reasonable results when $M_1 < M_2$. The above calculations, using the Thomas-Fermi Potential, can be solved

numerically by Monte-carlo simulations and the results can be found using the TRIM computer program described below.

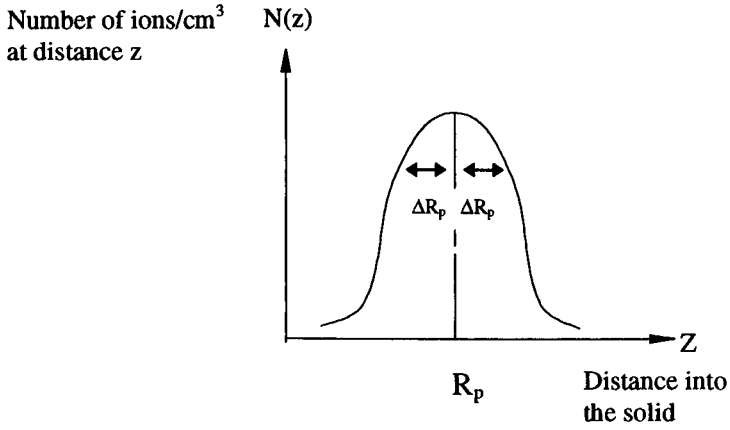

Figure 4.7: Gaussian distribution of the ion.

4.3 Diffusion Mechanisms in Semiconductors

Diffusion is the movement of atoms or molecules driven by a concentration gradient in the chemical potential. Diffusion mainly occurs in solids when some atoms possess enough kinetic energy (due to thermal vibrations) which exceeds the activation energy of the atoms in the material. Atom therefore can move from one lattice site to another. In fact diffusion in solids occurs with the help of point defects such as vacancies and interstitials and the diffusion coefficient strongly depends on the concentration and mobility of these defects as well as temperature. To have a better idea about the diffusion of atoms in solids and to fully understand the behaviour of the diffusion coefficient, it is very important to study the diffusion mechanisms by which atoms migrate in solids as shown below.

I. Vacancy Diffusion

Vacancy diffusion is often considered the dominant diffusion mechanism [13]. Empty lattice sites exist in every crystal and their number increases with temperature. This process takes place when one atom moves from its native lattice site into the neighbouring vacancy. Usually a small energy is needed to carry out this mechanism and the diffusion coefficient is proportional to the density of vacancies, figure 4.8.

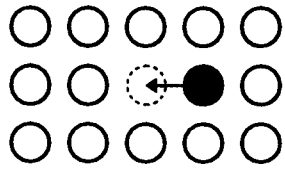

Figure 4.8: Vacancy diffusion mechanism.

II. Divacancy Mechanism

Alternatively, a bound pair of neighbouring vacancies (either two vacant sites of the same sublattice or a pair of vacancies from the anion and cation sublattices) may jump into a pair of native lattice sites next to each other, as shown in figure 4.9.

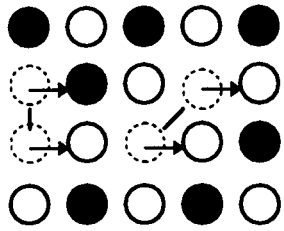

Figure 4.9: Divacancy diffusion mechanism.

III. Interstitial Diffusion

Interstitial diffusion mechanism is quite important for atoms which can occupy interstitial sites. Those atoms can easily jump into neighbouring interstitial sites and therefore give rise to diffusion, figure 4.10.

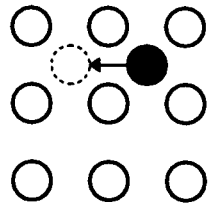

Figure 4.10: Interstitial diffusion mechanism.

IV. Interstitialcy Diffusion

Some atoms are able to move out of their original lattice sites into interstitial ones (due to the entropy gain). Then the interstitial atoms can knock regular atoms out of their positions into interstitial ones, as can be seen in figure 4.11.

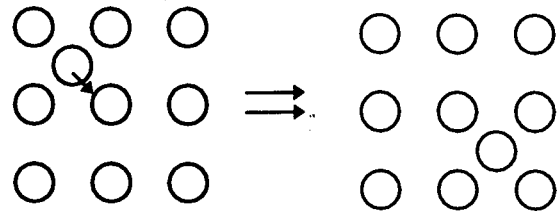

Figure 4.11: Interstitialcy diffusion mechanism.

V. Ring Mechanism

When two atoms exchange their positions in crystal lattice, large distortion of the lattice vicinity occurs. Now if more than two atoms engage in a cyclical exchange, we then have the ring mechanism as shown in figure 4.12.

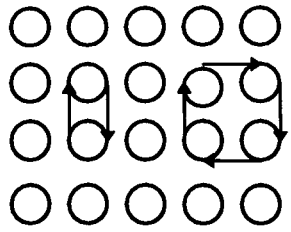

Figure 4.12: Ring diffusion mechanism.

VI. Interstitial substitutional mechanisms

1. The Frank-Turnbull or Longini mechanism: This process takes place when an impurity atom sites on an interstitial position recombines with a vacancy in the lattice, figure 4.13.

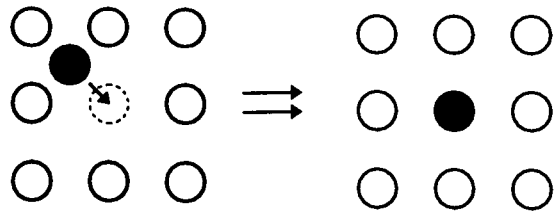

Figure 4.13. The Frank-Turnbull or Longini mechanism.

2. The kick out or dissociative mechanism: An impurity atom sites on an interstitial site can kick a lattice atom out of its native position into an interstitial site and occupy the empty lattice site, as shown in figure 4.14.

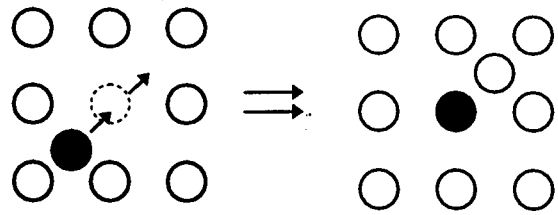

Figure 4.14: The kick out or dissociative mechanism.

4.4 Pulsed Laser Annealing

4.4.1 Introduction

Since the first demonstration of a pulsed ruby laser by Maiman in 1960, lasers have become significant and reliable sources of energy and are used on a routine basis in a number of industrial processing techniques. Today, lasers covering a broad range of wavelength, pulse characteristics, and output powers are available on the market [2]. The facility of rapidly heating and cooling surface layers with a laser without heating the bulk depends on the pulse time, which is typically of nanoseconds duration, and the coupling depths of the heat surface. Since the laser pulse only penetrates a small distance into the sample, melting of the surface region occurs, due to the large amount of heat delivered to the surface. This is then followed by recrystallization of the molten structure. While strong annealing is performed at the surface region, the remainder of the sample is almost unchanged. During the past decade there has been a very considerable growth of pulsed laser annealing techniques and their use to process semiconductors [14]. The potential of laser irradiation for annealing ion implantation damage has led to a substantial amount of work in this area [9].

Annealing also can be used to activate dopants and for the modification of the shapes of QWs [15]. It was reported that pulse laser irradiation has been used to perform intermixing of $Al_xGa_{1-x}As/GaAs$ superlattices without any detected residual damage within the structure [7]. Furthermore enhancement of luminescence by pulse laser annealing of ion-implanted europium in sapphire and silica has been carried out [16]. Pulsed excimer laser was employed for annealing damage caused by ion implantation and redistribution of impurities in SiC sample [17]. With compound semiconductors, techniques such as furnace annealing cannot be applied advantageously because they cause high thermal rises of the material near the surface, which is sufficient to cause dissociation of the material [18]. Furthermore, it was reported, in high-power laser annealing (HPLA), that the main mechanism to convert an implanted region into a single crystalline state is the melting of the material i.e., it is necessary that the threshold energy be applied to the sample [19,20]. As a result, the application of such a technique i.e., (HPLA), to a compound semiconductor such as GaAs involves the same difficulty encountered for the furnace annealing due to the volatility of As. Recent use of low-power pulsed laser annealing (LPPLA) has shown that below the melting threshold, an interval of the energy density of the laser pulses exists within which good annealing of the structure of implanted GaAs specimens can be achieved [21,22]. In the present work, pulsed laser annealing has been used to anneal out the damage caused by the ion bombardment and to restore the optical properties of the sample.

4.4.2 Pulsed Laser Annealing Technique

The implanted DQW structures were annealed using the pulsed laser annealing technique illustrated in figure 4.15. An excimer laser type Lumonics TE-860-4 XeCl with a wavelength of 308 nm and a maximum energy of 150 mJ and a pulse width of 26 ns was used. The laser beam enters an aperture and is then focused by a lens to hit the sample which is placed in a chamber. The annealing processes were done in air. Proper

Figure 4.15: Schematic diagram of Excimer pulse laser annealing technique.

filters were used where it is necessary to control the laser power which is measured by a Joulemeter.

4.5 Experimental Details

Two Double Quantum Well structures were employed in the present chapter, namely, sample 490 and sample 491. Sample 490 consisted of a very thick substrate layer (InSb) followed by the buffer layer (0.1 μm CdTe) then a thick layer of CdMnTe (0.2 μm) followed by the DQW layers as described below,

InSb (001) / 1000 Å CdTe / 2000 Å $Cd_{1-x}Mn_xTe$ / 80 Å CdTe / 300 Å $Cd_{1-x}Mn_xTe$ / 40 Å CdTe / 200 Å $Cd_{1-x}Mn_xTe$ /.

The Mn ion concentration, x, in the CdMnTe layers was 0.06. The layers were grown in the (001) direction. Sample 491 had exactly the same structure as 490 but the barrier layer between the two quantum wells was 500 Å wide. The 40 Å and 80 Å CdTe layers behaved as the first and second quantum wells. For ease we reference the 40 Å CdTe layer as the first quantum well and the 80 Å CdTe layer as the second quantum well.

PL measurements were carried out with the sample at 4.2 K. The excitation source was a Pyridine-2 dye laser, pumped with an Argon ion laser at 514 nm. The sample was mounted strain-free in the cryostat. The PL spectra and DCXRD rocking curves of the DQW structures were recorded after each stage of implantation and annealing. Different sections of the sample were implanted at different ion doses.

Figure 4.16 shows the experimental (A) and simulation (B) rocking curves of sample 490. The simulation was calculated using the dynamical theory of x-ray diffraction. The most intense peak, around 1600 arcseconds, is assigned to the substrate layer. Another intense peak located at 2000 arcseconds is identified as the reflection from the 2000 Å CdMnTe layer. A little peak, around 1450 arcseconds, sitting on the left tail of the substrate peak is attributed to the 1000 Å CdTe buffer layer and the rest of the peaks, at either side, correspond to the DQW layers. The best fit between the experimental and simulated rocking curves is met when the model was set at the following parameters:

InSb (001)/ 14 Å In_2Te_3/ 950 Å CdTe (40% relaxed)/ 1900 Å CdMnTe/ 71.2 Å CdTe/ 267 Å CdMnTe/ 35.6 Å CdTe/ 178 Å CdMnTe/.

From the x-ray simulation the Mn concentration was found to be 9.1%. The structures contained a highly mismatched layer a few monolayers thick at the InSb-CdTe buffer layer interface. This has been identified with the In2Te3 interfacial layer found at this interface by Raman Spectroscopy [23].

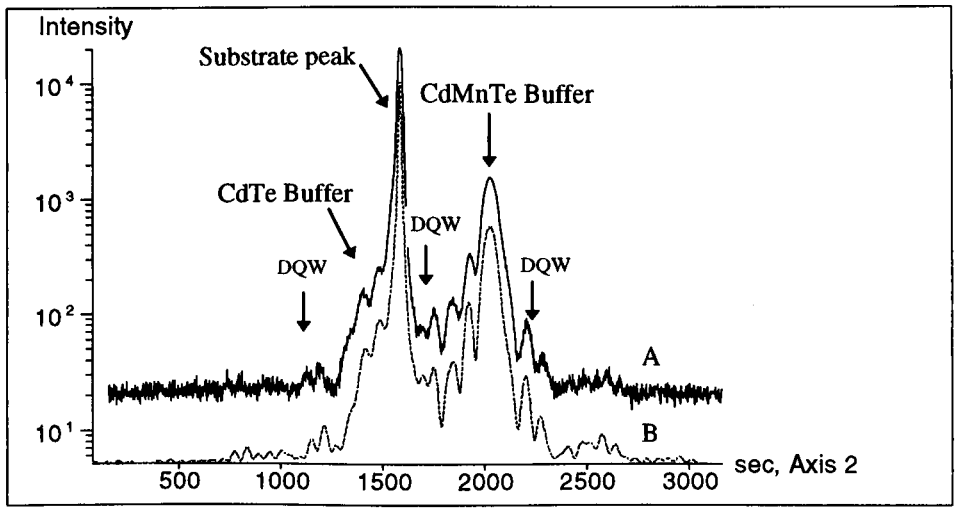

Figure 4.16: The experimental (A) and simulation (B) rocking curves of sample 490.

4.6 The TRIM 89 Computer Program

Prior to carrying out the experimental work a computer program using Monte Carlo calculations, the TRIM program (The Stopping and Range of Ions in Matter) [5], has been used to estimate the exact parameters of the implanted atoms into the target. These calculations are based on the LSS theory. Three different types of Trim Monte Carlo calculations are available. Ion distribution and quick calculation of damage, detailed calculation with full damage cascade and calculation of surface sputtering. The total number of vacancies, ion distribution, and some other interesting effects can be attained through the TRIM calculations. Our major interest is in the first type of calculation i.e. the ion distribution and quick calculation of damage. The ion energy and dose play a very significant part in the calculation because the ion range and distribution are highly dependant on both parameters. Several calculations based on a model of the DQW structure have been carried out to determine the ion energy at which most of the damage is created inside the first quantum well i.e. the 40 Å CdTe layer. At an energy where significant damage takes place in the first QW, some ions will also cause damage in the second QW. The idea of using a DQW structure is to damage the first QW and then achieving low-power pulsed laser annealing while the second QW i.e. the 80 Å CdTe layer is used as a reference. The implanted ions were Ar^{+2} and the total number of ions was 35000. Figures 4.17, 4.18, and 4.19 show total vacancies distributions of the DQW structure implanted with Ar^{+2} ions with different ion energies of 20, 26.2 and 30 keV respectively. The three previous figures indicate that the maximum amount of damage occurs approximately at the centre of the top 200 Å CdMnTe layer. In order to

push the maximum damage into the centre of the first QW this requires greater implantation ion energy but this is disadvantagous because the second QW will also be greatly damaged whereas our aim is to keep it undamaged as much as possible. At an ion energy of 20 keV, figure 4.17, three vacancies are created inside the first QW by each implanted ion. Figure 4.18 shows that each Ar^{+2} ion creates four vacancies inside the first quantum well when the ion energy is 26.2 keV. The ion energy was chosen on the basis of figure 4.18 where it is found that the maximum amount of damage occurs inside the first QW with a little damage to the second QW when the ion energy is 26.2 keV. At ion energy of 30 keV, figure 4.19, nearly four vacancies are created inside the first QW but the second QW is damaged. Different sections of the sample were implanted with different doses at ion energy of 26.2 keV.

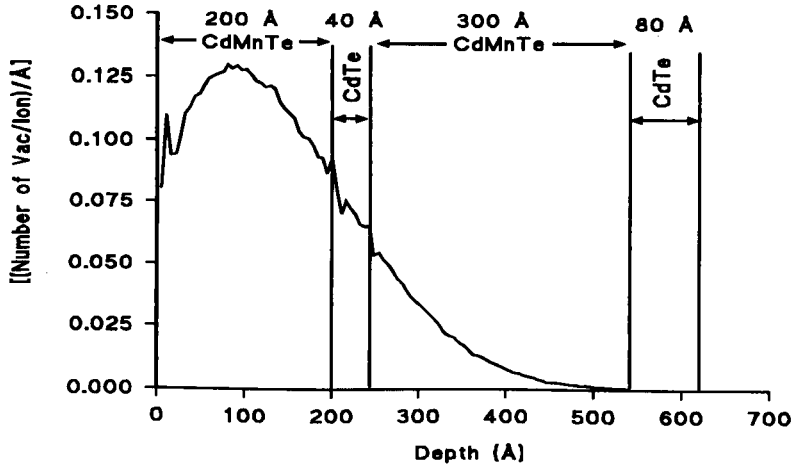

Figure 4.17: Vacancy distribution of the DQW structure at implantation of Ar^{+2} 20 keV.

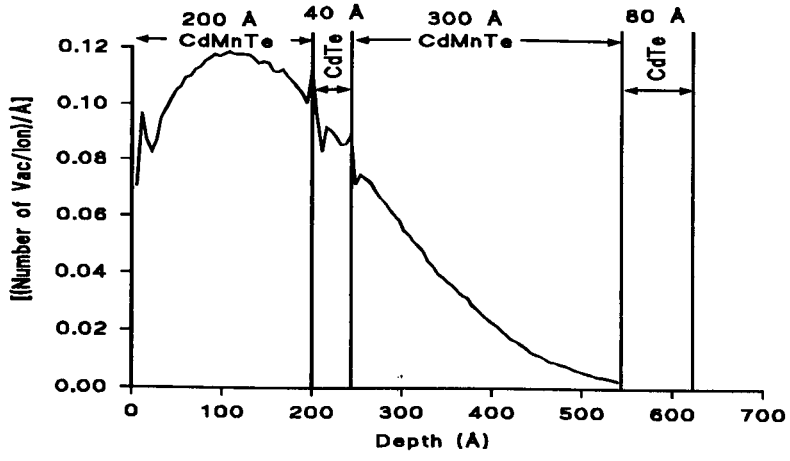

Figure 4.18: Vacancy distribution of the DQW structure at implantation of Ar^{+2} 26.2 keV.

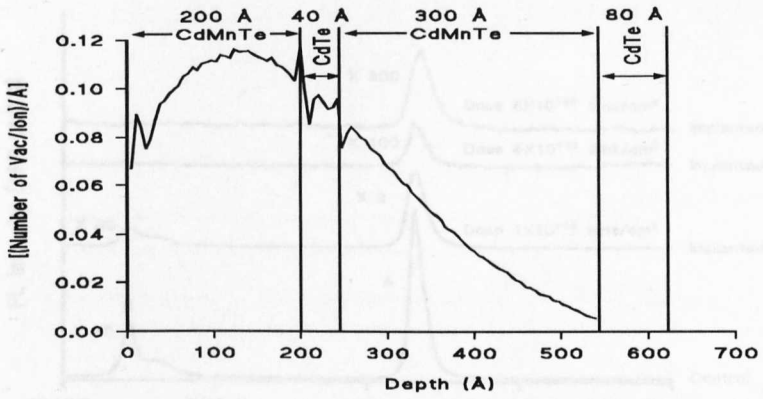

Figure 4.19: Vacancy distribution of the DQW structure at implantation of Ar^{+2} 30 keV.

4.7 Experimental Results

Sample 490 was initially implanted to create some damage then pulsed laser annealing was carried out on the implanted samples. The idea of damaging the first QW is to produce low-power pulsed laser annealing without melting the QW material, where the second QW is left as a reference. To study the nature and extent of the diffusion occurring in the DQW structure before and after the implantation process two techniques were used, namely photoluminescence (PL) spectroscopy and double crystal x-ray diffraction (DCXRD).

Table 4.1 shows the DQW samples used in this work with the treatments applied to each one. Figure 4.20 shows the PL spectra of the DQW structure before and after implantation at different ion doses of $1x10^{+13}$, $4x10^{+13}$ and $6x10^{+13}$ ions/cm^2 while the implanted ion energy was held as 26.2 keV. The lower intensity peak at 7445 Å is identified as the e1hh1 electron-hole recombination in the first quantum well (emission B) and the higher intensity peak around 7635 Å is assigned to emission from the second quantum well (emission A). It is obvious that increasing the ion dose leads to increasing the damage in the DQW structure which in turn causes quenching or decreasing of the PL emissions as seen in figure 4.20. After a dose of $4x10^{+13}$ ions/cm^2,

	490Q	490M	490N	491G	491H
Implantation Dose (ions/cm^2)	$4x10^{13}$	$4x10^{13}$	$4x10^{13}$	$4x10^{13}$	----------
Annealing Fluence "Single Shot" (mJ/cm^2)	30 50	40	50	40 50 60 70 80	30 50 60 70 80

Table 4.1: The DQW samples with the implantation doses and annealing fluences used in this chapter .

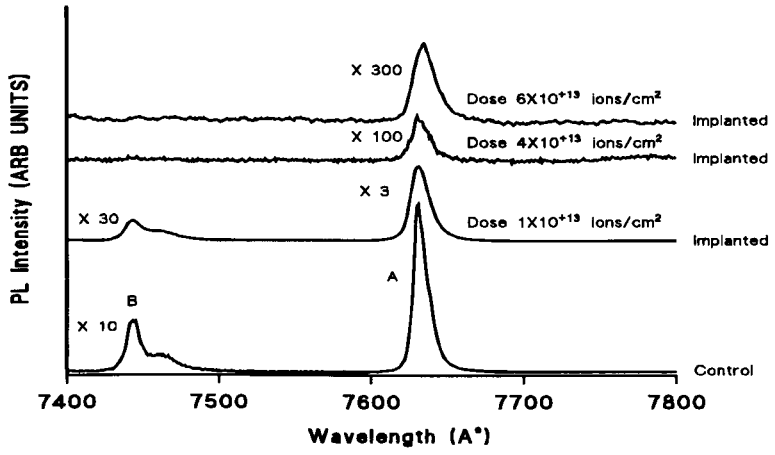

Figure 4.20: PL spectra of sample 490 before and after implantation at different ion doses $1x10^{+13}$, $4x10^{+13}$ and $6x10^{+13}$ ions/cm^2, all magnified peaks are referenced to peak A.

emission from the first QW nearly vanished while emission from the second QW is decreased by a factor of 10^2. According to these results the implantation dose was chosen as $4x10^{+13}$ ions/cm^2 and the implanted ions energy was kept as 26.2 keV. Three sections of sample 490 (Q, M and N) were implanted at a dose of $4x10^{+13}$ ions/cm^2 and ion energy of 26.2 keV. After the implantation process, the sample was then annealed at different laser fluences.

Sample 490Q was annealed at fluences of 30 and 50 mJ cm^{-2} progressively and after each annealing stage the PL spectrum and DCXRD rocking curve were recorded. Figure 4.21 shows DCXRD rocking curves of the control, implanted and annealed sample 490Q at a fluence of 50 mJ cm^{-2} (no changes were observed at a fluence of 30 mJ cm^{-2}). After the implantation process the DQW satellite peaks have almost disappeared. After annealing, the DQW satellite peaks reappear but with low intensities.

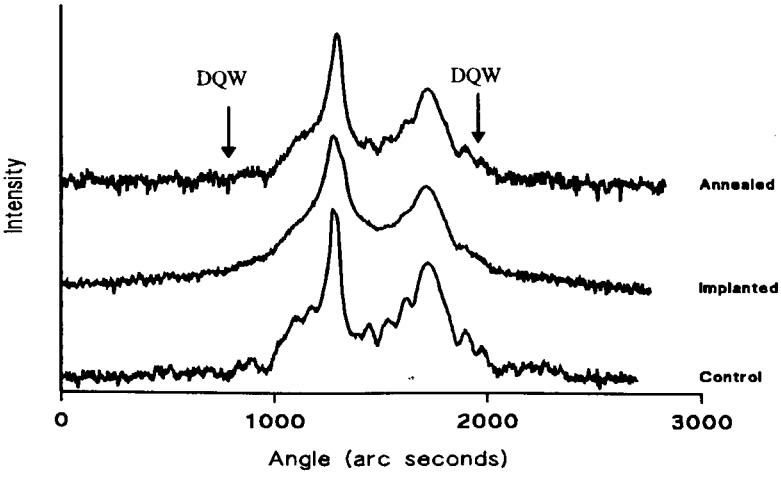

Figure 4.21: DCXRD rocking curves of the control, implanted, and annealed sample 490Q at a fluence of 50 mJ cm^{-2}.

The PL spectra of sample 490Q before and after each process are illustrated in figure 4.22. After annealing the implanted sample at a fluence of 30 mJ cm^{-2} no changes

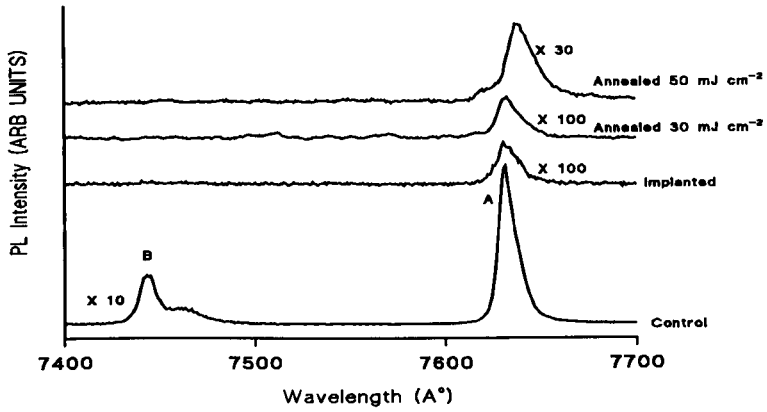

Figure 4.22: The PL spectra of the control, implanted, and annealed sample 490Q at fluences of 30 and 50 mJ cm^{-2}, all magnified peaks are referenced to peak A.

are observed in the PL spectrum or the DCXRD rocking curve. Again there is no sign of emission from the first QW (emission B) after annealing at a fluence of 50 mJ cm^{-2} but the intensity of emission A is increased, with the emission being red shifted by a small amount as shown in figure 4.22. The same conditions were applied to sample 490M but laser annealing was carried out at a fluence of 40 mJ cm^{-2}. Figure 4.23 shows DCXRD rocking curves. No significant changes are seen after the annealing process. The PL spectra of the control, implanted, and annealed sample 490M are seen in figure 4.24. A little decrease in the intensity of emission A is observed after annealing at a laser fluence of 40 mJ cm^{-2}.

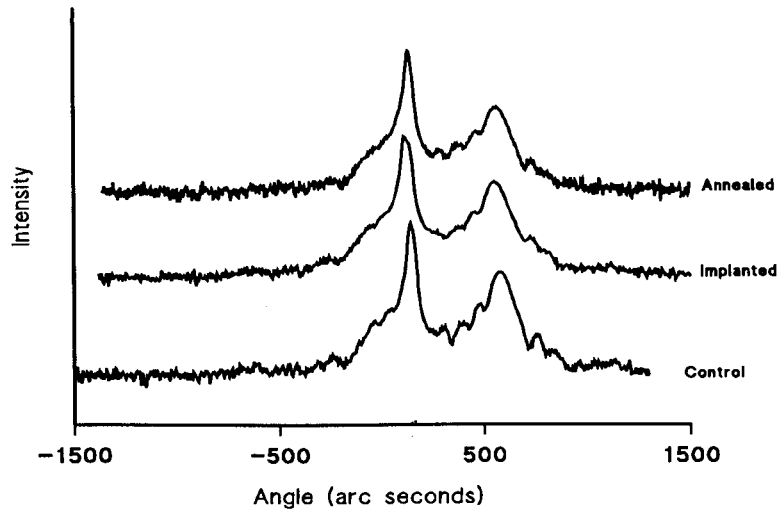

Figure 4.23: DCXRD rocking curves of the control, implanted and annealed sample 490M at a fluence of 40 mJ cm^{-2}.

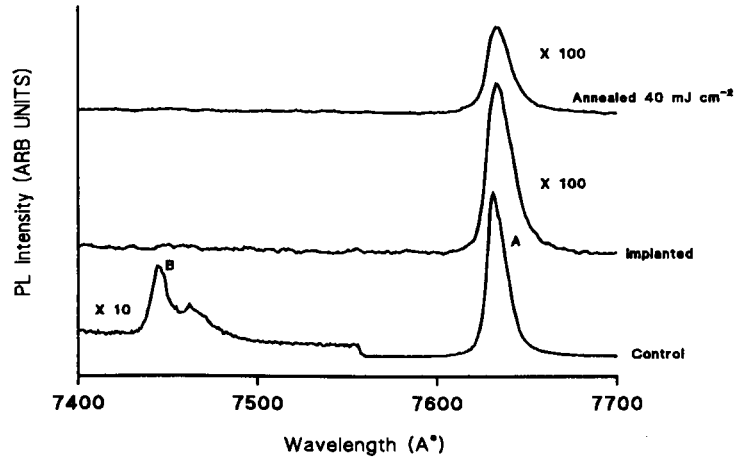

Figure 4.24: The PL spectra of the control, implanted, and annealed sample 490M at a fluence of 40 mJ cm^{-2}, all magnified peaks are referenced to peak A.

Sample 490N was annealed at a fluence of 50 mJ cm^{-2}. DCXRD rocking curves are shown in figure 4.25. No changes are observed after the annealing process. The PL spectra of the control, implanted, and annealed sample 490N are seen in figure 4.26.

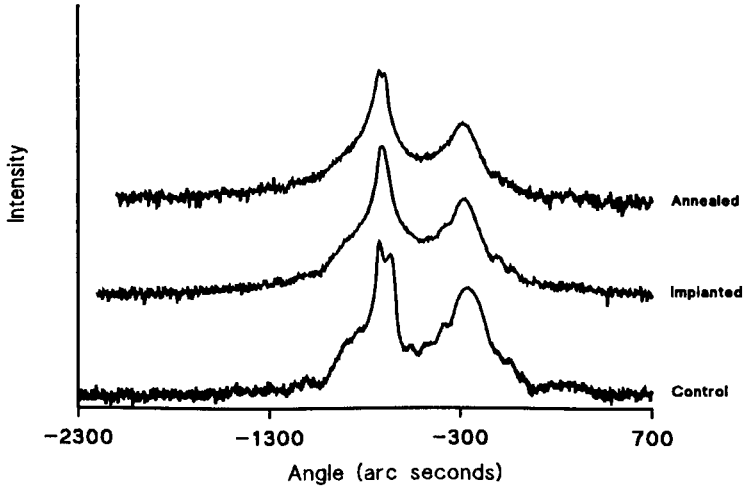

Figure 4.25: DCXRD rocking curves of the control, implanted, and annealed sample 490N at a fluence of 50 mJ cm^{-2}.

Figure 4.26 shows that emission from the first quantum well (emission B) reappears. Emission from the second quantum well is increased but both emissions are observed at intensities lower than those observed from the control sample. Emission A is slightly shifted to lower energies after annealing.

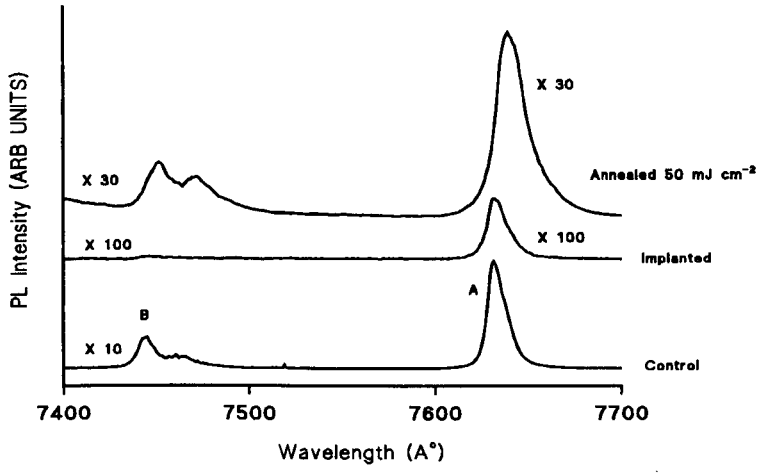

Figure 4.26: The PL spectra of the control, implanted, and annealed sample 490N at a fluence of 50 mJ cm^{-2}, all magnified peaks are referenced to peak A.

Two sections of sample 491 were studied also, sample 491G and sample 491H. Sample 491G was implanted at an ion dose of $4x10^{+13}$ ions/cm^2 and ion energy of 26.2 keV. The sample was then annealed at different fluences of 40, 50, 60, 70, 80 mJ cm^{-2} progressively. The PL spectra of sample 491G before implantation (control), after implantation, and after annealing are shown in figure 4.27.

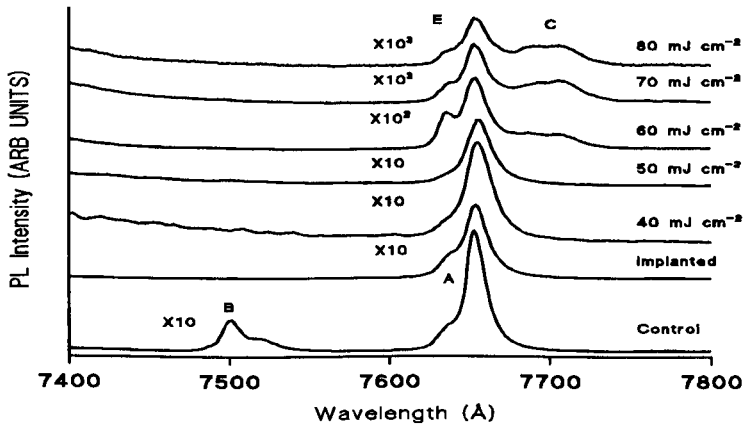

Figure 4.27: The PL spectra of the control, implanted, and annealed sample 491G at fluences of 40, 50, 60, 70, 80 mJ cm^{-2}. All magnified peaks are referenced to peak A.

Two emissions are observed from the control sample in figure 4.27, emission A and B which are assigned to emission from the 80 Å quantum well and from the 40 Å quantum well layer respectively. After implantation, emission A decreases by a factor of 10 and emission B disappears, which is due to the large disorder created by implantation. No major changes occur after laser annealing at fluences of 40 and 50 mJ

cm^{-2}. At a laser fluence of 60 mJ cm^{-2} emission A is broadened with the appearance of a small peak on the high energy tail of the emission (emission E). Also a very broad peak at the right side of emission A at 7710 Å is seen (emission C). At higher fluences 70 and 80 mJ cm^{-2}, progressive weakening of emissions A and E takes place while a little increase in emission C occurs. Again there is no sign of emission B.

To have a better explanation of what is happening after the PLA process in the DQW samples, sample 491H was annealed without any prior implantation at different laser fluences. The idea is to study the behaviour of a DQW structure when it is subject only to pulsed laser beams. Figure 4.28 shows the PL spectra of the control and annealed sample 491 at different laser fluences 30, 50, 60, 70 and 80 mJ cm^{-2}. At a laser

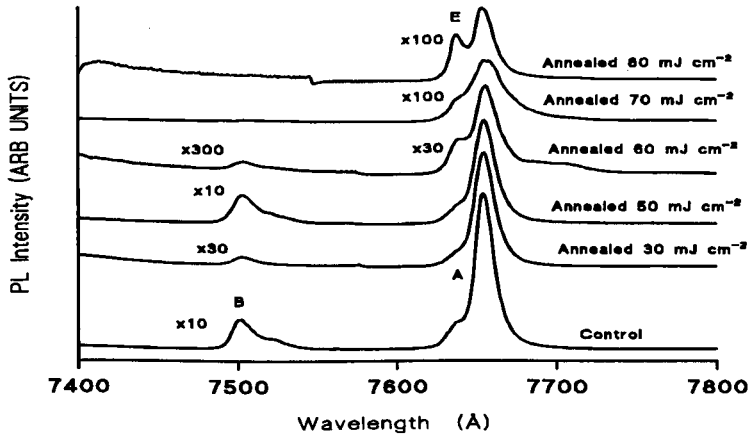

Figure 4.28: The PL spectra of the control, and annealed sample 491H at different laser fluences 30, 50, 60, 70 and 80 mJ cm^{-2}. All magnified peaks are referenced to peak A.

fluence of 30 mJ cm^{-2}, a decrease in intensity of emission B of about 6 is observed while the intensity of emission A remains the same. Further annealing at a fluence of 50 mJ cm^{-2} has introduced a total recovery of emission B while no changes were observed of emission A. At a higher laser fluence of 60 mJ cm^{-2}, the intensity of both QW emissions decreases with emission A being broadened and a small peak E appearing on the high energy tail of emission A at 7640 Å. Annealing at fluences of 70 and 80 mJ cm^{-2} causes even more quenching and broadening of the PL emissions with the disappearance of emission B and a noticeable increase of intensity of emission E at 7640 Å, figure 4.28

4.8 Discussion

Most of the results in the earlier section confirm that damaging of the DQW structure occurred after the implantation process. Figure 4.20 shows the PL spectra of different sections of sample 490 implanted at different ion doses of $1x10^{+13}$, $4x10^{+13}$ and $6x10^{+13}$ ions/cm^2. The implantation energy was held as 26.2 keV. It is quite clear that increasing the ion dose will increase the damage inside the DQW. This is due to the large number of defects (vacancies and interstitials) created within the DQW layers. It is apparent from the PL spectra that an implantation ion dose of $4x10^{+13}$ ions/cm^2 would

be sufficient for our purpose, where emission from the first QW has completely vanished, which is our interest, and the intensity of the second QW emission is decreased by a factor of 10^{+2}. We assume that a large number of vacancies are created inside the first QW, which in turn form non-radiative centres, therefore the emission from the first QW can no longer be observed. The intensity decrease in the second QW can be attributed to two factors. The first factor is due to the damage created via ion implantation in the second QW itself which introduces non-radiative centres inside the well. Secondly, ion implantation causes damage in the barrier layer between the two wells this damage creates non-radiative centres which cause electrons and holes to recombine in the barrirer layer before they can diffuse into the second QW. At ion implantation dose of $6x10^{+13}$ ions/cm^2 and above, progressive weakening of the PL emissions occur. Furthermore figure 4.9 shows that after the implantation process at energy of 26.2 keV, four vacancies per ion are created inside the first QW. For an ion dose of $4x10^{13}$ ions/cm^2, this gives a values of $16x10^{13}$ vacancies created inside the first QW after implantation, which is apparently large enough to wipe out the emission from the first QW.

It has been established that ion mixing can be represented as a diffusion like process in which the diffusion length, during the mixing, is proportional to $\Phi^{1/2}$, where Φ denotes the ion dose [24]. Furthermore, clear evedence that diffusion in CdTe/ CdMnTe structures is controlled by cation vacancies was reported by I. Karla et al [25]. In order to determine the total amount of diffusion caused by the ion implantation, we adopt here the formula given by I. Karla, et, al [26] which ascribes the mixing parameter in CdTe/ CdMnTe structures as the following:

$$\frac{Dt}{\Phi F_d} = 1.5 \times 10^3 \quad \text{Å}^5/\text{eV} \tag{4.5}$$

where F_d is the energy deposited per ion per unit depth which can be obtained from the Trim calculation. Figure 4.29 shows the energy deposited to recoils at implantation of Ar^{+2} ions with ion energy of 26.2 keV (the Trim code). From figure 4.29 below, a value of 77.7 (eV/ion)/Å was obtained for F_d. Using the above equation (4.5), the Dt value is calculated for different ion doses (1, 4, and $6x10^{13}$ ions/cm^2) also the diffusion length has been evaluated as shown in table 4.2.

Ion Dose (ions/cm^2)	$1x10^{13}$	$4x10^{13}$	$6x10^{13}$
Dt (Å^2)	116.5	466	699
$L_d=2[Dt]^{1/2}$ (Å)	21.6	43.2	52.9

Table 4.2: Dt and diffusion length values calculated as a function of the ion dose.

Figure 4.30 shows the plot of the Dt values taken from table 4.2 against the ion dose and a straight line is obtained. This procedure enabled us, from extrapolation of the straight line, to calculate the Dt values for any ion dose in the CdTe/CdMnTe structure.

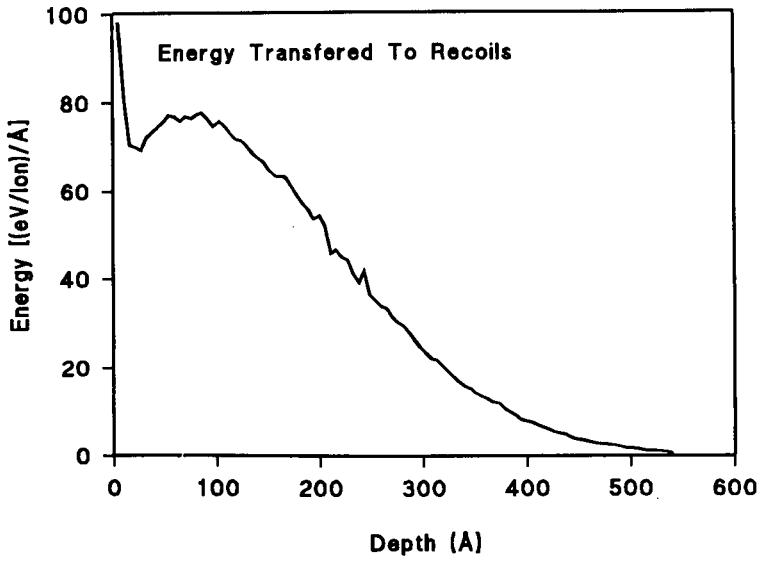

Figure 4.29: Energy deposited to recoils at implantation of Ar^{+2} ions at ion energy of 26.2 keV.

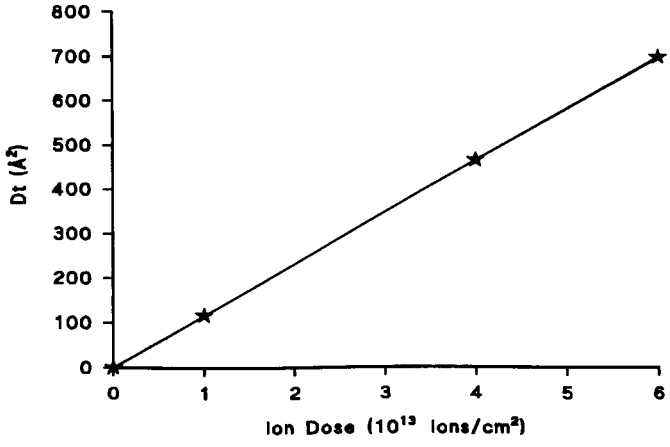

Figure 4.30: Plot of Dt in ($Å^2$) against the ion dose (10^{+13} ions/cm^2).

The annealing process was carried out upon the implanted samples in order to anneal out the damage caused by the ion bombardment. Unfortunately, DCXRD rocking curves were unable to provide any detail of the processes and mechanisms occurring after the ion implantation, whereas photoluminescence spectroscopy was the main technique used to study, in detail, the processes happening after each stage (implantation and annealing). Our major interest is to achieve low-power pulsed laser annealing of implantation damage in the DQW structure without melting the material. In order to do so several samples were implanted and annealed at different laser fluences. We know from the earlier chapter that lattice melting of CdTe occurs at a laser fluence of 75 mJ cm^{-2} therefore our interest will be below this value.

Figure 4.22 shows that annealing of the implanted sample 490Q at a laser fluence of 30 mJ cm^{-2} is not sufficient to anneal out the damage and to restore the optical properties of the quantum wells. Consecutive annealing of the same sample at a higher laser fluence of 50 mJ cm^{-2} led only to increase the second QW emission by a factor of three (i.e. comparing the implanted and annealed samples emissions). No emission from the first QW is observed yet at this point. The x-ray rocking curve of the annealed sample at a fluence of 50 mJ cm^{-2} shows a little increase in the DQW satellite peaks but the peaks are still smaller than those observed from the control sample.

Annealing of sample 490M at a fluence of 40 mJ cm^{-2} after the implantation stage induced even more weakening of emission A without any restoration of emission B as seen in figure 4.24. The x-ray rocking curve also emphasises that there is no restoration of the damage, with no increase in the satellites peaks seen, figure 4.23.

Sample 490N was annealed only at a fluence of 50 mJ cm^{-2}. Figure 4.26 indicates that restoration of the first QW emission (emission B) has successfully occurred but emissions A and B are still weaker than those observed from the control sample. The above results clearly show that at only at a specific laser fluence of 50 mJ cm^{-2} an energy window exists allowing the first QW emission to be partially restored.

To investigate the effect of high pulsed laser fluences on the implanted DQW structure, sample 491G was annealed at laser fluences of 40, 50, 60, 70, and 80 mJ cm^{-2}, figure 4.27. This annealing was also unsuccessful in recovering the first QW emission but at higher laser fluences peculiar changes start to appear around the second QW emission represented by broad peaks E and C at the shorter and longer wavelength tails respectively of emission A. At the higher laser fluences i.e, 60, 70 and 80 mJ cm^{-2}, progressive weakening of the second QW emission takes place. This indicates clearly that at higher laser fluences, a new kind of disorder is introduced to the DQW structure [27,28].

The main question we still need to answer here is, why is the first QW emission restored in sample 490N, but not from sample 490Q, bearing in mind that both samples were implanted with the same dose and annealed at the same laser fluence, 50 mJ cm^{-2} although 490Q was also annealed at 40 mJ cm^{-2}. At this point, and in order to have a better idea of what is happening inside the DQW structure after the annealing process, sample 491H was annealed at laser fluences of 30, 50, 60, 70, and 80 mJ cm^{-2} without any prior implantation. Figure 4.28 indicates that defects themselves are introducted at a laser fluence of 30 mJ cm^{-2} as the intensity of the first QW emission is decreased approximately by a factor of ten. Further annealing at a fluence of 50 mJ cm^{-2} yields a complete recovery of the first QW emission. This can be explained if a small number of defects are created by the 30 mJ cm^{-2} fluence, but a higher fluence of 50 mJ cm^{-2} would be sufficient to anneal out the damage and to restore the optical properties. The decrease of the PL emissions and the virtual disappearance of the first QW emission at higher fluences 60, 70, and 80 mJ cm^{-2} is a clear indication of defect creation in the DQW structure. The above results confirm again that at a laser fluence of 50 mJ cm^{-2} an energy window exists at which LPPLA can be obtained. If exceeded the laser pulse energy causes a new kind of structure disordering [27,28] which leads to the disappearance of the first QW emission. This in turn suggests that the same process occurred in sample 490Q. However this sample was first implanted and then annealed at 30 mJ cm^{-2} so that further annealing at a fluence of 50 mJ cm^{-2} would not be sufficient

enough to anneal the damage caused by both processes i.e., implantation and laser annealing.

In chapter 3 of the thesis the calculations show that surface melting in CdTe/CdMnTe structures occurs at a laser fluence of 75 mJ cm^{-2}. Therefore we expect that at a laser fluence of 75 mJ cm^{-2} and above, melting at the surface of the DQW structure will take place. The melt depth of the surface increases with the laser fluence and this is what changes the PL spectra when the laser fluence is increased, figures 4.27 and 4.28. Since the first quantum well is very close to the surface, only 200 Å, we assume that at a laser fluence of 80 mJ cm^{-2} the first QW has completely melted. Subsequent recrystallisation of the molten layer occurs in which a homogeneous layer of CdMnTe is created, and the top CdTe QW is lost [29]. In order to calculate the diffusion coefficient in the DQW structure, a simple heat diffusion model, explained in detail in chapter 3, is used. This model assumes that the laser pulse is absorbed entirely at the surface of the sample and produces heating of the DQW structure by thermal diffusion which in turn causes the diffusion of Mn ions from the barriers into the QWs. The model further assumes that no heat is lost to the surrounding ambient, by either conduction to the gas or by radiation (chapter 3, section 3.8.1). The temperature at which the surface temperature just reaches the equilibrium melting point of CdTe is about 1090 ^{0}C with a laser fluence of 75 mJ cm^{-2}. Our interest is below this temperature to perform LPPLA of the DQW implanted sample. Figure 4.31 shows the temperature-time-diffusion coefficient curves of the DQW structure (sample 491H). These calculations have been taken at the centre of both QWs for laser fluences of 30, 50, 70 mJ cm^{-2} respectively. The diffusion length calculated at 30 mJ cm^{-2} (table 4.3) for the

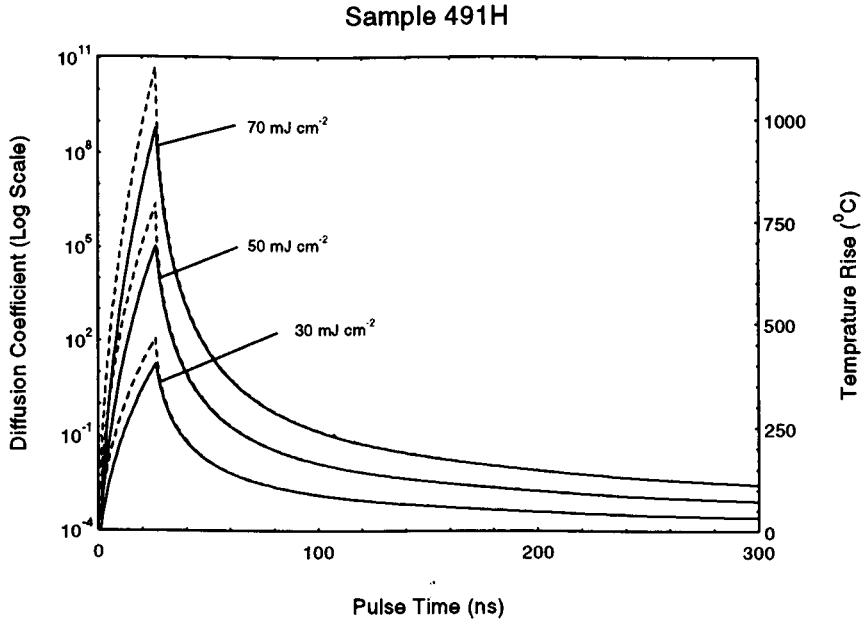

Figure 4.31: Temperature-Time-Diffusion Coefficient curves of the DQW structure (sample 491H) calculated at the centre of both QWs for laser fluences of 30, 50, 70 mJ cm^{-2}. Solid lines represent the 80 Å CdTe quantum well and dashed lines represent the 40 Å CdTe quantum well.

	30 mJ cm^{-2}		50 mJ cm^{-2}		70 mJ cm^{-2}	
	1st QW	2nd QW	1st QW	2nd QW	1st QW	2nd QW
Temperature (^{0}C)	480	420	800	700	1120	979
Dt (Å^2)	$5x10^{-7}$	$9x10^{-8}$	$7x10^{-3}$	$3x10^{-4}$	106	1.5
L_d (Å)	$1.5x10^{-3}$	$6x10^{-4}$	0.17	$3.5x10^{-2}$	21	2.5

Table 4.3: Calculated temperature, Dt and diffusion length values for the first and second QWs at 30, 50, and 70 mJ cm^{-2} laser fluences. Calculations were taken at the centre of both Qws.

first QW is much smaller than the lattice spacing of the CdTe layer. This suggests that there is a diffusion mechanism other than the diffusion of Mn from the barrier into the QW which introduces a small amount of vacancies within the first QW (sample 491H). We assume that at a fluence of 30 mJ cm^{-2} atoms hope out from their native lattice sites but they do not diffuse far from their empty lattice sites depending at the temperature deliverd by the laser pulse. However at a fluence of 50 mJ cm^{-2} we suggest that the total number of atoms hopping back to their lattice sites are more than those hopping out therefore the small disorder created at a laser fluence of 30 mJ cm^{-2} can be removed and emission from the first QW can be totally restored, figure 4.28. At higher laser fluences, where high temperatures are generated, atoms diffuse far distances away from their lattice sites and they become unable to return to their native lattice sites. The mechanism responsible for this effect is very difficult to investigate and requires a vast amount of work.

4.9 Conclusion

To summarize our results, defect introduction (vacancies and interstitials) was observed after the implantation of Ar^{+2} ions. Increasing the implantation dose led to an increase of the disorder of the DQWs. This results in the disappearance of the first QW emission and quenching of the second QW emission. The implantation-induced disorder can be annealed in a low-energy mode. In other words there appears to be an energy window at 50 mJ cm^{-2}, with the upper limit below the melting threshold, in which the crystallinity of the structure, can be restored. Increasing the laser pulse energy above this limit induce a new kind of structural disorder in the irradiated sample where the crystalline channels can be destroyed and the material can finally be melted. We call this a disannealing effect.

References

[1] G. A. Kachurin, N. B. Pridachin, and L. S. Smirnov, Sov. Phys. Semicond. 9, 946 (1976).

[2] *Laser Annealing of Semiconductors*, edited by J.M.Poate, and J.W.Mayer, Academic Press, INC, New York (1982).

[3] J. Narayan, R. T. Young, and C. W. White, J. Appl. Phys. 49, 3912 (1978).

[4] A. Gat, and J. F. Gibbons, Appl. Phys. Lett. 32, 143 (1978).

[5] *"The TRIM computer program"* (1989). Version 5.4, J. F. Zeigler, J. B. Biersack, and G. Cuomo.

[6] P. J. Poole, P. G. Piva, G. C. Aers, A. P. Roth, M. Dion, Z. R. Wasilewski, Emil. S. Koteles, S. Charbonneau, and J. Beauvais. Semicond. Sci. Technol. 9, 2134 (1994).

[7] J. Ralston, A. L. Moretti, R. K. Jain, and F. A. Chambers, Appl. phys. Lett. 50, 25, 1817 (1987).

[8] W. P. Gillin, A. C. Kimber, D. J. Dunstan, and R. P. Webb, J. Appl. Phys. 76, 6, 3367 (1994).

[9] I. Karla, Msc. Thesis, Hull University (1994).

[10] *Ion Implantation and Beam Processing*, edited by J. S. Williams, and J. M. Poate, Academic Press, Sidney (1984).

[11] *Ion Implantation of Semiconductors*, edited by G. Carter, and W. A. Grant, Edward Arnold Publishers Ltd, London (1976).

[12] *The Stopping and Ranges of Ions in Matter*, Volume 1, edited by J. F. Ziegler, J. P. Biersack, and U. Littmark, Pergamon Press, New York (1989).

[13] K. H. Lee, H. H. Park, and D. A. Stevenson, J. Appl. Phys, 65, 3, 1048 (1989).

[14] R. F. Wood, C. W. White, and R. T. Young, Semiconductors and Semimetals, Vol 23, Pulsed Laser Processing of Semiconductors, Academic Press Inc, London (1984).

[15] E. S. Koteles, B. Elman, R. P. Holmstrom, and P. Melman, Superlattices and Microstructures, Vol 5, No. 3, 321 (1989).

[16] N. Can, P. D. Townsend, D. E. Hole, and H. V. Snelling, J. Appl. Phys. 78, 11, 6737 (1995).

[17] S. Y. Chou, Y. Chang, K. H. Weiner, T. W. Sigmon, and J. D. Parsons, Appl. Phys. Lett. 56, 6, 530 (1990).

[18] C. T. Foxon, J. A. Harvey, and B. A. Ioyce, J. Phys. Chem. Solids 34, 1693 (1973).

[19] S. S. Kular, B. J. Sealy, K. G. Stephens, D. R. Chich, Q. V. Davis, and I. Edwards, Electron. Lett. .14, 85 (1978).

[20] G. Vitali, M. Bertolotti, G. Foti, and E. Rimini, Phys. Lett. A63, 351 (1977).

[21] G. Vitali, M. Rossi, D. Karpuzov, H. Budinov, and M. Kalitzova, J. Appl. Phys. 69, 3882 (1991).

[22] N. C. Kerr, and D. C. Emmony, J. Mod. Opt. 37, 787 (1990).

[23] J. H. C. Hogg, J. E. Nicholls, S. R. Jackson and W. E. Hagston; Material Science and Engineering B16, pp.60-63 (1993)

[24] G. Gladyszewski and A. Smal, Nucl. Instrum. Methods Phys. Res. B 62, 541 (1992).

[25] I. Karla, D. Shaw, W. E. Hagston, J. H. C. Hogg, S. Chalk, J. E. Nicholls, and C. Peili, J. Appl. Phys. 79, 4 pp.1895-1897 (1996).

[26] I. Karla, J. H. C. Hogg, W. E. Hagston, J. Fatah, and D. Shaw, J. Appl. Phys. 79, 4 pp.1898-1902 (1996).

[27] G. Vitali, Jpn. J. Appl. Phys. Vol 31, 2049-2055 (1992).

[28] G. Vitali, L. Palumbo, M. Rossi, G. Zollo, and C. Pizzuto, Phys. Rev. Vol 53, pp. 4757-4769 (1996).

[29] D. Sands, J. E. Nicholls, J. H. C. Hogg, S. Chalk, F. X. Wagner, W. E. Hagston, M. O'Neill, B. Lunn, and D. E. Ashenford, J. Crystal. Growth. 184/185 (1998) 114-118.

Chapter 5

Laser Emission from ZnS/ $Zn_{1-x}Cd_xS$ Quantum Well Structures

5.1 Introduction

The progress of reliable blue/green lasers is now a realistic goal of present research. Sony has demonstrated a diode with a life time in excess of 100 hours at room temperature [1]. Nevertheless, there are several applications where shorter wavelengths would afford further advantages, but the problems yet to be solved remain formidable. To extend the current ZnSe technology to shorter wavelengths, the use of a wider band gap semiconductors such as ZnS and MgS is required. Unluckily the question of P-doping of ZnS and MgS still needs to be answered. Doping levels in ZnSe can successfully be performed up to 10^{18} /cm^3 but this value drops immediately below 10^{17} /cm^3 when the alloy band gap is greater than 3.00 eV [2]. Laser emission at a wavelength of 385 nm has been attained from GaAlN/GaN [3] but the band gap restrains the shortest wavelength possible to about 375 nm at room temperature. Strong near-UV stimulated emission was observed at room temperature in GaN/AlGaN separate confinement heterostructures (SCH) grown by molecular beam epitaxy (MBE) on sapphire substrates [4]. Furthermore laser emission near 363 nm was observed at room temperature from an optically pumped GaN/AlGaN vertical cavity surface emitting laser [5]. In 1997 stimulated emission at 357 nm from an optically pumped GaN/AlGaN double heterostructure grown by vapor-phase deposition was reported [6]. The threshold excitation density at 77 K was similar to 40 kW/cm^2. One year later, Domen et al [7] reported that the lasing mechanism of an InGaN/GaN/AlGaN is dominated by free carriers. The fabrication of GaN/InGaN/AlGaN double heterostructure light emitting diodes (DH LEDs) covering the 385-430 nm spectral range was reported by Schlotter el al [8]. In 1999, Wu et al [9] reported that stimulated emission at a wavelength of 394 nm was observed from the cleaved edge of the optically pumped cubic GaN/AlGaN heterostructures at 15 K. Furthermore, photopumped room temperature surface-mode lasing at 401 nm in InGaN/GaN/AlGaN vertical-cavity surface-emitting laser grown on sapphire substrates using metal-organic vapor-phase epitaxy was reported [10]. In 1999, Lebedev et al [11] reported for the

first time an InGaN/GaN multiple quantum well (MQW) in-plane laser pumped by surface normal pulse and scanning electron beams. He found that pumping at room temperature (RT) and 80 K showed peak stimulated emission wavelengths of 402 and 409 nm with a full width half maximum (FWHM) of 0.6 nm and 1.2 nm, respectively. Optically pumped stimulated emission (SE) from InGaN/GaN multiple quantum wells (MQWs) grown by metalorganic chemical vapor deposition was reported by Schmidt et al [12]. He observed two distinct SE peaks at 425 nm at 10 K (430 nm at 300 K) and at 433 nm at 10 K (438 nm at 300 K). InGaN/GaN/AlGaN quantum-well-structure blue LEDs grown on epitaxially laterally overgrown GaN (ELOG) and sapphire substrates were reported by Nakamura et al [13]. The output power of both LEDs was as high as 6 mW at a current of 20 mA and the longest lifetime of 9800 hours at a constant output power of 2 mW was achieved. In 1995 Akasaki et al [14] reported, for the first time, stimulated-emission by current injection from an AlGaN/GaN/GaInN quantum-well device. Also room-temperature pulsed operation of an electrically injected InGaN/GaN multi-quantum well distribution feedback laser with an emission wavelength of 403 nm was reported by Hofstetter et al [15]. Optically pumped lasing at room temperature between 360 and 380 nm from simple slab waveguide ZnCdS/ZnS QW structures with cleaved facets have been achieved in this laboratory [16]. The threshold power densities obtained were between 150 and 200 kW cm^{-2}. Furthermore, optically pumped lasing at the shortest wavelength yet achieved in semiconductors was demonstrated at 333 nm, at temperatures up to 80 K [17]. These results were obtained following the success in developing the growth of ZnS with a sulfur cracker source on GaP substrates. In order to avoid the inherent problems implicated in p-type doping of ZnS and its alloys, the idea of developing an e-beam pumped near-UV laser based on ZnCdS/ZnS structures grown on (001) GaP was introduced. This objective was established after the fine success of achieving optically pumped laser emission from ZnCdS/ZnS structures [16,17]. The choice of ZnS may be advantageous in respect of the operating lifetime of the laser. In ZnSe laser diodes, it is assumed that the lifetime is limited by the propagation, with time, of existing defects from the II-VI/III-V interface through the active region due to the relative weak bond strength of the material [18,19,20]. Degradation of laser output with time was also observed in e-beam pumped CdTe GRINSCH structures (Graded Index Separate Confinement Heterostructures), and ascribed to the same mechanism mentioned above [21]. However, ZnS is a considerably harder and more robust material than both CdTe and ZnSe, therefore degradation of performance by this mechanism may be diminished.

E-beam pumping of semiconductor laser diodes, especially II-VI compounds, was investigated many years ago, but the requirement for high beam currents (typically 50 A cm^{-2}) and high voltages (typically 40 kV) have impeded the manufacture of a compact practical laser device. Compact (2 cm^3) micro-gun pumped lasers in the blue and red regions were lately established from ZnSe and CdTe based laser structures respectively [22,23]. These devices use a micro-tip electron gun with a cold cathode and simple e-beam optics to pump the laser. In fact, the penetration depth of the e-beam is quite low (about 100-500 nm), therefore a graded band gap was used to provide an effective way of collecting the electrons and holes into the QW region. Subsequently, GRINSCH lasers with low accelerating voltages (about 5-10 kV) and low currents (less than 500 μA) injection were demonstrated [22,23].

In the present chapter optically pumped stimulated emission experiments were carried out on a series of ZnS/ZnCdS single quantum well structures (SQWs) grown on GaP substrates by the MBE technique. The aim of this work was to produce laser emission in the ultraviolet spectral region at room temperature from ZnS/ZnCdS SQW structures in order to achieve blue and UV laser diodes. Photoluminescence spectroscopy and DCXRD were used to monitor the sample quality, Cd concentrations in the ZnCdS quantum wells, and strains in the samples in question. The stimulated emission experiments were performed at temperatures from 6K up to 280 K. Laser thresholds and gain measurements were carried out at different temperatures. Also electron beam pumping experiments were utilized for the sake of producing electron beam pumped stimulated emission.

5.2 Quantum Well Lasers

5.2.1 The Interest In Quantum Well Lasers

The technology of semiconductor lasers has progressed very rapidly over the last two decades. This rapid progress was directed towards the development of quantum well lasers. Quantum well technology allows the crystal growers a precise control of the range, depth, and arrangement of quantum mechanical potential wells. This control can be used to produce very good lasers. At the 12th International Semiconductor Laser Conference, held in Davos, Switzerland, more than half the conference papers were related to quantum well lasers [24]. This increasing reputation is due to the fact that quantum well lasers are rather better than conventional lasers with bulk active layers. One distinct advantage is the capability to alter the lasing wavelength solely by modifying the width of the quantum well. Another essential advantage is that the quantum well laser delivers more gain per injected carrier than conventional lasers, thus lower threshold currents can be obtained. Due to injected carriers being responsible for internal losses, quantum well lasers, which necessitate less injected carriers, are more efficient and can produce more power than conventional lasers. Furthermore, quantum well lasers deliver gain with less variation in refractive index than bulk lasers, resulting in lower chirp. Quantum well lasers have also narrower linewidths than conventional lasers because of the lower internal losses and the lower refractive index changes. The splitting of the heavy and light hole valence bands by spatial quantization and the capacity of growing quantum wells with compressive and tensile strain lead to a much better control over the optical polarisation than in bulk lasers. The differential gain (gain per injected electron) is greater in well designed multi-quantum well lasers which results in higher speed than for bulk lasers.

5.2.2 The first Observation of Quantum Well Lasers

Current semiconductor lasers incorporate a heterostructure in which the active region is surrounded by higher bandgap material. The heterostructure laser concept was suggested in 1963 by H. Kroemer [25] in the U.S. and by R. F. Kazarinov and Zh. I. Alferov [26] in the former Soviet Union. In 1967, GaAs and AlGaAs heterostructurs were successfully grown by liquid phase epitaxy by J. M. Woodall et al. [27] of IBM. Later, semiconductor lasers were reported by Alferov's group, H. Kressel, and H.

Nelso of RCA and I. Hayashi and M. B. Panish at Bell Laboratories [28]. By 1970, double heterostructure lasers continuously operating at room temperature were established by Alferov's group [29] and Hayashi and Panish [30].

The first observation of quantum well laser operation was made in 1975 by J. P. Van der Ziel et al [31], using GaAs/AlGaAs multilayer structures grown by MBE. They optically pumped the material at a temperature of 15 K and achieved a threshold of 36 kW/cm^2. One year later Miller et al [32] reported optically pumped laser experiments at room temperature from very thin GaAs/AlGaAs multilayer structures and conventional double heterostructures. A new method of crystal growth was developed at that time called metalorganic chemical vapour deposition (MOCVD). This method was first used by R. D. Dupuis and P. D. Dapkus of Rockwell International in 1977 to make AlGaAs heterostructure lasers [33]. At the same time, Dupuis and Dapkus in collaboration with N. Holonyak and co-workers at the university of Illinois utilized the MOCVD technique in order to produce enhanced quantum well lasers. In 1977, these authors reported the first demonstration of a quantum well injection laser [34]. The authors quoted that the laser threshold could be improved by extra layers for separately confining the optical field.

The demonstration of cw operation of SQW and MQW injection lasers was first announced in 1978 by the same authors. Meanwhile, the growth of lasers by MBE progressively improved and the first cw injection laser designed by MBE was attained by Cho et al in 1975 [35]. In 1979, Tsang et al [36] reported MBE-growth AlGaAs injection lasers containing 14 quantum wells, 139 Å wide, with a room temperature threshold of 2 kA/cm^2. They reached the final conclusion that the AlGaAs interfaces were basically free of the nonradiative defects that had troubled earlier attempts to produce low threshold quantum well lasers by MBE. Tsang found that the high thresholds of MQW lasers were caused by the inefficiency in injecting carriers over the barriers existing between wells. In 1981 [37], he optimized barrier heights and thicknesses and utilized larger Al content in the outer layers in order to achieve separate confinement of the optical energy. Meanwhile SQW lasers were reported by Tsang in 1981 [38]. Tsang was the first to introduce the graded index waveguide for separate optical confinement (GRINSCH) design. These two exciting papers by Tsang illustrated the advantage of quantum well lasers over conventional bulk active layer lasers in obtaining low laser threshold.

5.2.3 Review of Work on ZnS/ZnCdS Quantum Well Lasers

There have been many problems in achieving blue-green lasers as the low band gap of III-V compounds prevented this range of the spectrum from being accessed. Consequently interest developed in GaN and ZnSe/ZnSSe because of their wide bandgap. Both compounds have been used in order to push the emission wavelength into the near UV. As well as these compounds much progress has recently been achieved in the application of the wide bandgap II-VI compound semiconductors heterostrctures based on ZnSe/ZnCdSe quantum wells for injection laser diodes [39,40] and display devices [41,42], also operating in the blue green region of the spectrum. A large amount of work has been carried out also on optically pumped laser operation in a variety of wide bandgap II-VI multiple quantum well (MQW) structures and double heterostructures such as ZnSe/ZnMnSe [43], CdZnSe/ZnSSe [44], CdZnSe/CdZnSSe

[45], ZnSe/ZnSSe [46,47], and CdZnTe/ZnTe [48]. Among wide bandgap II-VI compound semiconductors with the zincblende structure, ZnS has the largest bandgap energy and exciton binding energy [see table 5.1], whilst CdZnS-based quantum well structures exhibit fundamental absorption edges which can be varied from the green to the near UV [49]. These SLs were grown, for the first time, by Endoh and Taguchi [50] employing low-pressure metal organic chemical vapour deposition (MOCVD) in 1989. Stimulated emission in optically pumped CdZnS/ZnS SLs at 10 K or at room temperature with the utilization of resonant excitation of the exciton absorption line had been achieved previously [51,52], which leads to the possibility of manufacturing an ultraviolet laser diodes. Furthermore, it is found that the optical gain mechanism in II-VI multiple quantum well (MQW) structures differs from that observed in III-V systems where an electron-hole plasma (EHP) plays a prominent part in providing optical gain [51,52]. Evidence of exciton lasing in optically pumped II-VI QWs [52,53] shows the possibility of exciton-related stimulated emission processes. In 1993 Taguchi et al [54] evaluated the band offset in ZnS/ZnCdS strained-layer quantum well structures. He found large values of approximately 180-260 meV in the conduction band offset for Cd concentrations of x=0.2-0.3.

	CdS	ZnS
Lattice constant a (Å)	5.832	5.4093
Elastic constants C_{11} (Mbar) C_{12} (Mbar)	0.78 0.53	1.067 0.666
Deformation potential constants a_c--a_v (eV) a_c (eV) a_v (eV) b (eV)	 -3.10 -2.08 1.02 -4.7	 -4.00 -2.78 1.22 -0.7
Band-gap energy E_b (eV)	2.56 (4.2 K) 2.36 (300 K)	3.84 (4.2 K) 3.67 (300 K)
Spin-orbital splitting energy Δ_{so} (eV)	0.07	0.072
Exciton binding energy E_B^{1s} (meV)	27	40
Offset of the CdS valence band at zero strain with respect to ZnS ΔE_v^0 (eV)	0.28	----------

Table 5.1: Physical parameters of ZnS and CdS materials [54].

The first observation of ultraviolet stimulated emission from $Zn_{1-x}Cd_xS/ZnS$ strained-layer multiple quantum wells (MQWs) under both optical pumping at room temperature and pulsed current injection at 30 K was carried out by Yamada et al in 1994 [55]. Two years later the demonstration for stimulated emission at 300 K from ZnS/ZnCdS quantum well structures grown by MBE on (100) GaP substrate was achieved [16]. GaP is thought to be a better substrate material since the lattice constant of ZnS (5.4093 Å) is closer to that of GaP (5.4505 Å) than that of GaAs (5.6533 Å). In that sense, the misfit dislocations and the strain due to the lattice mismatch should be less. They found that in quantum well structures with the lowest Cd-composition optically pumped lasing at wavelength as low as 333 nm at 8 K. They reached the conclusion that while lasing is excitonic at low thresholds, an electron-hole plasma (EHP) transition is possible if the pump power approaches 100 kW/cm^2 [16].

5.3 Laser Threshold and Optical Gain in II-VI Quantum Well Structures

It has been found that the mechanism in which stimulated emission in a II-VI quantum well structure is produced varies greatly from the gain mechanism observed in III-V semiconductor lasers. Optical gain in III-V devices originates from a population inversion which is produced by injecting a degenerate electron-hole plasma into the active region of the device. Furthermore, it is found that excitons do not contribute in any way to the lasing mechanism in III-V materials. Therefore at thresholds and above, only band-to-band transitions are significant.

In II-VI heterostructures there is a strong indication that stimulated emission is controlled by excitonic processes, which is expected mostly due to the larger binding energy, smaller Bohr radii r_B and shorter exciton lifetime in II-VI compounds. The exciton screening density is expected to be inversely proportional to r_B^3 , hence screening effects are less important in II-VI materials [56].

In quantum well structures, quasi-2D confinement of electron-hole pairs increases the exciton binding energy (E_X), and enhances the oscillator strength. The confinement can increase the exciton binding energy so that it exceeds the LO-phonon energy ($h\omega_{LO}$) in the material at issue, satisfying the condition:

$$E_X > h\omega_{LO} \tag{5.1}$$

It is possible also that the exciton binding energy may even exceed kT at room temperature:

$$E_X > kT \tag{5.2}$$

This results in a reduction in exciton-LO-phonon coupling which in turn leads to strong sharply defined exciton features in the spectra of II-VI quantum well structures, even at room temperature, whereas in bulk materials or in III-V compounds excitonic features are hardly observed above cryogenic temperatures (i.e. >100K). The LO-phonon energies in III-V materials are so large that, even with quantum confinement, they cannot be exceeded by the exciton binding energy, therefore interactions between

excitons and LO-phonons act to dissociate excitons into a free electron-hole pair continuum, resulting in a lack of excitonic features above cryogenic temperatures.
When laser activity starts in II-VI heterostructures the electron-hole population is strongly influenced by excitonic effects.

In a QW the density of states is a step-like function of energy, see figure 1.8, given by:

$$\rho(E)dE = \frac{1}{2\pi}\left(\frac{2m_r}{\hbar^2}\right)\ \frac{1}{L_z}\sum_{n=1}^{\infty} H(E-E_n)\,dE \tag{5.3}$$

where Lz is the well width and m_r is the reduced effective mass. The term $H(E-E_n)$ is the heaviside function for the quantum state energy E_n, $H(E-E_n)=1$ for $E \geq E_n$ else $H(E-E_n)=0$. The total concentration of electrons in the conduction band (or holes in the valence band) can be written as:

$$n = \int_{E_C}^{\infty} \rho(E) f(E) dE \tag{5.4}$$

where $f(E)$ is the Fermi-Dirac distribution function given by:

$$f(E) = \frac{1}{\exp[(E-E_f)/kT]+1} \tag{5.5}$$

For a given carrier density one can use the above equation to calculate the quasi-Fermi energy in the conduction band and in the valence band.

In a QW we sometimes need to know the sheet carrier density, which is given by:

$$nL_z = \int_{E_C}^{\infty} \rho(E) f(E) L_z\, dE \tag{5.6}$$

For gain calculations, we starts with Fermi's Golden rule which is given by [57]:

$$W = \frac{2\pi}{\hbar}\left|\langle i|H'|j\rangle\right|^2 \rho\left(E_f\right)\delta\left(E-E_i-E_f\right) \tag{5.7}$$

where W is the transition rate (s^{-1}) between initial and final states with energies E_i and E_f respectively, $\langle i|H'|j\rangle$ is the perturbation matrix element arising from the interaction of the vector potential of the electromagnetic field with the electron in the initial state, and $\rho\left(E_f\right)$ is the density of final states. Assuming a sinusoidal electric field, and using standard perturbation theory, the material gain coefficient for a quantum well can be expressed as [58]:

$$g(E)=\frac{q^2|M|^2}{\varepsilon_0 m_0^2 c\hbar\bar{n}}\frac{1}{EL_z}\sum_{ij} m_r C_{ij} A_{ij}\{f_n(E)-[1-f_h(E)]\}H(E-E_{ij}) \tag{5.8}$$

where:
q= electronic charge
ε_0= permittivity of free space
m_0= free electron mass
c= speed of light in vacuum
$\bar{n}$ = effective refractive index
i, j= conduction, valence band quantum numbers at Γ
f_n= Fermi population factor for conduction electrons
f_h= Fermi population factor for valence holes
E_{ij}= transition energy between states i and j

The reduced effective mass is defined as:

$$\frac{1}{m_r}=\frac{1}{m_i}+\frac{1}{m_j} \tag{5.9}$$

Also, $H(E-E_{ij})$ is the heaviside step function for a transition energy between steps i and j and C_{ij} is a spatial overlap factor, which can have values either near unity or near zero, and thus is basically the k-selection rule. A_{ij} is an anisotropy factor included to account for the polarization of the electric field [57, 59]. $|M|^2$ is the bulk momentum matrix element which is defined as:

$$|M|^2=\frac{m_0^2 E_\Gamma(E_\Gamma+\Delta)}{6m_e(E_\Gamma+2\Delta/3)} \tag{5.10}$$

where Δ is the valence band split off energy.

In order to evaluate the gain, the structural properties of a semiconductor laser must be considered. The majority of quantum well lasers have a very small active region (with a thickness of the order of a single quantum well) which is surrounded by thicker layers (of the order of many wavelengths) of material which define the optical waveguiding region. As a result only a small portion of the optical field, confined within the waveguide region, overlaps with the active layer of the QW laser. The gain only accounts to this small portion of the optical field. The real gain of the QW laser is recognized as the modal gain which is defined as the peak material gain of the QW (γ) multiplied by a confinement factor (Γ) which is nearly proportional to the well width L_z. When the gain is equal to the losses we then have the so-called laser threshold. In a semiconductor laser this can be expressed as:

$$\Gamma_\gamma=\alpha+\frac{1}{2L}\ln\frac{1}{R_1R_2} \tag{5.11}$$

where Γ_{th} is the modal gain at threshold, α is the absorption loss within the structure, and R_1 and R_2 are the facet reflectivities, included in order to take into account the light lost through transmission at the end of the facets. The threshold current density , in units of A/cm^2, can then be expressed as [57]:

$$J_{th} = \frac{J_0}{\eta} \exp \frac{\alpha + \frac{1}{L} \ln \frac{1}{R}}{\Gamma \beta J_0} \tag{5.12}$$

where β is a gain coefficient, and η is the quantum efficiency. The quantum efficiency term is introduced to account for any losses which arise independently of the optical processes.

Since the active region in many quantum well lasers are subject to some degree of strain, it is very important to take into consideration the effects of strain on the transparency and gain conditions. In a semiconductor material, the attendance of a biaxial strain causes shifts in the band edges relative to each other. Moreover, strain may cause changes in the values of the effective masses of carriers in the energy bands, for instance, the existence of a compressive biaxial strain causes a decrease in the hole effective mass in the direction parallel to the growth axis. This decrease leads to a reduction in the density of states. This results in a smaller value for the injected carrier density which is required to reach the lasing threshold. Also equation 5.8 predicts that any strain which might exists in the material will have an influence on the gain coefficient. Strain may also causes changes in the effective refractive index and bulk momentum matrix element. Therefore, it is very important to understand the behaviour of a quantum well material when it is subject to biaxial strain in order to evaluate accurately the conditions for transparency and optical gain in that material.

A DOS Quick Basic program was used to calculate the gain in ZnCdS/ZnS QW structures based on the free carrier gain mechanism. For a given ZnCdS/ZnS QW structure the program calculates first the well depths (offsets) in the conduction and valence bands, including strain induced shifts. Then the energy levels of the QW states are calculated for the electrons and holes. For a given carrier density the electron and hole quasi-Fermi energies are then calculated, equations 5.3 to 5.5. The program then calculates the gain as a function of energy for a given carrier density (mainly at the e1hh1 transition energy), equation 5.8.

Figure 5.1 shows the calculated modal gain as a function of the sheet carrier density for $Zn_{0.8}Cd_{0.2}S$/ZnS QWs with well widths of 40, 60, 80 and 120 Å. One can see that narrower wells will have higher gain for the same sheet carrier density. Furthermore, figure 5.2 shows that a single QW is the best solution for low threshold lasing. In multiple QW structures the optical confinement factor (Γ) is multiplied almost by the number of the QWs, so for the same amount of modal gain (Γ_{th}) needed to reach the threshold, the material gain (g) needed may be several times lower. However for a certain amount of excitation density, carriers are distributed among the QWs so the carrier density in each QW is several times lower. Since the gain is a non-linear function of the carrier density, above the transparency carrier density (where g=0), the gain increases very quickly (exponentially) with the carrier density. This is particularly so in ZnCdS/ZnS QWs with large electron and hole effective masses.

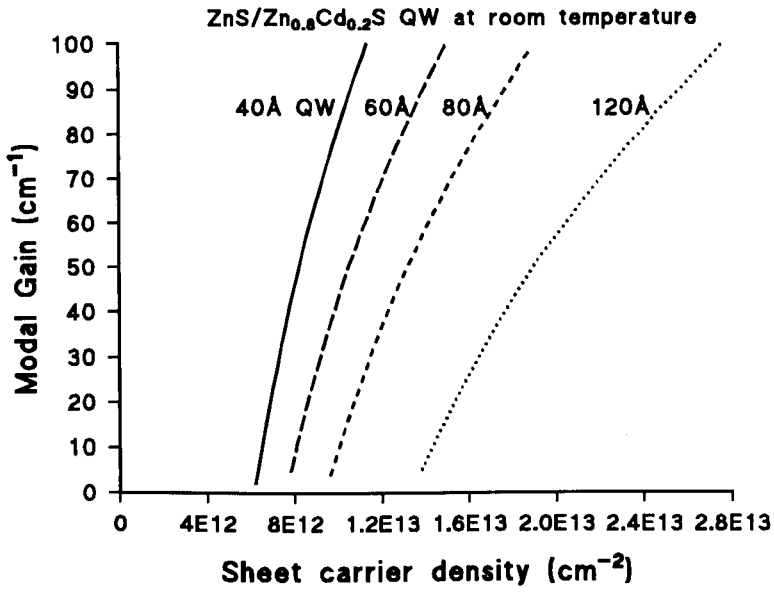

Figure 5.1: Modal gain as a function of sheet carrier density for a single $Zn_{0.8}Cd_{0.2}S/ZnS$ QW with well widths of 40, 60, 80 and 120 Å.

Therefore the smallest excitation density needed to reach the same amount of modal gain is in a single QW structure. Figure 5.2 shows the calculated modal gain as a function of the excitation density for GRINSCH $Zn_{0.8}Cd_{0.2}S/ZnS$ lasers with 1, 2, 3, or 4 QWs. The excitation density is the sum of the sheet carrier densities in each well.

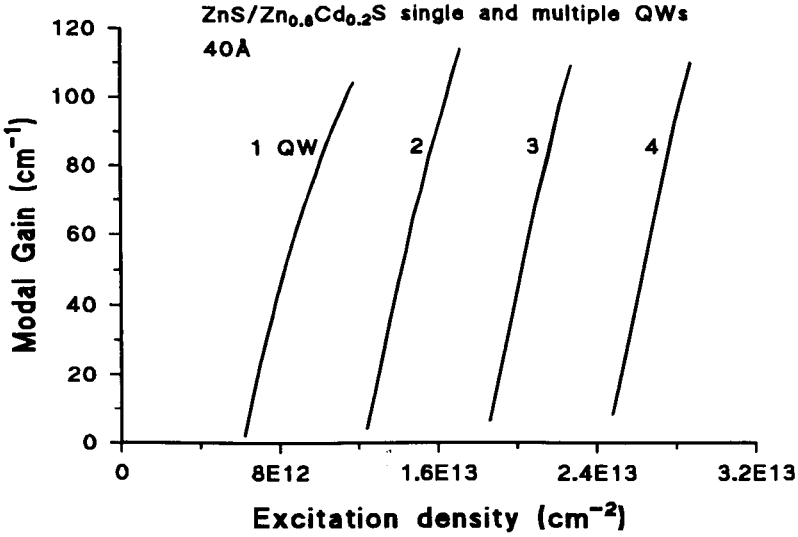

Figure 5.2: Modal gain as a function of excitation density for GRINSCH $Zn_{0.8}Cd_{0.2}S/ZnS$ lasers with 1, 2, 3, or 4 QWs.

Assuming the modal gain at the threshold is the same (anywhere below 100 cm^{-1} for an example), one can see that the excitation density needed is much smaller in the single QW structure.

5.4 Growth Procedure and Samples Details

As a result of the previous calculation three different ZnCdS/ZnS single quantum well structures were studied in the present work. All of them were grown using Molecular Beam Epitaxy (MBE) in the (001) direction on GaP substrate. In all three structures the QW was positioned at the same depth from the surface of the structure. The structure and composition of each sample is given below:

1. Sample S20: ZnCdS / ZnS SQW with reduced barriers (Non-graded SCH structure).

Sample S20 was grown by MBE on a (001) GaP substrate. Its structure is shown below:

1000 Å ZnS / 1000 Å ZnCdS (2%) / 35 Å ZnCdS (20%) / 1000 Å ZnCdS (2%) /
/ 1.5 μm ZnS / GaP (001) : Substrate.

The ZnCdS (2%) buffer layers were approximated by an 18 period superlattice of 50 Å ZnS / 5.5 Å ZnCdS (20%). Figure 5.3 shows a schematic diagram of a non-graded SCH structure (S20).

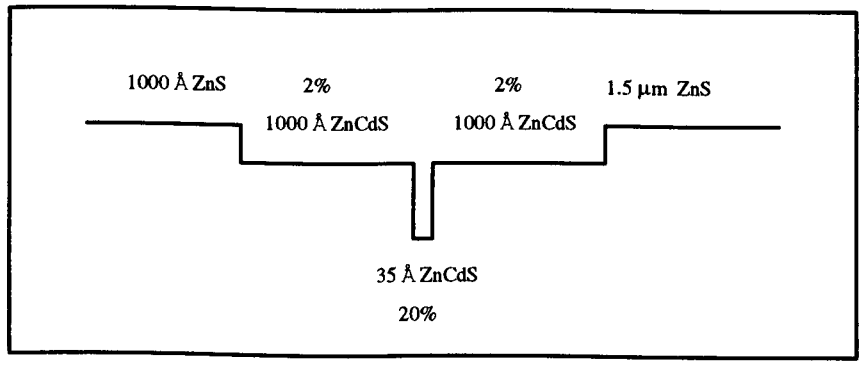

Figure 5.3: A schematic diagram of a non-graded SCH structure (S20).

2. Sample S24: ZnCdS / ZnS SQW with graded barriers (GRIN-SCH structure).

Sample S24 was also grown by MBE on a (001) GaP substrate. Its structure is shown below:

1000 Å ZnS / 1000 Å ZnS-ZnCdS (4%) Graded / 35 Å ZnCdS (20%) /
1000 Å ZnCdS (4%)-ZnS Graded / 1.5 μm ZnS / GaP (001) : Substrate.

A schematic diagram of a GRIN-SCH structure (S24) is illustrated in figure 5.4. Details

of the graded interface are shown in table 5.2.

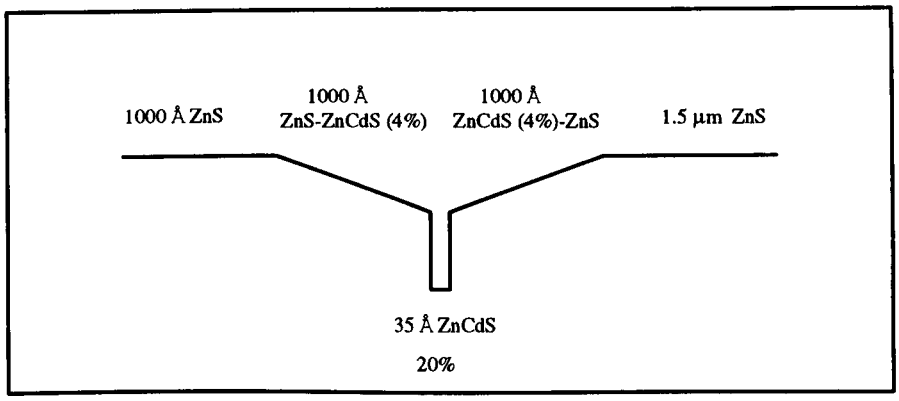

Figure 5.4: A schematic diagram of a GRIN-SCH structure (S24).

319.8 Å ZnS	20.9 Å ZnS	2.09 Å ZnCdS	20.9 Å ZnS	2.09 Å ZnCdS	18.81 Å ZnS
2.09 Å ZnCdS	16.72 Å ZnS	2.09 Å ZnCdS	16.72 Å ZnS	2.09 Å ZnCdS	16.72 Å ZnS
2.09 Å ZnCdS	14.63 Å ZnS	2.09 Å ZnCdS	14.63 Å ZnS	2.09 Å ZnCdS	14.63 Å ZnS
2.09 Å ZnCdS	14.63 Å ZnS	2.09 Å ZnCdS	12.54 Å ZnS	2.09 Å ZnCdS	12.54 Å ZnS
2.09 Å ZnCdS	12.54 Å ZnS	2.09 Å ZnCdS	12.54 Å ZnS	2.09 Å ZnCdS	10.45 Å ZnS
2.09 Å ZnCdS	12.54 Å ZnS	2.09 Å ZnCdS	10.45 Å ZnS	2.09 Å ZnCdS	10.45 Å ZnS
2.09 Å ZnCdS	10.45 Å ZnS	2.09 Å ZnCdS	10.45 Å ZnS	2.09 Å ZnCdS	10.45 Å ZnS
2.09 Å ZnCdS	8.36 Å ZnS	2.09 Å ZnCdS	10.45 Å ZnS	2.09 Å ZnCdS	8.36 Å ZnS
2.09 Å ZnCdS	10.45 Å ZnS	2.09 Å ZnCdS	8.36 Å ZnS	2.09 Å ZnCdS	8.36 Å ZnS
2.09 Å ZnCdS	8.36 Å ZnS	2.09 Å ZnCdS	8.36 Å ZnS	2.09 Å ZnCdS	6.27 Å ZnS

Table 5.2: ZnS-ZnCdS (4%) grading rate [ZnCdS=ZnCdS (20%)].

3. *Sample S26:* ZnCdS / ZnS SQW structure.

The sample structure can be seen below:

1000 Å ZnS / 1000 Å ZnS / 35 Å ZnCdS (20%) / 1000 Å ZnS / 1.5 μm ZnS / GaP (001) : Substrate.

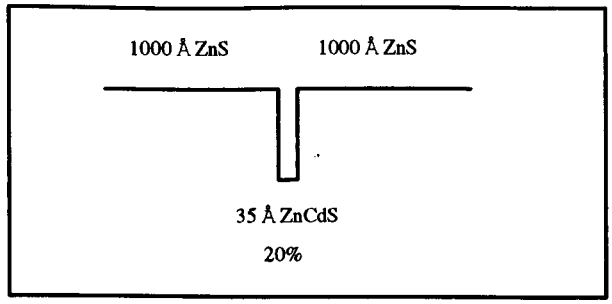

Figure 5.5: A schematic diagram of a SQW structure (S26).

5.5 Experimental Results

The samples, which form the subject of the present work, were studied experimentally by several techniques. Before starting the stimulated emission measurements, photoluminescence spectroscopy and DCXRD techniques were utilized to evaluate the samples quality, determine if possible the Cd concentration in the samples and to select the most adequate samples for the main task, i.e. stimulated emission experiments. The experimental set-up of the techniques already named are explained in detail in chapter 2.

5.5.1 DCXRD Measurements

Double Crystal X-Ray Diffraction measurements were carried out on the ZnS/ZnCdS samples. Figure 5.6 shows the x-ray rocking curves of samples S20, S24, and S26 respectively. The most intense peak at 0 arcsecond is attributed to the thick substrate layer. The broadened peak at the right side of the substrate peak, around 1500 arcseconds, is assigned to the thick ZnS buffer layer. Unfortunately, no satellite peaks of the superlattice layers were detected. We attribute this to the variations in wells thicknesses which in turn act to break the periodicity of the superlattice structure. Further contribution to this could be from lattice strains and dislocations which again act to distort the periodicity of the structure.

All that can be deduced from the x-ray rocking curves is the relaxation of the buffer layer which is estimated, from the RADS simulation, as 90%.

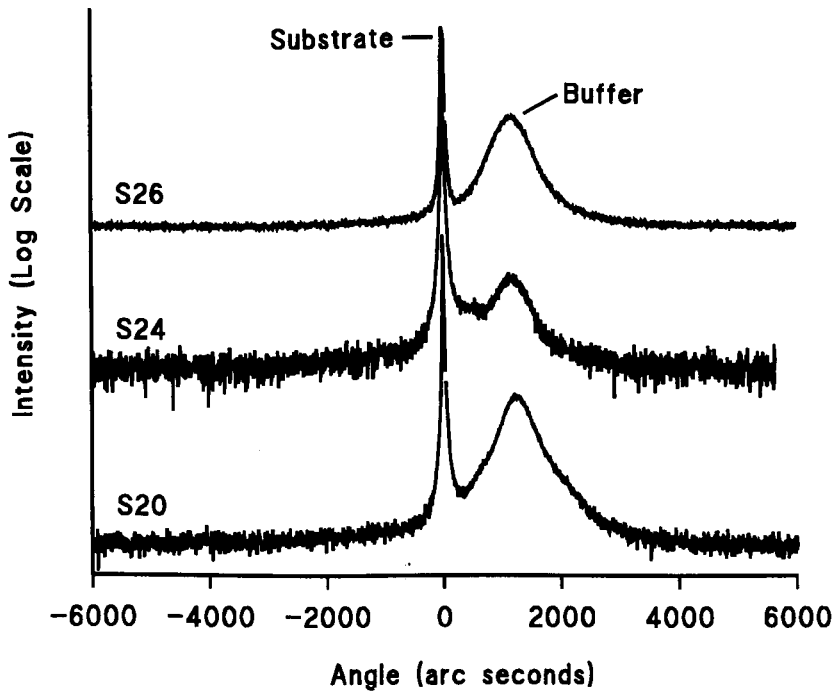

Figure 5.6: Experimental rocking curves of samples S20, S24 and S26 respectively.

5.5.2 Transition Electron Microscope Measurements (TEM)

Transition electron microscope measurements were only carried out on the non-graded SCH sample S20 as shown in figure 5.7. The dark regions in figure 5.7 correspond to the ZnCdS QWs whilst the bright regions correspond to the ZnS barriers. The region marked B is attributed to the 35 Å ZnCdS layer, see figure 5.3. Furthermore, it seems that, during the growth procedure, another QW (the region marked as A) with a higher thickness is deposited unintentionally in sample S20, see figure 5.8. This can only happen during the growth if the Cd shutter is left open (due to mechanical failure) while depositing the ZnS material. In figure 5.8, the thicknesses of the different ZnCdS QWs can be approximated as 60 Å, 35 Å and 5.5 Å which correspond to A, B and C where C defines the quantum wells in the superlattice structure, see figure 5.3 for more details.

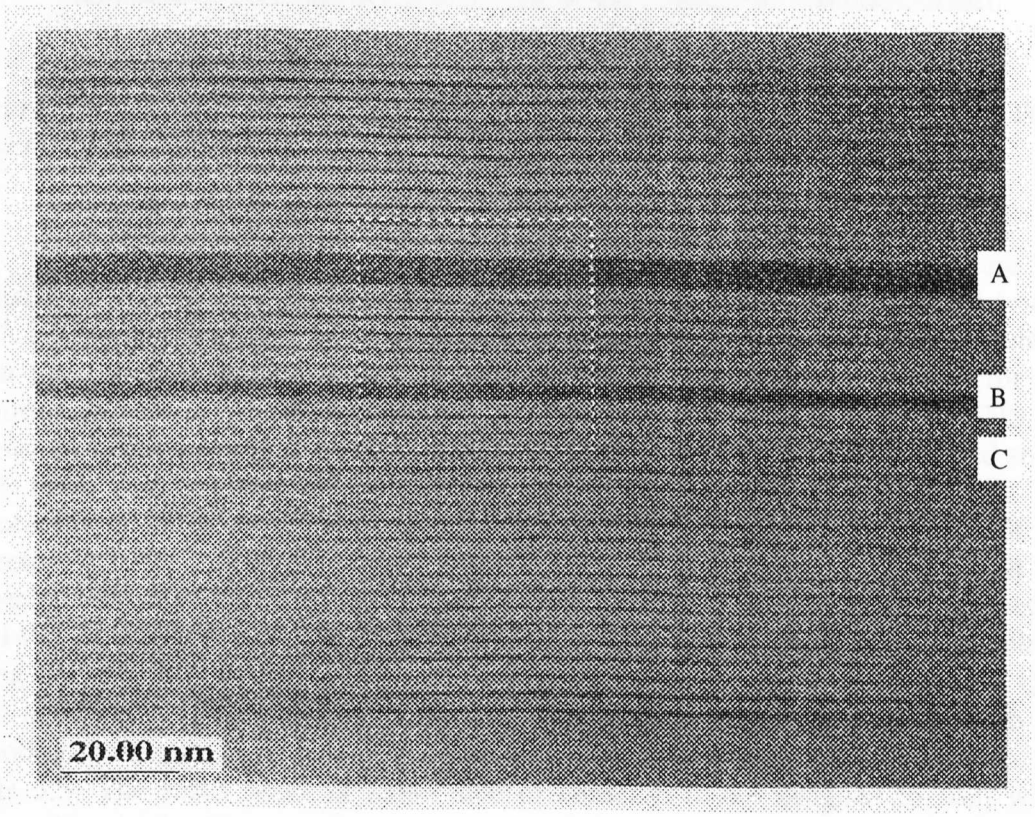

Figure 5.7: Bright field image of the non-graded SCH sample S20. Regions of higher Cd concentration appear dark. The brightness profile of the highlited region is shown in figure 5.8.

5.5.3 PL Measurements

PL measurements were carried out on samples which were mounted strain-free in the cryostat at 4.2 K. The samples were excited by the 300.5 nm line of a large frame Ar^+ laser (Spectra Physics, Model 2045). The photoluminescence spectra were collected in the same way as explained previously in figure 2.8, chapter 2.

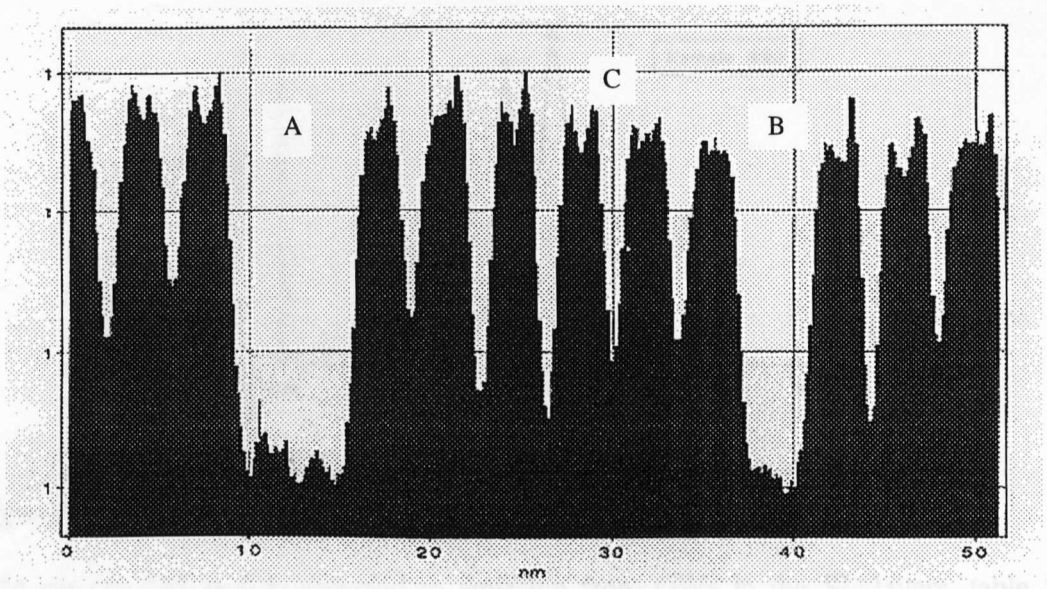

Figure 5.8: Cross sectional brightness profile from figure 5.7, showing the three quantum wells A, B and C.

The PL spectrum of a non-graded SCH structure (S20) is shown in figure 5.9. Emission A seen at an energy of 3.534 eV (or 352 nm) is attributed to emission from a 60 Å ZnCdS quantum well, see figure 5.7. This was identified from its energy calculated with the shooting technique, see chapters 1 and 3. The input parameters for the shooting technique i.e. effective masses and bandgap energies for ZnS and CdS are shown in tables 1.3 and 1.4. The valence band offset for ZnCdS was assumed to be 16% [60]. The calculations for different well widths are shown in table 5.3. The inaccuracy of calculations given in table 5.3 are due to the imprecise values of the effective masses and valence band offset and other parameters. In order to fit the experimental transitions with the calculated ones the Cd concentration was assumed to be 14%. Emission B at 3.588 eV (or 346 nm) is identified, from its energy calculated using the shooting technique (see table 5.3), to emission from the 35 Å ZnCdS QW. The emission at 3.675 eV (or 338 nm), emission C, is identified (again with the shooting technique) as emission from the 5.5 Å ZnCdS QWs in the SL structure, see table 5.3. The small peaks at either side of emission C are assigned to well width fluctuations in the SL structure. In principle, if the quantum well has the same width over the SL structure only one peak would be detected, but due to differences in well widths (narrower or wider quantum wells) due to monolayer fluctuations, different emissions within about 1nm of each other would be observed in the PL spectrum as the calculation in table 5.3 confirms that. Similar structure is seen in figure 5.9.

Figure 5.10 shows the PL spectrum of a GRIN-SCH structure (S24). The main peak observed at energy of 3.634 eV (or 341.5 nm) is again assigned to emission from the 35 Å ZnCdS quantum well layer, see calculation in table 5.4. The small peaks at either side of emission B are again due to small well width fluctuations where narrower and wider wells are formed during the growth, figure 5.10. The small intensity peak at

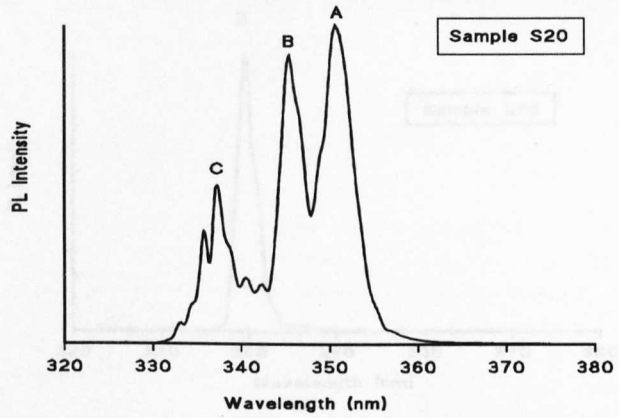

Figure 5.9: The PL spectrum of the non-graded SCH sample S20 at 4.2 K.

3.74 eV (or 332 nm) is assigned to emission from QWs in the SL layers, table 5.4. Similarly, the PL spectrum of the SQW structure (S26) is shown in figure 5.11. The emission observed at 3.65 eV (or 339.5 nm) is attributed also (using shooting technique) to emission from the 35 Å ZnCdS quantum well layer, table 5.4.

Broadening of the PL emissions seen in figures 5.9, 5.10 and 5.11 can be assigned to several effects such as interface fluctuations or compositional fluctuations or lattice mismatch strain in the structures.

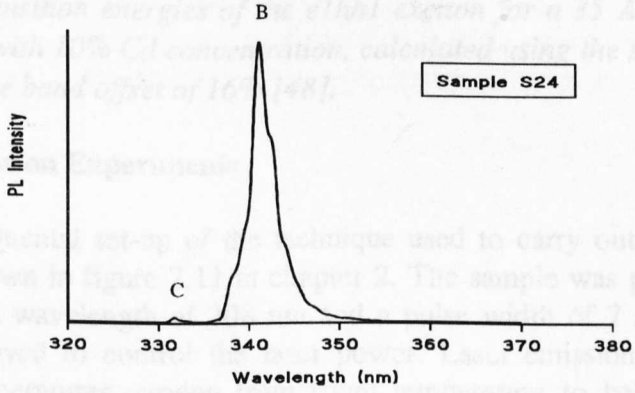

Figure 5.10: The PL spectrum of the graded gap (GRIN-SCH) sample S24 at 4.2 K .

Cd Concentration	14%	14%	14%	14%	14%	14%	14%
Well Width (Å)	60 (A)	40	35 (B)	32.5	30	25	5.5 (C)
Transition Energy (eV)	3.529	3.547	3.554	3.560	3.566	3.582	3.710
Transition Wavelength (nm)	351.2	349.5	348.7	348.1	347.6	346.1	334.1

Table 5.3: Variation of the transition energies of the e1hh1 exciton for a single ZnCdS QW, calculated using the shooting technique, at different will widths assuming a valence band offset of 16% [48]. One monolayer corresponds to 2.5 Å.

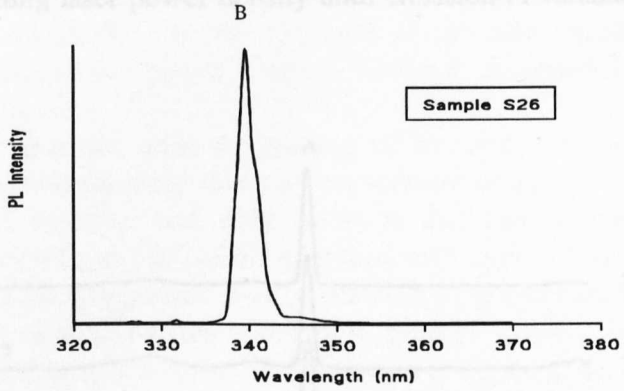

Figure 5.11: The PL spectrum of the SQW sample S26 at 4.2 K.

Cd Concentration	10%	10%
Well Width (Å)	35 (B)	5.5 (C)
Transition Energy (eV)	3.634	3.758
Transition Wavelength (nm)	341.1	329.8

Table 5.4: The transition energies of the e1hh1 exciton for a 35 Å ZnCdS QW and a 5.5 Å ZnCdS QW with 10% Cd concentration, calculated using the shooting technique, assuming a valence band offset of 16% [48].

5.5.4 Laser Emission Experiments

The experimental set-up of the technique used to carry out the laser emission experiments is shown in figure 2.11 in chapter 2. The sample was pumped with a UV pulse beam with a wavelength of 308 nm and a pulse width of 7 ns. Neutral density filters were employed to control the laser power. Laser emission experiments were performed at temperatures varying from room temperature to below 10 K. Optical pumping of the samples were recorded in both front and edge geometries.

5.5.4.1 Laser Emission At Low Temperatures

The various SQW samples were studied and the spectra were recorded at the lowest temperature that can be achieved. Figure 5.12 shows emission from the edge of a non-graded SCH structure (sample S20) showing the onset of lasing at different excitation power at temperature of 8 K. The emission observed at wavelength of 351.5 nm (emission A) is attributed to the laser emission from the 60 Å ZnCdS QW, see figure 5.9. The two broad peaks at wavelengths of 347 nm and 337 nm are assigned to luminescence from the ZnCdS quantum well layers (see emissions B and C in figure 5.9). Figure 5.12 shows also that the laser emission intensity drops sharply when

decreasing the exciting laser power density until emission A vanishes below a value of 8 kW/cm^2.

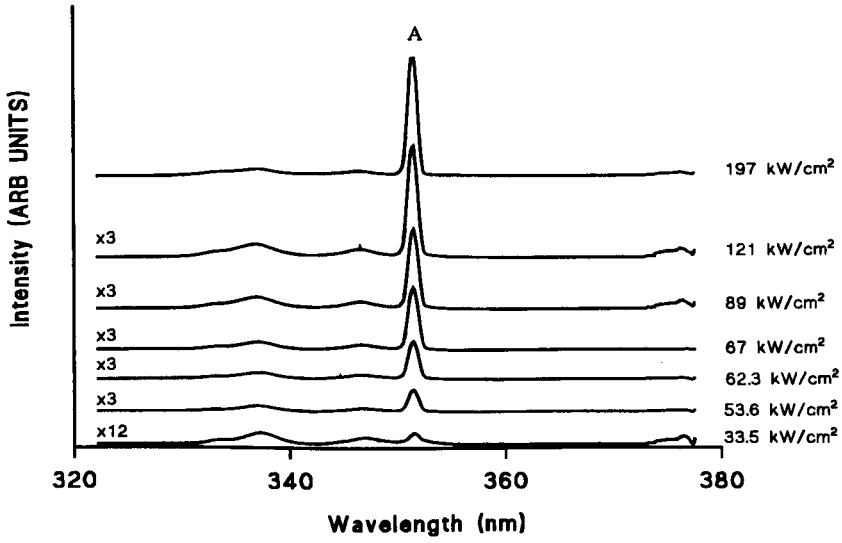

Figure 5.12: Emission from the edge of a non-graded SCH structure (sample S20) showing the onset of lasing at different excitation power at temperature of 8 K.

Similarly the same measurements were carried out on the GRIN-SCH structure (sample S24). Emission from the edge of the GRIN-SCH structure showing the onset of lasing at different excitation power at temperature of 15 K is seen in figure 5.13.

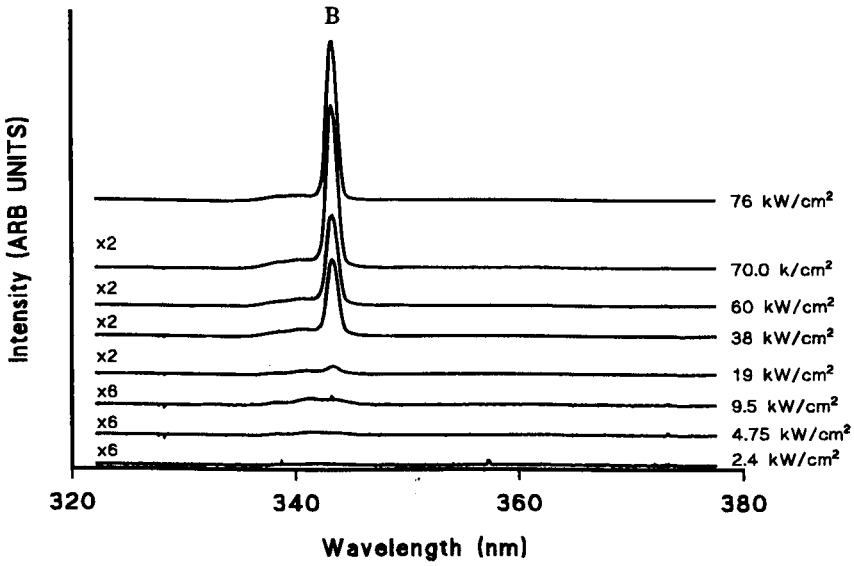

Figure 5.13: Emission from the edge of a GRIN-SCH structure (sample S24) showing the onset of lasing at different excitation power at temperature of 15 K.

The emission at 343.5 nm (emission B) is ascribed as laser emission from the 35 Å ZnCdS QW. Also figure 5.13 shows decrease of the laser emission intensity when decreasing the exciting laser power density. Emission B gradually vanishes below a value of 5 kW/cm^2.

The SQW structure with no grading of barriers (sample S26) was treated likewise. The measurements were taken at temperature of 11 K. No laser emission was observed from this structure and only emission that can be seen in figure 5.14 is luminescence emission from the ZnCdS quantum well layer at 339 nm (see emission B in figure 5.11). A gradual decrease and broadening of the observed emission intensity takes place while decreasing the excitation power density, figure 5.14. Similar measurements were carried out at increasing temperature, on samples S20 and S24. No laser emission was observed from sample S26 at higher temperatures.

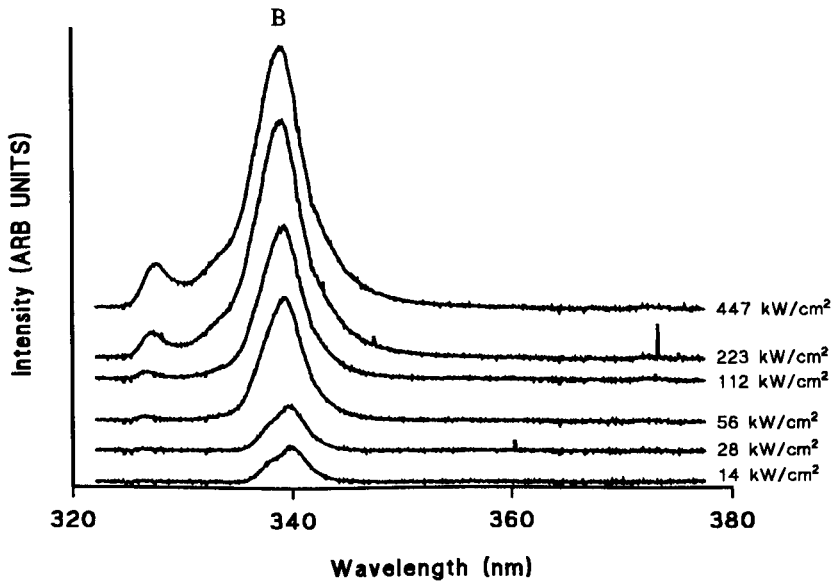

Figure 5.14: Emission from the edge of sample S26 at different excitation power at temperature of 11 K.

5.5.4.2 Laser Emission At High Temperatures

The non-graded SCH was studied at temperatures from 8 K up to 280 K where laser emission from the sample could still be seen. At each temperature, the excitation power density was varied in order to deduce the minimum excitation power density required to obtain laser emission from the sample. For example figure 5.15 shows the onset of lasing at different excitation powers at a temperature of 280 K. It is clear from figure 5.15 that below an excitation power density of 500 kW/cm^2 the laser emission disappears and all that can be observed is luminescence from the quantum well layers.

On the other hand, the GRIN-SCH structure was investigated at temperatures from 14 K up to a maximum temperature of 200 K at which temperature laser emission can still be detected. Also the excitation power density was varied while performing the temperature dependence measurements. Emission from the GRIN-SCH structure shows

the onset of lasing at different excitation powers at a temperature of 200 K can be seen in figure 5.16. Below a value of the excitation power density of 350 kW/cm^2 the laser emission vanishes, figure 5.16.

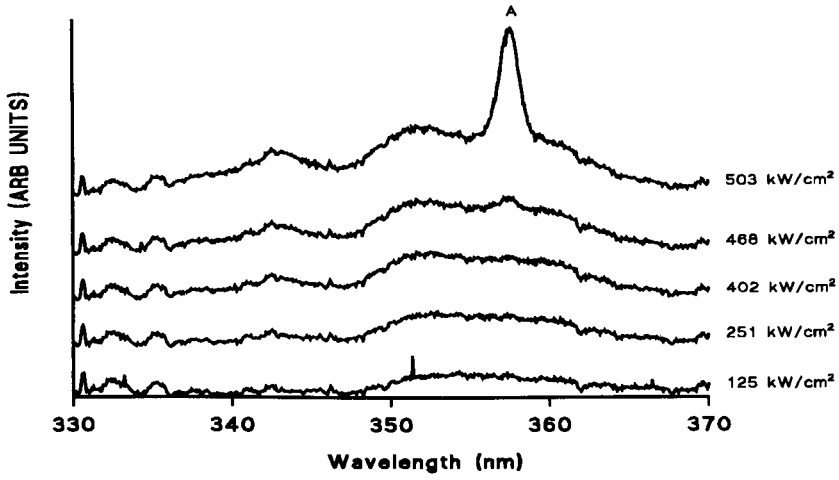

Figure 5.15: Emission from the edge of a non-graded SCH structure (sample S20) showing the onset of lasing at different excitation power at temperature of 280 K.

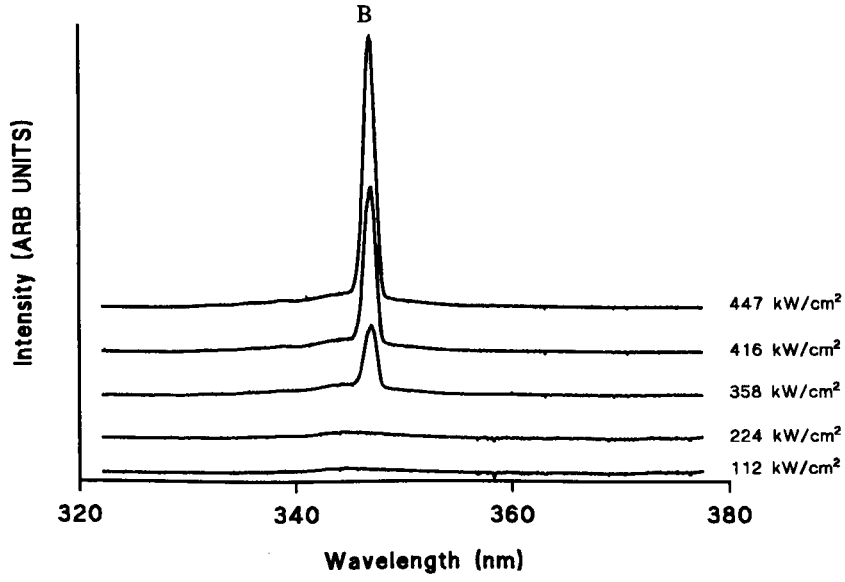

Figure 5.16: Emission from the edge of GRIN-SCH structure (sample S24) showing the onset of lasing at different excitation power at temperature of 200 K.

5.5.5 Lasing Threshold Measurements

The lasing thresholds were found by using double logarithmic plots of the integrated near bandgap emission versus the excitation power density at temperatures

from 8 K up to 240 K, figures 5.12 and 5.13. Figure 5.17 shows the plots for the GRIN-SCH, non-graded SCH and SQW structures at temperature of 10 K. Lasing thresholds, given by the point at which the gradient changed, of 17 kW/cm^2 and 15 kW/cm^2 were obtained for the non-graded SCH and GRIN-SCH structures, respectively whereas no lasing threshold was observed from the SQW structure.

The thresholds for lasing at temperatures from 8 K up to 240 K for the non-graded SCH and GRIN-SCH structures are summarised in table 5.5.

The variation of the lasing thresholds with temperature of the GRIN-SCH and non-graded SCH structures are shown in figure 5.18. The figure indicates that at temperatures from 8 K up to 140 K the lasing thresholds for the non-graded SCH structure are slightly higher than those of the GRIN-SCH structure. Above a temperature of 140 K the lasing thresholds of the GRIN-SCH structure become higher than those found for the non-graded SCH structure, figure 5.18.

Lasing Threshold (kW/cm^2)								
Temperature	8 K	14 K	40 K	80 K	120 K	160 K	200 K	240 K
Non-graded SCH	20	-----	46	44	58	70	130	200
GRIN-SCH	-----	17	21	25	28	-----	220	-----

Table 5.5: Lasing thresholds at temperatures from 8 K up to 240 K for the GRIN-SCH and Non-graded SCH structures.

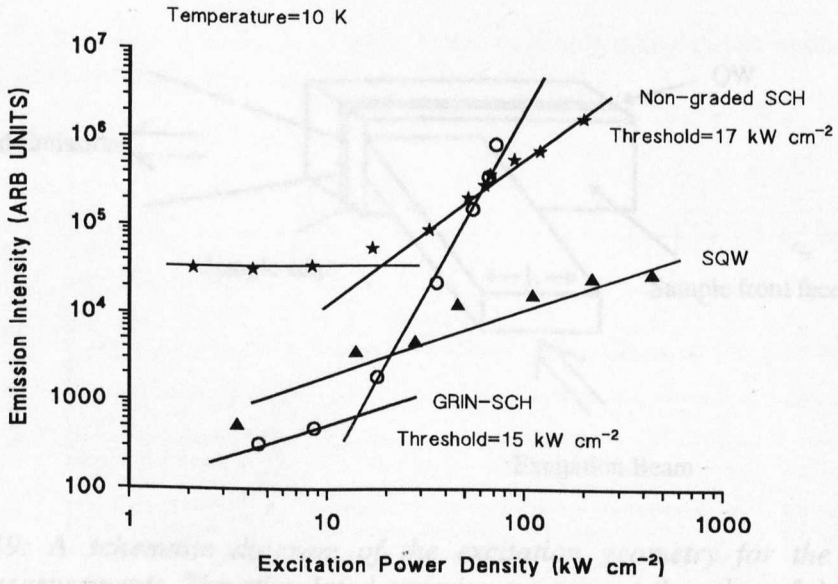

Figure 5.17: Variation of the emission intensity from the edge of the GRIN-SCH (S24), non-graded SCH (S20) and the SQW (S26) structures showing the lasing threshold, of the first two structures, at 10 K.

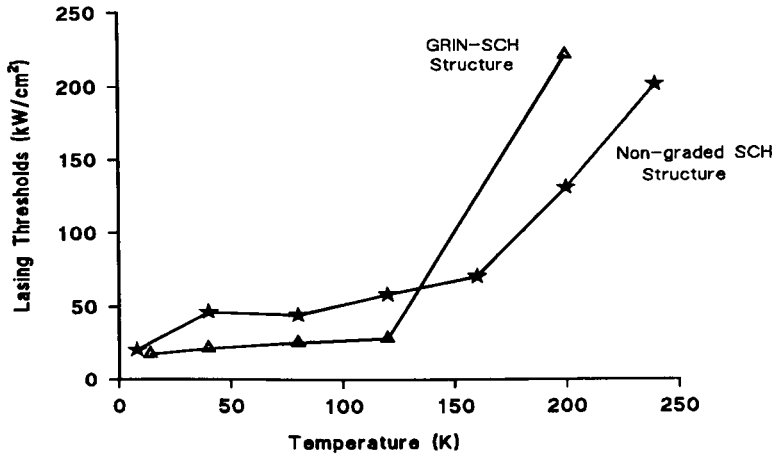

Figure 5.18: Variation of the lasing thresholds with temperature of the GRIN-SCH and non-graded SCH.

5.5.6 Laser Gain Experiments

Measurements of the laser gain from the GRIN-SCH and non-graded SCH structures were made with the variable strip length technique [61]. The nanosecond pulses were focused onto an adjustable slit placed between the spherical lens and the cryostat, see figure 2.11, chapter 2. The image of the slit is focused onto the sample to give a line focus of variable length (L), figure 5.19. The excitation power density and

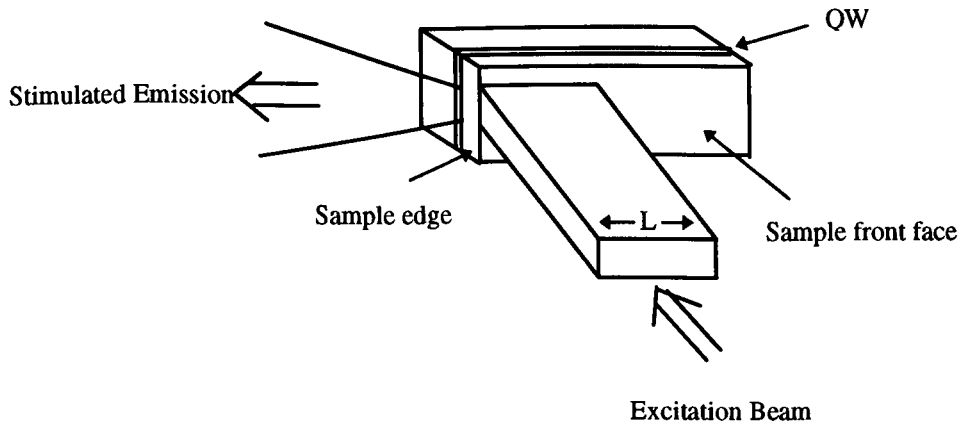

Figure 5.19: A schematic diagram of the excitation geometry for the stimulated emission measurements. The stimulated emission passes out the edge of the sample to the left.

the temperature were kept the same while performing the gain measurements. Only the slit width is changed. Figure 5.20 shows how the laser emission intensity drops when decreasing the slit width for the non-graded SCH structure at a temperature of 10 K.

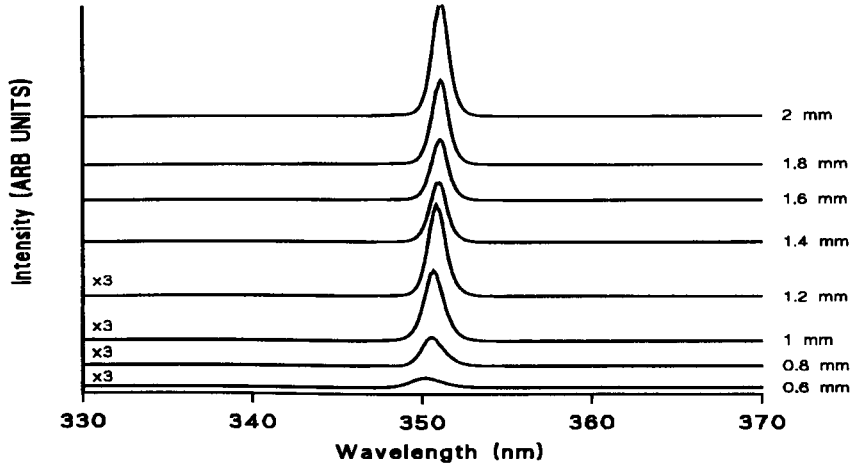

Figure 5.20: Emission from the edge of a non-graded SCH structure showing the onset of lasing at different slit widths at temperature of 10 K.

The laser emission from the edge of the GRIN-SCH structure at different slit widths at temperature of 50 K are shown in figure 5.21. Intensity decrease, broadening and slight blue shifts of the laser emission are observed when decreasing the slit width. The gain was then measured from figures 5.20 and 5.21, see section 5.3. The laser gain was calculated using an equation given by Shaklee et al [61]:

$$I = \frac{c}{g}(e^{gx} - 1) \tag{5.13}$$

where I is the intensity, g is the laser gain, c is a constant and x is the excitation length (equivalent to slit width in this case).

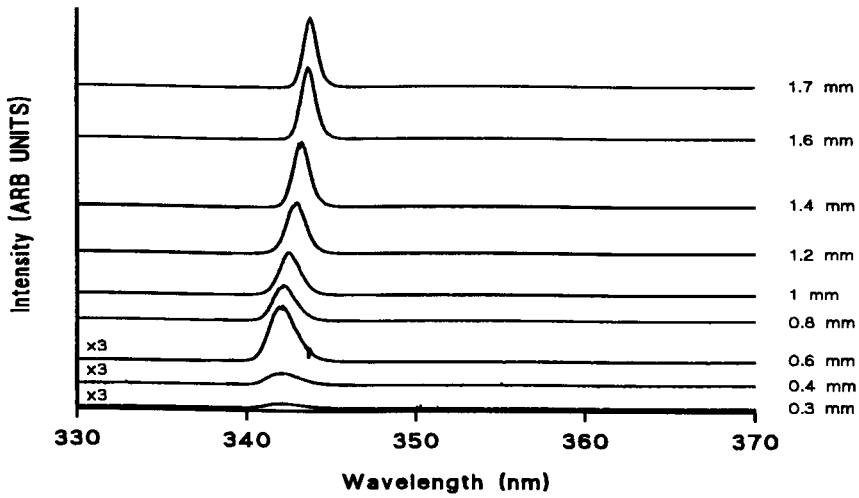

Figure 5.21: Emission from the edge of a GRIN-SCH structure showing the onset of lasing at different slit widths at temperature of 50 K.

Figure 5.22 shows the gain spectrum of the non-graded SCH structure at 10 K. The maximum value of the gain (≈20 cm^{-1}), occurs at a wavelength of 351.5 nm, which correspond to the laser emission from the 60 Å ZnCdS QW. Furthermore, another peak is seen at 348 nm in the gain spectrum.

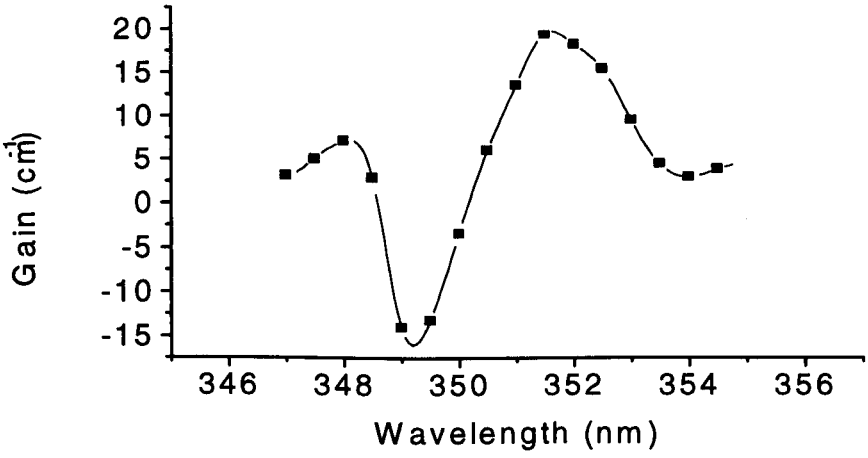

Figure 5.22: Gain spectrum of the non-graded SCH structure at 10 K.

Likewise, the gain spectrum of the GRIN-SCH structure at 50 K is shown in figure 5.23. The maximum value of gain (≈25 cm^{-1}), occurs at a wavelength of 343 nm, at the laser emission from the 35 Å ZnCdS QW. Another peak at 340 nm is seen also in figure 5.23.

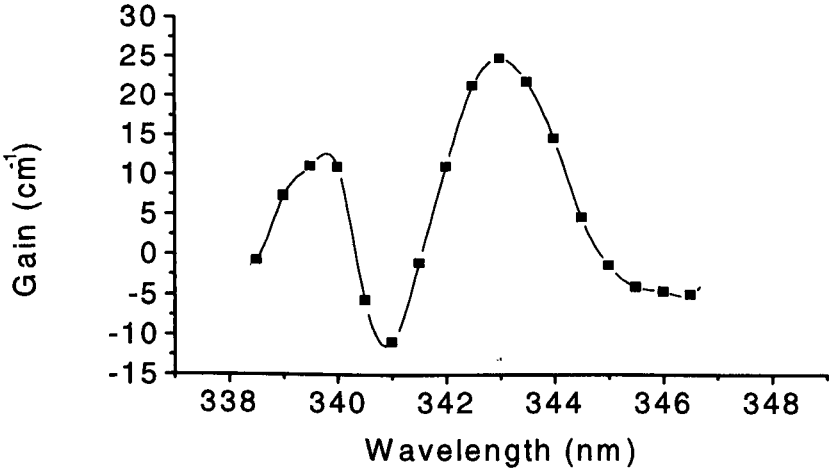

Figure 5.23: Gain spectrum of the GRIN-SCH structure at 50 K.

5.5.7 Electron Beam Pumping Experiments

The GRIN-SCH and non-graded SCH structures were studied using electron beam pumping. The technical set-up of this is very similar to the stimulated emission technique described in figure 2.11, chapter 2, where an electron beam gun is used instead of the laser. The electron beam system was constructed so that optical and electron excitation of the sample could be carried out without changing the configuration of the cryostat by bending the beam with a small laboratory electromagnet. Pulsed e-beam operation was achieved by electrostatic deflection. The maximum current which could be reached is about 10 mA at 10 kV. Astigmatic focusing was used to provide line focusing across the resonator structure. The resulting emissions were collected and analysed at the same way as described in figure 2.11.

Figure 5.24 shows emissions from the edge of the non-grading SCH structure excited with an electron-beam at 10 kV and various currents at different temperatures. No lasing is observed from the sample at any stage when exciting with an e-beam and only broad emissions can be seen. Increasing the temperature leads only to red shifting of the emissions accompanied with intensity decrease. Increasing the current up to the available value of 10 mA did not achieve the desired results of e-beam pumped laser emission.

Similarly, emissions from the edge of the GRIN-SCH structure excited with an electron-beam at 10 kV and various currents and different temperatures are shown in figure 5.25. Also no lasing is detected from the sample and only broad emissions can be seen. Increasing the temperature leads only to decreasing the emission intensities with emission being shifted into smaller energies. Using higher currents up to 10 mA did not yield laser emission from the sample.

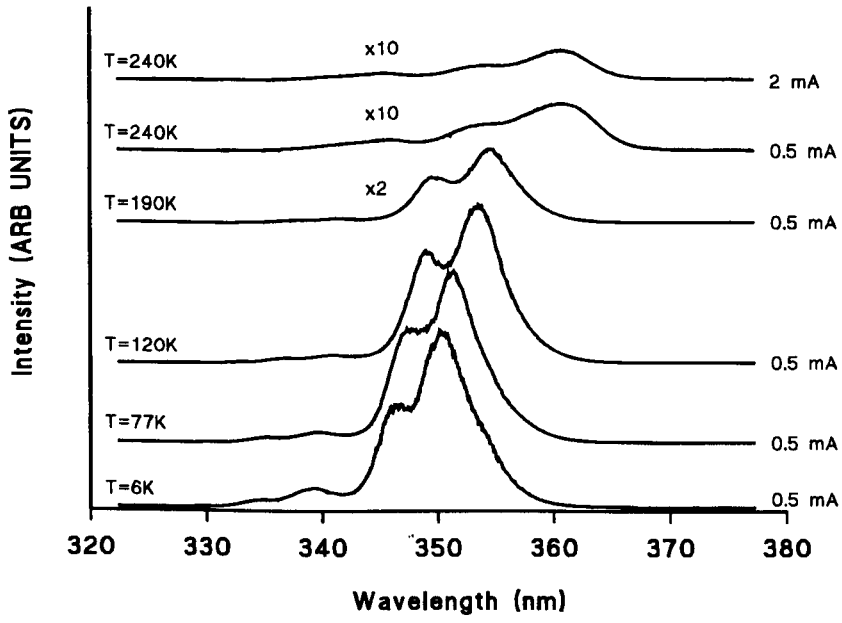

Figure 5.24: Emission from the edge of the non-graded SCH structure pumped with an electron-beam at 10 kV at different currents and different temperatures.

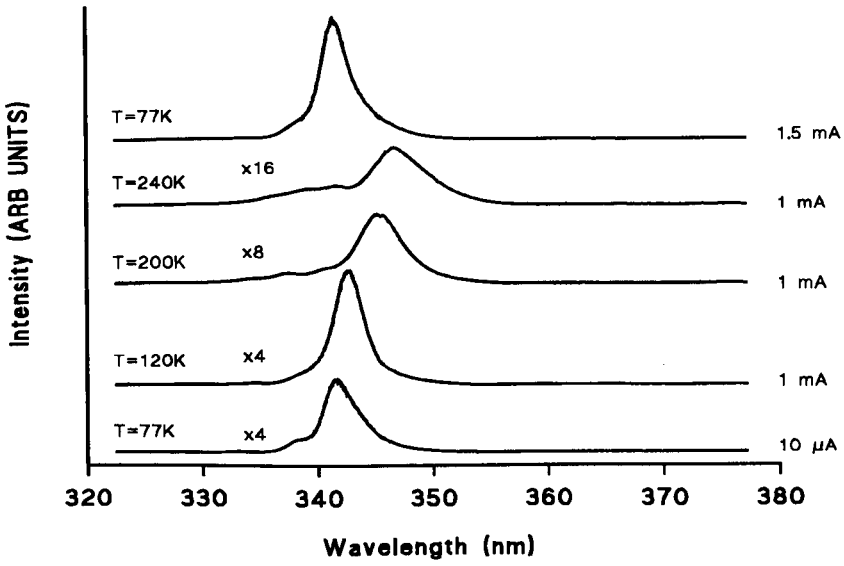

Figure 5.25: Emission from the edge of the GRIN-SCH structure pumped with an electron-beam at 10 kV at different currents and different temperatures.

5.6 Discussion

We report for the first time, to my knowledge, optically pumped laser emission from $ZnS/Zn_{1-x}Cd_xS$ non-graded SCH and GRIN-SCH structures grown on GaP substrate by MBE. Lasing was observed at temperatures up to 280 K from the non-graded SCH structure while lasing from the GRIN-SCH structure was observed at temperatures up to 200 K as shown in figures 5.15 and 5.16 respectively. The non-graded SCH structure produces stimulated emission at a wavelength of 351.5 nm at 8 K whereas the GRIN-SCH structure shows stimulated emission at a wavelength of 343.5 nm at 15 K, figures 5.12 and 5.13. No lasing was observed from the SQW structure, figure 5.14. We attribute this to surface recombination of carriers owing to lack of carrier confinement by a SCH. In the non-graded SCH structure laser thresholds reach a minimum values of 20 kW cm^{-2} at 8 K and 200 kW cm^{-2} at 240 K whereas the minimum threshold values for the GRIN-SCH structure are 17 kW cm^{-2} at 14 K and 220 kW cm^{-2} at 200 K as shown in table 5.5. In fact the optical pumping thresholds at low temperatures, $\approx$ 10 K, are very similar for the GRIN-SCH and non-graded SCH structures, figure 5.17. At higher temperatures up to 140 K the lasing thresholds for the non-graded SCH structure are slightly higher than those of the GRIN-SCH structure. Above a temperature of 140 K the lasing thresholds of the non-graded SCH structure become smaller than those measured for GRIN-SCH structure, where at $\approx$ 200 K the threshold from the former was about half that of the latter structure, figure 5.18. CW PL at 4.2 K with front face excitation from both the GRIN-SCH and non-graded SCH structures show multiple emissions, which can be attributed to emissions from the 60 Å, 35 Å and 5.5 Å quantum wells, see figure 5.9. Optical gain measurements showed

positive gain associated with the SQW. The non-graded SCH structure showed a maximum positive value of gain at ≈20 cm^{-1} at 10 K, this is because the stimulated emission is higher than the absorption, see figure 5.22. This value agrees with the laser emission observed at 351.5 nm from the 60 Å QW. The gain reaches a minimum value of ≈-15 cm^{-1} at a wavelength of 349 nm. This is expected because when approaching the band gap the absorption increases and the stimulated emission decreases resulting in decreasing the gain. The odd thing about the gain spectrum in figure 5.22 is that the gain reaches another peak (≈7.5 cm^{-1}) at a wavelength of 348 nm. This is unusual in gain spectra where only a single maximum peak of gain is reported previously [61]. This observation may be explained if the exciton line is inhomogeneously broadened. Then phase space filling and gain occurs in both the high energy and low energy tail of the emission line. The GRIN-SCH structure revealed a maximum value of gain at ≈25 cm^{-1} at 50 K, figure 5.23. This value virtually corresponds to the laser emission emitted at a wavelength of 343.5 nm from the 35 Å QW. The gain drops off to a minimum value of ≈-12 cm^{-1} at a wavelength of 341 nm. This also can be understood in terms of the absorption being higher than the stimulated emission when approaching the bandedge. Similarly, the gain has another peak (≈12 cm^{-1}) at a wavelength of ≈ 340 nm. This also may be explained for the same reason mentioned above.

No laser emission has been observed with electron beam pumping. This is partly because poor focusing of the electron gun meant that higher currents than were desirable had to be used, resulting in sample heating. At 100 K the threshold for laser action is typically 100 kW cm^{-2} from the optical pumping data. The maximum power of the electron gun is 100 W (10 mA, 10 kV), requiring a line focus of ≈ 30 μm (assuming only 30% of the e-beam energy produces electron-hole pairs). We were unable to achieve this degree of focusing, without which lasing would seem not to be possible in the structures grown.

5.7 Conclusion

In conclusion, we have demonstrated optically pumped UV laser emission in $ZnS/Zn_{1-x}Cd_xS$ non-graded SCHs and GRIN-SCHs and measured the optical gain. We have shown the need to prevent surface recombination if laser action is to be achieved and find that a GRIN-SCH or a non-graded SCH structures are equally effective in achieving this. The minimum laser threshold of the non-graded SCH structure is 20 kW cm^{-2} at 8 K and the maximum gain obtained is approximately 20 cm^{-1} at 10 K. The minimum threshold value for the GRIN-SCH structure is 17 kW cm^{-2} at 14 K and the maximum gain attained is ≈25 cm^{-1} at 50 K. Electron-beam pumped lasing of the SCH structures is not achieved because we were unable to focus the electron beam sufficiently to reach the threshold power densities measured by optical pumping.

References

[1] Compound Semiconductors 2, 7 (1996).

[2] H. Okuyama, Y. Kishita, T. Miyajima, A. Ishibashi, and K. Akimoto, Appl. Phys. Lett 64, 904 (1994).

[3] I. Akasaki, H. Amano, S. Sota, H. Sakai, T. Tanaka, and M. Koike, Jpn. J. Appl. Phys. 34, L1517 (1995).

[4] T. J. Schmidt, X. H. Yang, W. Shan, J. J. Song, A. Salvador, W. Kim, O. Aktas, A. Botchkarev, H. Morkoc, Appl. Phys. Lett. Vol. 68, No. 13, pp. 1820-1822 (1996).

[5] J. M. Redwing, D. A. S. Loeber, N. G. Anderson, M. A. Tischler, and J. S. Flynn, Appl. Phys. Lett. Vol. 69, No. 1, pp. 1-3 (1996).

[6] M. V. Maksimov, A. V. Sakharov, V. V. Lundin, A. S. Usikov, B. V. Pushnyi, I. L. Krestnikov, N. N. Ledentsov, P. S. Kopev, Z. I. Alferov, and V. P. Rozum, Technical. Phys. Lett. Vol. 23, No. 8, pp. 597-599 (1997).

[7] K. Domen, A. Kuramata, R. Soejima, K. Horino, S. Kubota, and T. Tanahashi, IEEE Journal of Selected Topics In Quantum Electronics. Vol. 4, No. 3, pp. 490-497 (1998).

[8] P. Schlotter, J. Baur, C. Hielscher, M. Kunzer, H. Obloh, R. Schmidt, and J. Schneider, Materials Science and Engineering B-Solid State Materials for Advanced Technology. Vol. 59, No. 1-3, pp. 390-394 (1999).

[9] J. Wu, H. Yaguchi, K. Onabe, and Y. Shiraki, J. Cryst. Growth. Vol. 197, No. 1-2, pp. 73-77 (1999).

[10] I. L. Krestnikov, W. V. Lundin, A. V. Sakharov, V. A. Semenov, A. S. Usikov, A. F. Tsatsulnikov, Z. I. Alferov, N. N. Ledentsov, A. Hoffmann, and D. Bimberg Appl. Phys. Lett. Vol. 75, No. 9, pp. 1192-1194 (1999).

[11] V. I. Kozlovsky, A. B. Krysa, Y. K. Skyasyrsky, Y. M. Popov, A. Abare, M. P. Mack, S. Keller, U. K. Mishra, L. Coldren, S. DenBaars, M. D. Tiberi, and T. George, Mrs Internet Journal of Nitride Semiconductor Research. Vol. 2, No. 33-

41, pp. 35-39 (1997).

[12] T. J. Schmidt, S. Bidnyk, Y. H. Cho, A. J. Fischer, J. J. Song, S. Keller, U. K. Mishra, and S. P. DenBaars, Appl. Phys. Lett. Vol. 73, No. 25, pp. 3689-3691 (1998).

[13] S. Nakamura, M. Senoh, S. Nagahama, N. Iwasa, T. Matushita, and T. Mukai, Mrs Internet Journal of Nitride Semiconductor Research. Vol. 4, No. S1, pp. U6-U22 (1999).

[14] I. Akasaki, H. Amano, S. Sota, H. Sakai, T. Tanaka, and M. Koike, Japan. J. Appl. Phys. Part 2-Lett. Vol. 34, No. 11B, pp. 1517-1519 (1995).

[15] D. Hofstetter, R. L. Thornton, L. T. Romano, D. P. Bour, M. Kneissl, and R. M. Donaldson, Appl. Phys. Lett. Vol. 73, No. 15, pp. 2158-2160 (1998).

[16] K. B. Ozanyan, J. E. Nicholls, M. O'Neill, L. May, J. H. C. Hogg, W. E. Hagston, B. Lunn, and D. E. Ashenford, Appl. Phys. Lett. 27, 4230-4232 (1996).

[17] K. B. Ozanyan, L. May, J. E. Nicholls, J. H. C. Hogg, W. E. Hagston, B. Lunn, and D. E. Ashenford, Solid. State. Communications. 97, (5) pp. 345-348 (1996).

[18] R. L. Gunshor, J. Han, G. C. Hua, A. V. Nurmikko, and H. Jeon, J. Crys. Growth 159, 1 (1996).

[19] S. Guha, H. Cheng, M. A. Haase, J. M. DePuydt, J. Qiu, B. J. Wu, and G. E. Hofler, Appl. Phys. Lett. 65 (7), 801 (1994).

[20] S. Guha, J. M. DePuydt, M. A. Haase, J. Qiu, and H. Cheng, Appl. Phys. Lett. 63 (23), 3107 (1993).

[21] D. Herve, J. M. Bonard, L. Vanzetti, J. J. Paggel, L. Sorba, J. D. Ganiere, E. Molva, and A. Franciosi, J. Crys. Growth 159, 600 (1996).

[22] E. Molva, R. Accomo, G. Labrunie, J. Cibert, C. Bodin, L. S. Dang, and G. Feuillet, Appl. Phys. Lett. 62, 796 (1993).

[23] D. Herve, R. Accomo, E. Molva, L. Vanzetti, J. J. Paggel, L. Sorba, and A. Franciosi, Appl. Phys. Lett. 67, 2144 (1995).

[24] *Proceedings of the 12th IEEE international semiconductor laser conference.* Davos, Switzerland, September (1990).

[25] H. Kroemer, A proposed class of heterojunction lasers, Proc. IEEE 51, 1782-1783 (1963).

[26] Zh. I. Alferov, R. F. Kazarinov. Semiconductor laser with electrical pumping,

U.S.S.R. Patent 181737 (1963).

[27] J. M. Woodall, H. Rupprecht, and G. D. Pettit. Solid state device conference (1967), Santa Barbara, California. [Abstract reported in IEEE Trans. Electron. Devices ED-14, 630 (1967).].

[28] H. C. Casey, and M. B. Panish. Heterostructure lasers, Chapter 1. Academic Press, New York (1968).

[29] Zh. I. Alferov, V. M. Andreev, D. Z. Garbuzov, Yu. V. Zhilyaev, E. P. Morozov, E. L. Portnoi, and V. G. Trofim. Sov. Phys. Semicon. 4, 1573 (1971).

[30] I. Hayashi, M. B. Panish, P. W. Foy, and S. Sumski. Junction lasers which operate continuously at room temperature, Appl. Phys. Lett. 17, 109 (1970).

[31] J. P. Van Der Ziel, R. Dingle, R. C. Miller, W. Wiegmann, and W. A. Nordland. Jr. laser oscillations from quantum states in very thin GaAs/$Al_{0.2}Ga_{0.8}As$ multilayer structures, Appl. Phys. Lett. 26, 463-465 (1975).

[32] R. C. Miller, R. Dingle, A. C. Gossard, R. A. Logan, and W. A. Nordland. Jr. laser oscillations with optically pumped very thin GaAs/$Al_xGa_{1-x}As$ multilayer structures and conventional double heterostructures, J. Appl. Phys. 47, 4509-4517 (1976).

[33] R. D. Dupuis, and P. D. Dapkus. Very low threshold GaAs/$Al_xGa_{1-x}As$ double heterostructure lasers grown by MOCVD, Appl. Phys. Lett. 32, 473-475 (1978).

[34] R. D. Dupuis, and P. D. Dapkus, N. Holonyak, Jr, E. A. Rezek, and R. Chin. Room temperature operation of quantum well GaAs/$Al_xGa_{1-x}As$ laser diodes grown by MOCVD, Appl. Phys. Lett. 32, 295-297 (1978).

[35] A. Y. Cho, R. W. Dixon, H. C. Casey, Jr, and R. L. Hartman. Continuous room temperature operation of GaAs/$Al_xGa_{1-x}As$ double heterostructure lasers prepared by MBE, Appl. Phys. Lett. 28, 501-503 (1976).

[36] W. T. Tsang, C. Weibuch, R. C. Miller, and R. Dingle. Current injection GaAs/$Al_xGa_{1-x}As$ multi-quantum-well heterostructure lasers prepared by MBE, Appl. Phys. Lett. 35, 673-675 (1979).

[37] W. T. Tsang, Extremely low threshold (AlGa)As modified multiquantum well heterostructure lasers grown by MBE, Appl. Phys. Lett. 39, 786-788 (1981).

[38] W. T. Tsang, Extremely low threshold (AlGa)As graded-index waveguide separate-confinement heterostructure lasers grown by MBE, Appl. Phys. Lett. 40, 217-219 (1982).

[39] M. A. Haase, J. Qiu, J. M. DePuydt, and H. Cheng, Appl. Phys. Lett, 59, 1272

(1991).

[40] H. Jeon, J. Ding, W. Patterson, A. V. Nurmikko, W. Xie, D. C. Grillo, M. Kobayashi, and R. L. Gunshor, Appl. Phys. Lett, 59, 3619 (1991).

[41] W. Xie, D. C. Grillo, R. L. Gunshor, M. Kobayashi, G. C. Hua, N. Otsuka, H. Jeon, J. Ding, and A. V. Nurmikko, Appl. Phys. Lett, 60, 463 (1992).

[42] H. Jeon, J. Ding, A. V. Nurmikko, W. Xie, M. Kobayashi, and R. L. Gunshor, Appl. Phys. Lett, 60, 892 (1992).

[43] R. N. Bylsma, W. M. Becker, T. C. Bonsett, L. A. Kolodziejski, R. L. Gunshor, M. Yamanishi, and S. Datta, Appl. Phys. Lett, 47, 1039 (1985).

[44] Y. Kawakami, S. Yamaguchi, Y. -H. Wu, K. Ichino, Sz. Fujita, and Sg. Fujita, Jpn. J. Appl. Phys. 30, L605 (1991).

[45] K. Ichino, Y. -H. Wu, Y. Kawakami, Sz. Fujita, and Sg. Fujita, J. Crys. Growth. 117, 527 (1992).

[46] K. Nakanishi, I. Suemune, Y. Fujii, Y. Kuroda, and M. Yamanishi, Appl. Phys. Lett, 59, 1401 (1991).

[47] G. Sun, K. Shahzad, J. M. Gaines, and J. B. Khurgin, Appl. Phys. Lett, 59, 310 (1991).

[48] D. Lee, A. M. Johnson, J. E. Zucker, C. A. Burrus, R. D. Feldman, and R. F. Austin, Appl. Phys. Lett, 60, 739 (1992).

[49] T. Taguchi, Y. Endoh, and Y. Nozue, Appl. Phys. Lett. 56, 342 (1991).

[50] Y. Endoh, and T. Taguchi, Mter. Res. Soc. Symp. Proc. 161, 211 (1990).

[51] Y. Yamada, J. Mullins, Y. Masumoto, and T. Taguchi, Conf. Dig. 13th Int. Semicond. lasers. Conf. Takamatsu. p162 (1992).

[52] T. Taguchi, Y. Masumoto, J. Mullins, and T. Taguchi, Appl. Phys. Lett. 61, 2190 (1992).

[53] J. Ding, H. Joen, T. Ishihara, A. V. Nurmikko, H. Luo, N. Samarth, and J. Furdana, Surf. Sci. 287, 616 (1992).

[54] T. Taguchi, C. Onodera, Y. Yamada, and Y. Masumoto, Jpn. J. Appl. Phys. 32, L1308 (1993).

[55] Y. Yamada. Y. Masumoto, T. Taguchi, J. Crys. Growth. 138, 570-574 (1994).

[56] Y. Kawakami, B. C. Cavenett, K. Ichino, Sz. Fujita, and Sg. Fujita, Jpn. J. Appl. Phys. 32, L730 (1993).

[57] "*Semiconductor lasers: Past, Present and Future*", Govind. P. Agrawal, Chapter 1, pp. 1-27 (AIP Press, 1995)

[58] L. May, PhD Thesis. University of Hull (1999).

[59] S. R. Chinn, P. S. Zory, and A. R. Reisinger, IEEE, J. Quantum. Electron. 24 (11), pp2191-2214 (1988).

[60] T. Yokogawa, T. Ishikawa, J. L. Merz, and T. Taguchi, J. Appl. Phys. 75 (4) pp. 2189-2193 (1994)

[61] K. L. Shaklee, R. E. Nahory, and R. F. Leheny, J. Luminescence. 7, pp. 284-309 (1973).